Experimental and Modelling Study of Catalytic Diesel Soot Oxidation

Kirsten Leistner

THÈSE DE DOCTORAT DE
L'UNIVERSITÉ PIERRE ET MARIE CURIE

Spécialité: Génie des procédés et des technologies avancées

Présentée par

Kirsten LEISTNER

Pour obtenir le grade de
DOCTEUR de l'UNIVERSITÉ PIERRE ET MARIE CURIE

Etude expérimentale et modélisation de l'oxydation catalysée de suies Diesel

soutenue le 4 mai 2012

devant le jury composé de:

Mme V. TSCHAMBER	Professeur à l'Université de Haute-Alsace	Rapporteur
M. Ph. VERNOUX	Directeur de recherche à l'IRCELYON	Rapporteur
M. P. DA COSTA	Professeur à l'Université Pierre et Marie Curie	Directeur de thèse
M. S. CAVADIAS	Professeur à l'Université Pierre et Marie Curie	Examinateur
M. O. DEUTSCHMANN	Professeur au Karlsruher Institut für Technologie	Examinateur
M. A. NICOLLE	Ingénieur IFP Energies nouvelles	Examinateur Co-encadrant
M. H. COLAS	Ingénieur PSA	Invité

Abstract

This study describes the development of kinetic models for platinum-ceria-zirconia ($Pt/Ce_xZr_{1-x}O_2$)-catalysed diesel particle filter (DPF) regeneration. Such models have a practical purpose in that they can be used to calculate source terms in 3D flow models, and they also have an intrinsic interest for the understanding of the mechanisms of catalysed soot oxidation. The core of this kinetic analysis consists in estimating Arrhenius parameters of a number of (semi) detailed reaction steps by fitting calculated curves to experimental ones. In doing so, understanding of the roles of the different reactants has been gained, and the efficacy and limitations of the modelling procedure for gas-solid heterogeneous reactions investigated. Amongst the examined aspects is the feasibility of attributing physically meaningful values to individual parameters in large reaction mechanisms. This is achieved by fitting one "subset"of reaction steps at a time. The procedure is illustrated by means of the cases of soot oxidation by NO, NO_2 and/or O_2, NO oxidation catalysed by ceria-based catalysts and soot oxidation catalysed by $Pt/Ce_xZr_{1-x}O_2$. Experiments used for these kinetic studies are temperature programmed tests in a fixed bed reactor. In order to extract kinetic parameters, a reactor model describing gas flow through a bed of particles and a meanfield model of soot and catalyst surface chemistry have been developed. The interest of these detailed kinetic mechanisms lies in their ability to describe all the reaction products instead of concentrating merely on global soot consumption rate. The role of a heterogeneous reactive surface, such as that of soot structure and ceria-zirconia composition/structure have been considered, as well as the soot/catalyst ratio.

Keywords: meanfield model, kinetics, soot, catalytic oxidation, diesel particulate filter, nitrogen oxides, ceria zirconia

---

Resumé

L'objectif de cette ètude est de développer des modèles cinétiques pour la régénération des filtres à particules Diesel (FaP), basés sur la catalyse par des formulations du type platine-cérine-zircone ($Pt/Ce_xZr_{1-x}O_2$). L'intérêt pratique de ce type de modèle est lié à son utilité dans le calcul de termes sources chimiques dans des modèles 3D, et la possibilité d'étudier le mécanisme réactionnel de l'oxydation catalysée de la suie. Au coeur de cette analyse cinétique se situe l'estimation des paramètres d'Arrhenius pour un ensemble d'étapes réactionnelles, en ajustant les courbes théoriques (calculées) à celles obtenues expérimentalement. Ce faisant, l'objectif n'est pas seulement de comprendre le rôle des différents réactifs, mais aussi d'explorer l'efficacité et les limitations de la modélisation des réactions hétérogènes à l'interface des phases gazeuses et solides. Le défi principal de cette démarche est l'attribution de valeurs physiques pertinents à des paramètres individuels dans un mécanisme réactionnel complexe. Notre stratégie pour aborder ce problème consiste en un ajustement progressif de sous-ensembles des étapes réactionnelles. Pour illustrer cette procédure, nous avons développé trois configurations d'oxydation des suies : i) l'oxydation par O_2, NO et/ou NO_2, non catalysée ii) l'oxydation par NO_2 en présence d'un catalyseur en cérine, et iii) l'oxydation catalysée par $Pt/Ce_xZr_{1-x}O_2$. Les études cinétiques expérimentales ont été menées sous forme de tests en température programmée, dans un réacteur à lit fixe. Afin de déduire les paramètres cinétiques à partir de ces données, un modèle de réacteur décrivant l'écoulement de gaz à travers un empilement de particules a été construit. Ce modèle comprend un sous-modèle portant sur la surface chimique des suies et du catalyseur, basé sur l'approximation du champ moyen. L'impact de la structure graphitique des suies, la composition/structure de la cérine-zircone et du ratio suie/catalyseur dans la réaction ont été considérés.

Mots-clefs: *approximation du champ moyen, cinétique, suies, oxydation catalysée, filtre à particules Diesel, oxydes d'azote, cérine zircone*

Acknowledgements

First of all, I would like to acknowledge ANRT and IFP Énergies nouvelles (IFPEn) for financial support of this reasearch in form of a CIFRE bursary. I should also like to thank Institut Jean LeRond D'Alembert, Université Pierre et Marie Curie (IJLRA, UPMC) for hosting me for several months of experimental work.

Many people in various capacities have contributed to this study. First among them are my two advisors, Patrick Da Costa from IJLRA and André Nicolle from IFPEn. I would like to thank Patrick for his kind, openminded approach and never splitting hairs. André I thank for mentoring me on a day to day basis and steering my dissertation topic towards chemical engineering and chemistry. Several engineers from IFPEn should be acknowledged for their technical help, especially David Berthout for his help with AmeSim and Anthony Velghe and Rajesh Kumar for their help with IFP-C3D. I am thankful for all the help with chemical concepts, modelling and coping with administrative procedures offered by Nikola and Stavros and their friendly encouragement. I also thank Kader, Rui and Gosia for their technical help with experiments, and I appreciated the company of many other Ph.D. students at IFPEn and IJLRA. Many thanks to my family who encouraged me from afar and to Teddy for all his helpful advice and support.

Last but not least, I am convinced that my past three years in France would never have yielded what they did *sans* a number of particular contributions. It would certainly not have been the same without the purposeful, decisive planning and clear objectives of my advisors, the unquestioning support and tolerant atmosphere of IFPEn and the excellent, responsive administrative services of IFPEn and UPMC.

Remerciements

Tout d'abord, je tiens à remercier l'ANRT et l'IFP Énergies nouvelles (IFPEn) d'avoir financé ce projet de thèse sous forme d'une bourse CIFRE. Je remercie également l'Institut Jean Le Rond D'Alembert, Université Pierre et Marie Curie (IJLRA, UPMC) de m'avoir accueilli durant plusieurs mois pour effectuer mon travail expérimental.

Beaucoup de gens ont contribué à ce projet de thèse, à des titres très variées. Les premiers à citer parmi eux sont mes deux encadrants : Patrick Da Costa (IJLRA) et André Nicolle (IFPEn). Je tiens à remercier Patrick de m'avoir fait témoigner de sa gentillesse et de son esprit ouvert, et de n'avoir pas cherché à couper les cheveux en quatre. Je suis très reconnaissante à André de m'avoir encadré quotidiennement et d'avoir piloté ce projet vers l'ingénierie chimique et la chimie en générale. Plusieurs ingénieurs de l'IFPEn m'ont apporté une assistance technique précieuse : David Berthout (avec AmeSim) et Anthony Velghe et Rajesh Kumar (avec IFP-C3D). Je suis très reconnaissante à Nikola et Stavros pour leur aide et conseils concernant les concepts chimiques, modélisation, et la gestion des affaires administratives, mais surtout pour leur amitié. Je remercie également Kader, Rui et Gosia pour l'assistance technique. J'ai eu la chance de côtoyer des nombreux thésards à l'IFPEn et l'IJLRA et ce fut une expérience fort agréable. Grand merci à ma famille qui m'a encouragé de loin et à Teddy pour ses conseils et soutien.

Pour en conclure, je suis convaincue que mon rendement scientifique durant les trois années passées en France n'aurait pas été le même sans un nombre de contributions clés. Parmi ces contributions je compte la planification résolue avec des objectifs clairs de la part de mes encadrants, le soutien non-conditionnel et l'atmosphère de tolérance dont j'ai pleinement profité à l'IFPEn et surtout le service éclaire (et adaptable sur mesure) de la part des services de soutien administratif de l'IFPEn et l'UPMC.

Contents

Introduction

L'objectif de cette thèse est de développer des modèles cinétiques pour la régénération des filtres à particules Diesel (FaP), basés sur la catalyse par des formulations du type platine-cérine-zircone ($Pt/Ce_xZr_{1-x}O_2$). L'intérêt pratique de ce type de modèle est lié à son utilité dans le calcul de termes sources chimiques dans des modèles 3D, et la possibilité d'étudier le mécanisme réactionnel de l'oxydation catalysée de la suie. Au coeur de cette analyse cinétique se situe l'estimation des paramètres d'Arrhenius pour un ensemble d'étapes réactionnelles, en ajustant les courbes théoriques (calculées) à celles obtenues expérimentalement. Ce faisant, l'objectif n'est pas seulement de comprendre le rôle des différents réactifs, mais aussi d'explorer l'efficacité et les limitations de la modélisation des réactions hétérogènes à l'interface des phases gazeuses et solides. Le défi principal de cette démarche est l'attribution de valeurs physiques pertinents à des paramètres individuels dans un mécanisme réactionnel complexe. Notre stratégie pour aborder ce problème consiste en un ajustement progressif de sous-ensembles des étapes réactionnelles.

Pour illustrer cette procédure, nous avons développé trois configurations d'oxydation des suies : i) l'oxydation par O_2, NO et/ou NO_2, non catalysée ii) l'oxydation par NO_2 en présence d'un catalyseur en cérine, et iii) l'oxydation catalysée par $Pt/Ce_xZr_{1-x}O_2$. La cinétique de ces réactions n'a pas été exhaustivement étudiée auparavant, et nos résultats ont apporté une meilleure compréhension de ce phénomène. L'approche d'ajustement s'est démontré justifiée, car elle a permis la reproduction de profils d'espèces-clés dans un ensemble de conditions expérimentales. Les études cinétiques expérimentales ont été menées sous forme de tests en température programmée, dans un réacteur à lit fixe. Une partie de nos données expérimentales a été obtenue directement ainsi, les autres donnée provenant d'études publiées par d'autres groupes. Afin de déduire les paramètres cinétiques à partir de ces données, un modèle de réacteur décrivant l'écoulement de gaz à travers un empilement de particules a été construit. Ce modèle comprend un sous-modèle portant sur la surface chimique des suies et du catalyseur, basé sur l'approximation du champ moyen. L'impact de la structure graphitique des suies, la composition/structure de la cérine-zircone et du ratio suie/catalyseur dans la réaction ont été considérés. Les paramètres décrivant leurs effets ont été estimés.

Dans le chapitre 1 de ce manuscrit, le contexte et l'état d'art concernant la recherche sur les FaP sont présentés. Nous nous intéressons par la suite aux diverses motivations sous-tendant ces travaux, liées à la santé humaine, l'environnement et la législation. Finalement, les modèles de FaP existants ainsi que leurs particularités sont discutés. Le chapitre 2 présente la démarche expérimentale, le matériel et méthodes, et le chapitre 3 porte sur notre approche de modélisation. Les Chapitres suivants (4-6) traitent des systèmes réactionnels particuliers, et l'étude de leur cinétique par des approches expérimentales et de la modélisation. Dans les Chapitres 4 et 5 certains aspects de la chimie du FaP sont traités, notamment l'oxydation des suies en absence de catalyseur, et l'interaction du catalyseur avec les gaz d'échappement. Enfin, le chapitre 6 porte sur la cinétique de la régénération dans l'ensemble d'un FaP catalysé par $Pt/Ce_xZr_{1-x}O_2$.

Scope and Outline

The objective of this Ph.D. thesis is the development of kinetic models for platinum-ceria-zirconia ($Pt/Ce_xZr_{1-x}O_2$)-catalysed diesel particle filter (DPF) regeneration. Such models have a practical purpose in that they can be used to calculate source terms in 3D flow models, and they also have an intrinsic interest for the understanding of the mechanisms of catalysed soot oxidation. The core of this kinetic analysis consists in estimating Arrhenius parameters of a number of detailed reaction steps by fitting calculated curves to experimental ones. In doing so, the aim is not only to understand the roles of the different reactants, but also to investigate the efficacy and limitations of the modelling procedure for gas-solid heterogeneous reactions. Principal among the examined aspects is the feasibility of attributing physically meaningful values to individual parameters in large reaction mechanisms. The problem is approached by fitting one "subset"of reaction steps at a time.

This procedure is illustrated by means of the cases of soot oxidation by NO, NO_2 and/or O_2, NO oxidation catalysed by ceria-based catalysts and soot oxidation catalysed by $Pt/Ce_xZr_{1-x}O_2$. Interesting insights are gained into the mechanisms of these reactions, since the kinetics had often not been analysed thoroughly in the relevant literature. The fitting approach is shown to be effective as it allows for reproduction of several key species profiles in each of a number of experiments. Experiments used for these kinetic studies are temperature programmed tests in a fixed bed reactor, many of which were performed during the course of the study and data concerning others taken from the literature. In order to extract kinetic parameters from the temperature programmed data, a reactor model describing gas flow through a bed of particles and a mean field model of soot and catalyst surface chemistry are developed. The role of soot structure, ceria-zirconia composition/structure and soot/catalyst ratio on reaction are considered. Parameters used to deal with their effects are estimated.

This manuscript is structured as follows. In Chapter 1, we set the context of current research concerning DPFs, consider the environmental, health related and legislative motivations behind it as well as the state-of-the-art of modelling chemistry in DPFs

and the specific issues arising in such models. The experimental setup, methods and materials are described in Chapter 2 and the modelling approach in Chapter 3. Subsequent chapters (4-6) deal with the specific reaction systems and the study of their kinetics by means of the experiments and model. Chapters 4 and 5 concern certain aspects of interest in DPF chemistry, i.e. the oxidation of soot without catalyst, and catalyst interaction with some of the exhaust gases, respectively. Chapter 6 however deals with the kinetics of regeneration in a $Pt/Ce_xZr_{1-x}O_2$-catalysed DPF as a whole.

Chapter 1

Context and Literature Review

Abstract

Dans ce chapitre, on donne des informations sur le contexte des recherches pour les FaP. En particulier, on aborde la question de l'origine des particules de suies dans les moteurs Diesel et l'on explique pourquoi la destruction des suies présentes dans les gaz d'échappement est souhaitable. Les technologies actuelles pour les FaP sont exposées dans les grandes lignes, en se focalisant sur la régéneration du filtre (c'est-à-dire l'oxydation des suies), dont la chimie est le sujet de cette étude. L'état de l'art des dispositifs expérimentaux et des méthodes associées pour étudier la cinétique de l'oxydation (catalysée) des suies est abordé et un état de l'art est également dressé en modélisation cinétique.

⋆

In this chapter, information on the context of research for DPFs is given. In particular, it addresses the origin of soot particles from Diesel engines and explains why there is a need for removal of these particles from the exhaust. Then current technologies for DPFs are briefly outlined, with a focus on the regeneration (i.e. soot oxidation) process, the chemistry of which is the topic of this study. The state of the art in experimental investigations for the kinetics of (catalytic) soot oxidation is

addressed, and similarly the state of art in modelling such kinetics.

1.1 Background on Formation and Polluting Characteristics of Soot

1.1.1 Physico-Chemistry of Soot Formation

Diesel soot particles are formed during fuel combustion at typical diesel engine operating conditions: Temperatures between 1000 and 2800 K and pressures between 50 and 100 atm and sufficient air for overalll complete combustion. In practice most soot particles are formed when locally hydrocarbons remain unburnt, condense and become precursors for solid soot particles. This first formation of precursors from the gaseous phase is known as nucleation. These particles then grow by the surface growth mechanism, which entails gas-phase molecules attaching to the carbon surface, and by coagulation of particles amongst each other. Oxidation of the soot particles may spontaneously occur at any stage of the formation process.

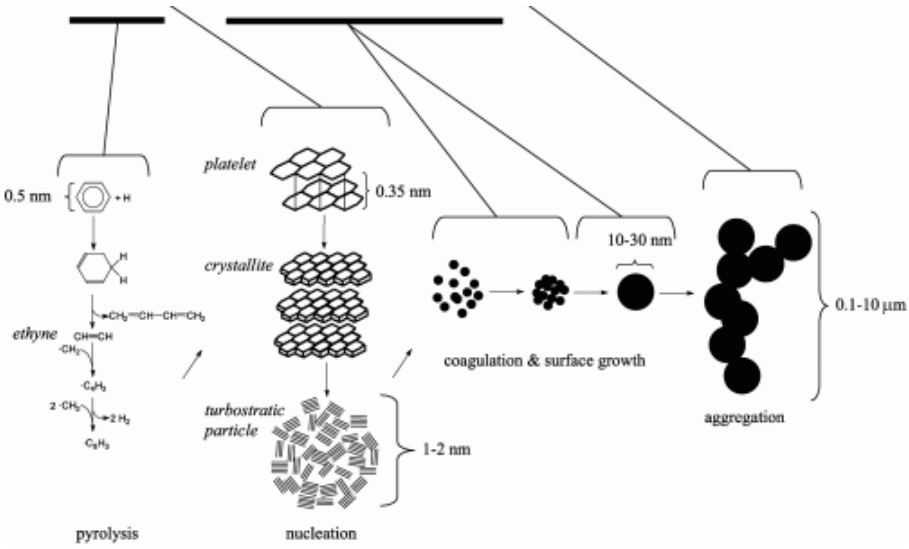

Figure 1.1: Formation of soot particles [1]

Turbostratic particles are formed by stacks of crystallites (graphene layers) (Figure 1.1), which, in turn, are formed by stacks of polycyclic aromatic structures called platelets [2, 3]. Hydrogen, oxygen and other heteroatoms are commonly present at the edges of crystallite layers [4]. Ultrafine particles are usually formed by just nucleation, which is the initial stage of the process by which several gaseous compounds react together to form a solid. These particles are a few nanometres in size but can grow up to 1 μm, either by additional gas condensing onto the particles or by coagulation (when several particles combine to form a larger particle). It has been shown that carbon black (CB) has a very similar, albeit more ordered, structure to diesel particulate matter. Many studies are therefore based on CB, which has the advantage of being produced in a reproducible manner.

1.1.2 Impact on Human Health and the Environment

Economic growth and urbanisation are leading to an ever-increasing number of vehicles on the road [5, 6]. Ambient air pollution is increasing as a consequence and international and European emission standards are being made ever-more stringent. Road transport is a major source of pollutant emissions, while other sources include stationary combustion plants, industrial processes and forest fires [3].
Some of the more common pollutants found in the atmosphere include:

- Particulate matter (PM) is the generic term for a broad class of chemically and physically diverse substances that exist as discrete particles (liquid droplets or solids) over a wide range of sizes. Particles originate from a variety of man-made stationary and mobile sources as well as from natural sources. Particles may be emitted directly or formed in the atmosphere by transformations of gaseous species such as sulfur oxides, nitrogen oxides, and volatile organic compounds (VOC). The chemical and physical properties of PM vary greatly with time, region and source, thus complicating the assessment of health and environmental effects. Common particle pollutants include dust, dirt, soot and smoke. Particulate pollutants are very diverse in terms of size. The US Environmental Protection Agency (EPA) distinguishes between "inhalable coarse particles," with diameters larger than 2.5 micrometers and smaller than 10 micrometres and "fine particles," with diameters that are 2.5 micrometres and smaller [7].

The size of particles is directly linked to their potential for causing health problems. Small particles less than 10 micrometers in diameter pose the greatest problems, because they are more likely to penetrate the lungs and get into the bloodstream [7]. These include Diesel Particulate Matter. Fine particles (2.5 micrometres and smaller) are the major cause of reduced visibility (haze) in parts of the United States [7]. Particles with a diameter smaller than 10 μm (PM10) are most frequently used as an indicator and therefore often found in statistics. On the other hand, PM2.5 is a better indicator of risk to health and likely also a better for anthropogenic particles [3].
Polluting particulate matter also varies greatly in chemical composition and includes carbonaceous particles such as those emitted by burning fossil fuels and biomass and non-carbonaceous particles like mineral fly ash and fragments of rock and dust.

- Carbon monoxide: CO is a colourless, odourless gas that is formed during incomplete combustion of fossil fuels. CO originating from motor vehicles make up about 56 percent of all CO emissions in the USA [7]. Other sources of CO include industrial processes, residential wood burning, and natural sources such as forest fires. Woodstoves, gas stoves and cigarette smoke are sources of CO indoors. CO is harmful to humans at high concentrations, because it reduces oxygen supply to the heart, brain and other tissues. It is therefore particularly dangerous for individuals with heart disease and can negatively affect the central nervous system [7].

- Nitrogen oxides: NO_2 is the component of greatest interest and the indicator for the larger group of nitrogen oxides. In addition to contributing to the formation of ground-level ozone, NO_2 contributes to the formation of OH and, subsequently, ozone in the troposphere [8]. EPA set standards for NO_2 at 0.053 parts per million (53 ppb), averaged annually [7], and fine particle pollution, NO_2 is linked with a number of adverse effects on the respiratory system. Current scientific evidence links NO_2 exposures with adverse respiratory effects including airway inflammation in healthy people and increased respiratory symptoms in people with asthma. NO_x anthropogenic emissions

are mainly due to road transport, as well as agriculture and industry.

- Sulphur dioxide: Sulphur dioxide (SO_2) is a highly reactive gas. The largest sources of SO_2 emissions are from fossil fuel combustion in power plants (66%) and other industrial facilities (29%) [7]. Current scientific evidence links exposures to SO_2 with a number of adverse respiratory effects, including bronchoconstriction and increased asthma symptoms. EPA has set a 24-hour standard at 140 ppb and an annual average standard at 30 ppb.

- Volatile organic compounds (VOC) include a wide range of gas-phase hydrocarbons, oxygenates, halogenates and other carbon compounds [3]. Main sources of atmospheric VOC are leakage from pressurised systems and fuel tanks and incomplete combustion of fossil fuels [3].

- Ozone: Ozone (O_3) is usually not emitted directly into the air, but created at ground-level by a chemical reaction between NO_x and volatile organic compounds (VOC). In the earth's lower atmosphere, ground-level ozone is undesirable. Motor vehicle exhaust and industrial emissions, gasoline vapours, and chemical solvents as well as natural sources emit NO_x and VOC that help form ozone. Ground-level ozone is the primary constituent of smog. Sunlight and hot weather cause ground-level ozone to form in harmful concentrations in the air. As a result, it is known as a summertime air pollutant. Ozone occurs naturally in the stratosphere and forms a layer that protects life on earth by preventing high-energy radiation from reaching the troposphere.

According to the EPA [7], numerous scientific studies have linked exposure to PM to the following symptoms: respiratory problems[1], decreased lung function, aggravation of asthma, chronic bronchitis, an irregular heartbeat, nonfatal heart attacks and premature death in people with heart or lung disease. The smallest particles can be considered the most dangerous, because of the ease with which they can

[1] irritation of the airways, coughing, breathing difficulties.

penetrate the lungs. They also have a large area/volume ratio, which means that they can efficiently carry other toxic substances, such as heavy organic molecules and transition metals (e.g. vanadium) which may be present in PM, the latter of which has been linked to internal lesions, while the former may be carcinogenic [9]. Polycyclic aromatic hydrocarbons (PAHs) on the particle surface are considered to have inflammatory properties and cause allergic reactions [9]. Exposure to PM affects different people differently [7], [10]. Long-term exposure to PM leads to a significant reduction in life expectancy (12-14 % increase in risk of death) and is therefore more relevant to public health than short-term exposure [11]. Thresholds below which adverse effects on health do not occur have not been identified, because current PM concentrations are often already a risk for health [3]. The exposure guidelines recommended by the World Health Organization (WHO) can therefore not provide full protection. According to the French Minister of Environmental Affairs, Chantal Jouanno, "fine particles will in future be one of the major problems in air quality, as they are responsible for 30000 premature deaths in France and 300000 in Europe." [12]. Particle deposition in the lungs ([13]) has been shown to trigger inflammation and increased clotting ability of platelets, and nanoparticles in particular are easily adsorbed into the lungs' alveoli and impair the ability of the organism to remove foreign particles. Carbon nano particles have also been shown to be cytotoxic (i.e., to kill human cells in culture) [13]. Lastly, it has been reported recently that soot particles in the atmosphere are in fact not inert, but that solar radiation drastically enhances the particles' reaction with NO_2 and subsequent conversion to HONO. This presents potential hazards to the environment and human health by potential formation of nitro-PAHs known for their toxicity [8].

While the Kyoto Protocol of 1997 did not take into account the global warming potential of soot, it has in fact been shown that a reduction of black carbon emissions could slow down global warming more than any reduction of CO_2 and CH_4 emissions [14]. According to calculations by Jacobson (2002), 20-45 percent of net global warming could be eliminated within 3-5 years. Reducing CO_2 by a third would produce the same change, but after 50-200 years [15]. Solid particles present in the atmosphere under form of aerosols may have either cooling or heating effects [16]. Black carbon deriving from fossil fuels has a warming effect because it tends to absorb

Table 1.1: EPA 2006 National Ambient Air Quality Standards (NAAQS) for fine and coarse particles, averaged over 24 h and annually [μ g/m^3], [7]

	24 h	annual
fine	35	15
coarse	150	

incoming solar radiation and then warm the surrounding atmosphere, whereas particles derived from the burning of biomass have a cooling effect because they reflect solar radiation back into space. Apart from these direct effects, aerosols may also cause radiative forcing via an indirect effect by changing the properties of clouds, such as their lifetime. This may cause problems on a local, rather than global scale. Soot also produces radiative forcing by lowering the reflectance of ice and snow [14]. PM containing hydrocarbons and elemental carbon (EC) soils all sites on which it deposits, including those of important cultural heritage. Inorganic elements (silicates, metals) contained in airborne particulate matter also impacts on the surfaces of historical buildings and monuments, causing mechanical abrasion and corrosion [17]. Soot deposits on buildings constitute, together with other organic compounds, a medium for the absorption of damaging gases like SO_2 [18].

1.2 Pollution Regulations: Particulate Matter

In the USA, the Clean Air Act requires EPA to set air quality standards to protect both public health and the environment (e.g. crops, vegetation, visibility). PM affects both. The latest US emission standards can be seen in table 1.1

In Europe, the emission standard Euro 5 entered into being in September 2009. Its main goal is to reduce the emission of particulate matter from diesel cars from 25mg/km to 5mg/km. Euro 6 is scheduled to enter into vigour in January 2014 and will mainly lead to the reduction of NO_x emissions from diesel cars [19].

Table 1.2: EU emission standards for passenger cars (Category M_1), g/km [19]

	Date	CO	HC	HC+NO_x	NO_x	PM
Compression Ignition (Diesel)						
Euro 1[†]	1992.07	2.72(3.16)	-	0.97(1.13)	-	0.14(0.18)
Euro 2, IDI	1996.01	1.0	-	0.7	-	0.08)
Euro 2, DI	1996.01[a]	1.0	-	0.9	-	0.10
Euro 3	2000.01	0.64	-	0.56	0.50	0.05)
Euro 4	2005.01	0.50	-	0.30	0.25	0.025
Euro 5	2009.09[b]	0.50	-	0.23	0.18	0.005[e]
Euro 6	2014.09	0.50	-	0.17	0.08	0.005[e]

[*] At the Euro 1..4 stages, passenger vehicles > 2500 kg were type approved as Category N_1 vehicles

[†] Values in brackets are conformity of production(COP) limits

[a] - until 1999.09.30 (after that date DI engines must meet the IDI limits)

[b] - 2011.01 for all models

[e] - 0.0045 g/km using the PMP measurement procedure

1.3 DPF Technology

In the light of progressively tightening air quality standards, much research is devoted to the development and control of aftertreatment technologies for diesel engines. However, the development of exhaust gas treatment technologies still represents a challenge. DPFs physically capture diesel particulate matter. The main technology in use is the wall-flow monolith, which is composed of many parallel channels. Adjacent channels are plugged at opposite ends, so that an open channel will always be surrounded by plugged channels. As can be seen in Figure A.1a, this forces the reactive gas to flow through the porous channel walls. Consequently, solid particles in the flow are deposited on the porous material, Figure A.1b. This type of filtration can occur via two mechanisms [19]: Deep bed filtration, which occurs by inertial or diffusional deposition of particles on the porous medium, and surface filtration (cake filtration), which occurs when particles are larger than pore diameters, so that particles are trapped by sieving. During soot loading, deep bed filtration initially occurs, then giving way to the cake filtration regime [20].

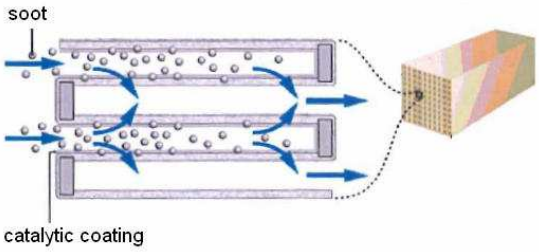

(a) Schematic diagram of a DPF monolith [21]

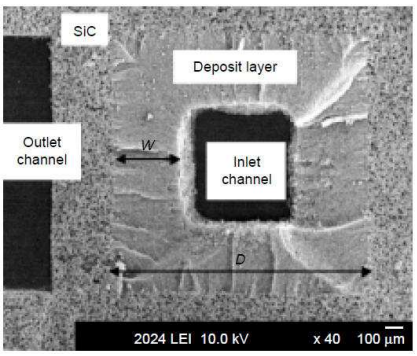

(b) Scanning electron micrograph of the fractured edge of a loaded DPF [22]

Figure 1.2: Wallflow monolith

The so-called cake, formed by the soot particles accumulating on the filtrating medium, grows in size, and consequently the pressure drop over it grows, in a non linear fashion[2] [20]. To avoid this pressure drop reaching excessive levels, the accumulated soot particles are removed in a process known as filter **regeneration**, i.e., the soot cake is oxidised to form gaseous products. Diesel particulate spontaneously burns in air at about 500 - 600 °C [24]. This temperature range is not regularly achieved in typical diesel vehicle applications for sufficient periods of time to enable self-regeneration. Due to the low temperatures (150 - 240 °C) of diesel exhaust gases and the high activation energies (100 - 210 kJ/mol) of the soot oxidation reaction, catalysts are usually used.

The task of regeneration can be faced following two different approaches: either the exhaust gas and/or the filter is heated up to the particulate ignition temperature, or the ignition temperature is lowered with the aid of substances which catalyse soot oxidation. In the former, the exhaust gas temperature can be raised by the occasional post-injection of fuel that gets burned in a honeycomb oxidation catalyst placed up-stream of the DPF or using an external heating system [1]. The filter can also be heated up by means of electrically-driven devices or burners [24]. Concerning the catalysed approach, there are two alternatives: organic derivatives of

[2]The non linearity of the pressure drop profile is due to the succession of the different filtration regimes: deep-bed, mixed, and surface filtration [23]

active metals may be used as fuel additives, or the catalyst can be deposited directly onto the filter surface. EURO V regulations enforce the latter solution since 2008 [24].

The chemistry of particulate oxidation is complex due to the varied character of soot, the formation and migration of surface complexes on both soot and catalyst and the modification of chemical properties of soot due to exposure to high temperatures (annealing) [25], amongst other factors detailed in the following section. Chemical reaction can also be influenced directly by geometrical factors, such as the form of catalyst, which have direct influence on the importance of mass transfer [26].

At temperatures above 500 °C, several issues arise in DPFs: Reaction kinetics may change somewhat, different reactions, such as those with radicals ($OH^{\bullet}$) may occur [27]. Thermal transfer, in particular by radiation, becomes important (T^4). It may be necessary to take this into account to accurately predict temperature gradients, the latter being required to describe and predict thermal problems such as local hot-spots.

This latter phenomenon is one of several aspects, which can be captured more accurately by a 3D description. Hot-spots arise if an excess of soot is collected on the filter or if the flow in each channel of the DPF is not uniform in the radial direction (maldistribution), causing an unevenly distributed layer of soot particles on the filtering wall. The exhaust gas temperature then rises due to the increased back pressure, and this leads to a sudden burn off, which might cause the filter temperature to rise above the melting point of the filter itself (thermal runaway) [24]. Flow maldistribution may be linked to DPF geometry: the pulsating flow of the engine along with the geometry of the manifold creates highly non-uniform inlet conditions [28]. Such an occurrence also has a negative influence on conversion of the pollutants and leads to partial utilisation of the catalyst surface [28]. In addition, it is important to accurately calculate the temperature distribution in the DPF in order to account for its thermal durability over its lifetime [28]. 0D or 1D (multi-0D) models cannot take these mal-distribution effects into account as they use average flow parameters [28].

Manufacturers have identified a need for a software prediction tool to assess the behaviour of such DPFs in the early design phase. Ideally, it should take into account the condition of a given car's exhaust, the mileage of the car, its filter size and its filter shape in a flow modelling tool [29]. The ability to predict the local regeneration behaviour and thereby avoid excessive local temperatures is a major requirement for the design of diesel filters consisting of less expensive but more temperature sensitive material [29]. A practically useful description of the reactive flow in a DPF is challenging. On the one hand, the complex character of the heterogeneous soot oxidation reaction and three dimensional flow phenomena call for detailed chemical mechanisms and flow models. On the other, the amount of computational time needed to model the complete system in such detail me would make it very difficult to use such a model in on-board control and even for development applications.

The European law limits will almost certainly bring about the use of active means to occasionally raise filter temperature. This will most likely imply a fuel penalty of the order of 4% [24]. Future targets in DPF development thus include finding the technological means to reduce or even eliminate this fuel penalty by both catalyst and trap development, lower soot ignition temperatures and lower DPF pressure drops [24].

1.4 Chemistry and Kinetic Modelling for DPFs

1.4.1 Non Catalytic Oxidation of Soot

Kinetics

A number of the components of Diesel exhaust fumes are relevant for DPF regeneration. Amongst the most prominent ones are O_2, NO_2, NO, CO, H_2O and various hydrocarbons because of their affinity for reaction with soot or with the catalysts commonly present in DPFs. Reaction with gaseous SO_2 and H_2O assists in the process by forming acids which are good oxidants. The reactions considered here are those with NO_2, NO and O_2.

At low temperatures a mixture of NO and O_2 will equilibrate to include significant amounts of NO_2 below 500 °C and N_2O_4 below 100 °C. The magnitudes of the reaction rates are found to be: $NO_2 > N_2O \approx NO \approx O_2$ [30]. All of these reactions proceed via adsorption of gas phase molecules onto the solid carbon/catalyst surface, forming weak bonds (physisorption) or stronger bonds (chemisorption). The latter give rise to surface species such as are nitro groups, alkyl nitrates and nitrate esters, carboxylates, anhydrides and lactones. The most detailed mechanism with estimated parameters for the C-O_2 reaction is that of Miessen [31, 32], shown in Figure 1.3. It involves six intermediate surface species and two types of site: edge sites, i.e. those located at the edge of graphene sheets and more reactive, and bulk sites, located in the midst of the graphene sheet. These sites interact with gas phase O_2, CO, CO_2 and O atoms to produce six different type of SOC, which may further interact with each other and with gas phase molecules. Each elementary step is assumed to follow a modified Arrhenius law $k(T) = AT^{\beta} \cdot e^{-\frac{E_a}{RT} f(\theta_n)}$, and the kinetic parameters are taken from various sources in literature (R1,4: Kelemen 1985; R2,3: Hayns 1975; other parameters are estimated).

Analysis of the products of the C-NO_2 reaction shows the presence of CO_2, NO and N_2. The global reactions

$$2\ NO_2 + C \rightarrow 2\ NO + CO_2$$
$$NO_2 + C \rightarrow 1/2\ N_2 + CO_2$$

are proposed. Several studies [30] report that the C-NO_2 reaction is enhanced by the presence of water vapour. However, this increase in rate diminishes as temperature is increased. The promoting effect is attributed to the formation of nitric and nitrous acids. Jacquot et al. [33] find that soot oxidation with NO_2 is enhanced by the presence of O_2. Water, CO_2, O_2 and nitrogen oxides are all present to some degree in Diesel exhaust gases and may therefore play a role in DPF regeneration. However, most studies focus on soot oxidation by O_2 and also NO in catalysed regeneration. This choice is based on the fact that CO_2 and H_2O are much less reactive towards carbon materials [34] at low temperatures. Globally, experiments show that

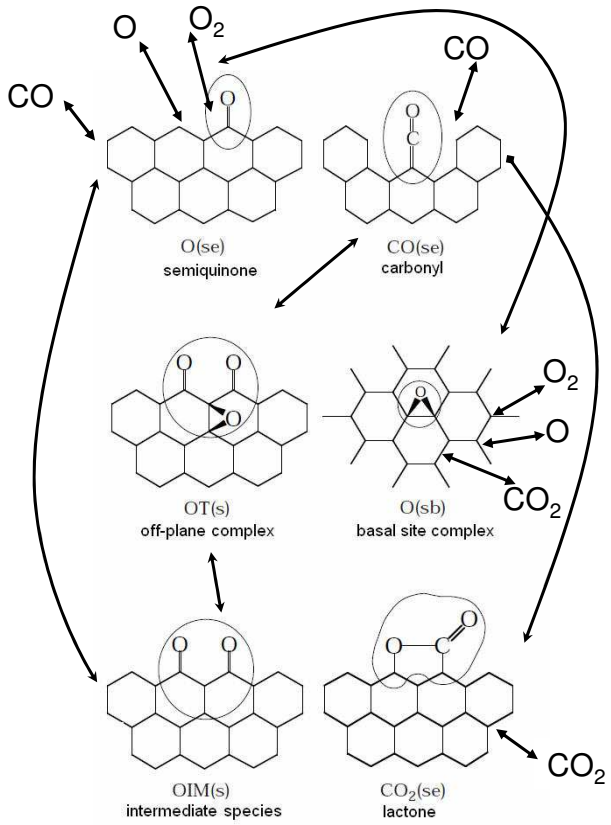

Figure 1.3: Surface mechanism, based on that of Miessen [32]

the non-catalytic carbon-O_2 reaction leads to carbon dioxide and carbon monoxide as products. Neeft et al. [35] and Yezerets et al. [36] are among those who propose the following global reactions:

$$2\ C + O_2 \rightarrow 2\ CO$$
$$C + O_2 \rightarrow CO_2$$

The global reaction rate is written as

$$r = k(T) \cdot C^n_{oxidant} \tag{1.1}$$

where the rate constant $k(T)$ is usually described by a simple Arrhenius law

$$k(T) = A \cdot e^{-\frac{E_a}{RT}} \tag{1.2}$$

or a modified Arrhenius law,

$$k(T) = AT^{\beta} \cdot e^{-\frac{E_a}{RT}} \tag{1.3}$$

Global activation energies for soot oxidation with O_2 range from 140 to 170 kJ/mol [37]. Hurt and Calo [38] find E_a=105-180 kJ/mol and Reichert et al. 100-210 kJ/mol from a review of literature. Reaction order n with respect to O_2 varies strongly with temperature. At higher temperatures (ca. 2230 °C) it is mostly assumed equal to 1 [39] and equal to zero at lower T (ca. 130 °C) [40].

The heterogeneous carbon-O_2/NO_x reaction is complex, as it involves several intermediate steps, intermediate (surface) species and active carbon sites. The surface complexes generated during reaction are numerous and therefore characterised by a distribution of chemical properties. Their characteristics depend, amongst other factors, on microscopic irregularities in the chemical structure of soot surfaces. Many modelling studies treat the surface species as having uniform kinetic properties, in what are termed **lumped kinetic models** while others [41, 4, 42] consider the distribution of kinetic parameters. When numerous surface complex species are present, a number of CO_2 and CO peaks may be produced, with activation energies of desorption of 115-380 kJ/mol [43]. The reaction occurs with a so-called "turnover mechanism", in which active sites are regenerated when a carbon atom is consumed to form a gaseous product, thereby making it possible to access a lower layer of carbon atoms. Surface species may migrate and interact with each other. Both mobile

and immobile complexes may be formed, the mobile ones being due to ionic bonding, and the immobile ones to covalent bonding. These latter covalent bonds are characteristic of carbonyl, ether, lactone and acid anhydride functional groups [42]. The migration of oxygen complexes has been established by the work of Marsh and Haynes [42]).

The CO/CO_2 product ratio of the C-O_2 reaction depends on temperature [44]. Campbell and Mitchell [42] find that during oxidation of char CO formation predominates at higher temperatures, and CO_2 at lower temperatures. For modelling the CO/CO_2 ratio, it is important to attribute the formation of CO and O_2 to the correct reactions. Two main pathways have been proposed, the Eley-Rideal direct interaction of an active carbon site with O_2 and an interaction between SOCs. According to Hurt and Calo [38], the direct interaction of SOCs with O_2 (Eley-Rideal) is predominantly responsible for CO_2 formation: $2\ C^*(O) + O_2 \rightarrow 2\ CO_2$. Experimental evidence is cited, such as the high CO/CO_2 ratio in desorption experiments in a vacuum. Others propose reaction between SOCs: $2\ C^*(O) \rightarrow CO_2 + C^*$, but this is based exclusively on DFT calculations and global considerations are neglected [45].

An important consideration when trying to estimate kinetic parameters is that the global oxidation rate will be limited by the slowest step of the mechanism. According to Hurt and Calo and others [38, 46], activation energies for CO and CO_2 desorption assume the larger values than adsorption step energies, suggesting that formation of CO and/or CO_2 are the rate limiting steps in the temperatures of interest to DPF regeneration (T = 350-14000 °C) (Figure 1.4).

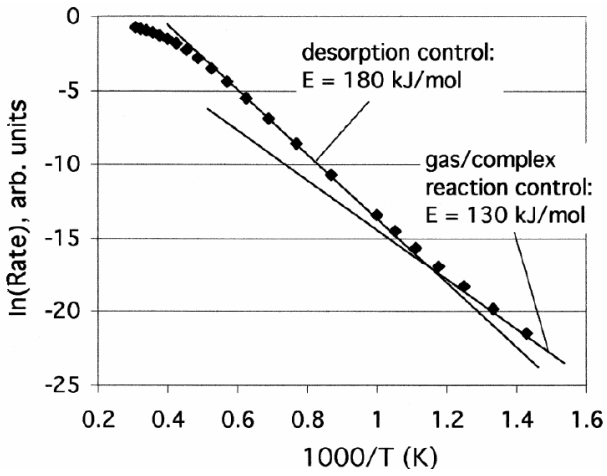

Figure 1.4: Global Arrhenius diagram and rate determining regimes of carbon oxidation [38]

Chemical Structure of Soot and its Relation to Reactivity

Diesel soot typically is made up of approximately spherical primary particles with diameters of the order of 10-30 nm [47], which aggregate in chain-like structures [37]. Each of these particles contains:

- a graphitic carbon matrix making up the carbon nucleus of each of the particles. This elemental carbon is arranged in graphene sheets, which form a wavy, multi-layered structures giving rise to the name turbostratic particles.
- organic compounds (including unburned hydrocarbons, oxygenated hydrocarbons and polynuclear aromatic hydrocarbons), which at temperatures below 500 °C tend to condense and become adsorbed on the carbon nucleus.
- a small amount of inorganic ash (mineral and metallic substances originating from engine lubricant and engine wear

Particulate matter is usually partitioned with an extraction solvent; this allows further classification into a soluble fraction and a dry-soot fraction [48].

In kinetic modelling, the structure of the soot is important because of its relation to soot reactivity and the following paragraphs aim to expose the correlation be-

tween reactivity and various structural parameters. Reactivity is in fact dependent on chemical or nano structure (in particular the degree of graphitisation), as well as bulk properties such as porosity, H/C ratio and inorganic impurities (mineral matter). These bulk properties may in turn be dependent on the nano structure [49]. In a discussion of soot structure, it can be of interest to consider the spectrum of carbonaceous materials. The latter may be seen as being delimited by graphite, on the end of highly ordered carbons, and amorphous carbon on the end of highly disordered carbons. Graphite is a form of pure carbon consisting of layers of hexagonally arranged carbon atoms in a plane (graphene layers). These layers are stacked parallel to each other at a distance of 3.3354 Å (0.0335 nm) in a three-dimensional crystalline long-range order [47, 49]. The chemical bonds within the layers are covalent with sp^2 hybridisation [50]. Amorphous carbon is a carbon material without long-range crystalline order. Exposed edge sites and defects are characteristic of disordered, amorphous carbons. The forms of carbon existing in between graphite and amorphous carbon are many and varied and their chemical structure may be characterised by their degree of graphitisation. Graphitised carbons tend to have more orderly stacked crystallite layers and consequently fewer exposed active sites. Sometimes an irregular structure may evolve to become more regular, particularly when the material is subjected to higher temperatures ($T \geqslant$ 700-1100 °C [51]). This process, known as graphitisation or thermal annealing[3], often occurs during soot formation, as seen in Figure 1.5.

[3]Note that the term annealing has also been interpreted as the process of closing a 5-membered ring in place of an active site [52].

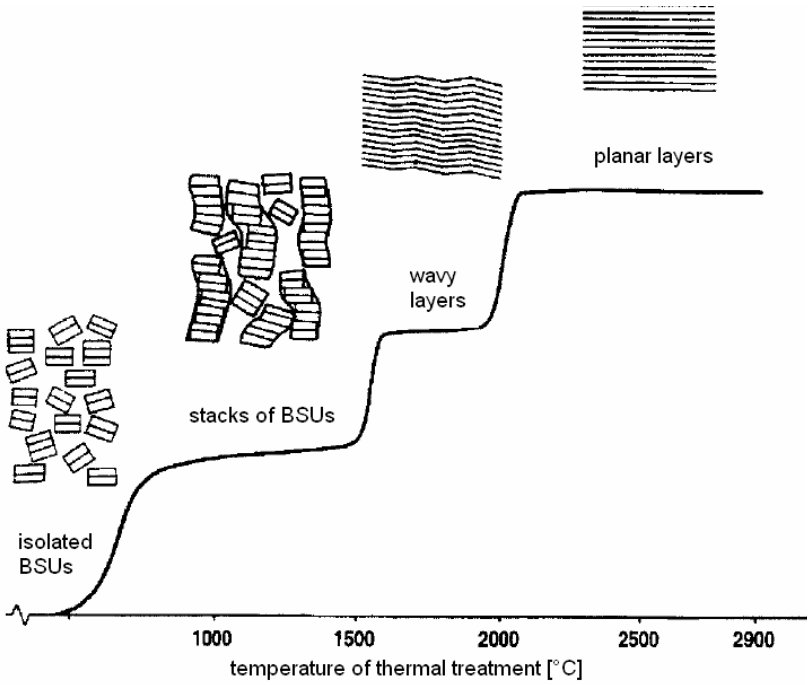

Figure 1.5: Various steps of graphitisation [53]

Chemical structure influences reactivity via number and location of active sites [51] and seems to be the predominant factor determining the reactivity of a carbon material. For e.g., coal rank, i.e., degree of graphitisation, has been found to be the main factor influencing reactivity of coals and their derived chars [54]. Indeed, reactivity has been found to be higher on carbon surfaces containing many exposed edge sites (mainly amorphous carbons) [4] and a linear relation between coal rank and the pre-exponential factor A of the coal oxidation reaction has been identified [55, 56]. Similarly, Vander Wal and Tomasek [57, 49] attribute the loss of reactivity with higher degrees of graphitisation to the fact that ungraphitised carbons have shorter graphene layers, and, therefore, a higher proportion of atoms in edge positions. These edge sites are more easily accessible than basal sites, and this leads to a higher overalll reactivity. Soot formed at higher temperatures can be expected to have a lower intrinsic reactivity, due to loss of active sites [51] and lower BET surface area [58]. Figure 1.6a shows a TEM image of a diesel soot particle, highlighting its onion-like turbostratic structure. Part b of this figure also shows how soot particles are composed of a relatively disorganised (amorphous) core containing fine particles

(3-4 nm) [58, 47, 49] and an external shell of neatly arranged concentric crystallite layers. The reactivity of diesel particulate matter is therefore to be expected within the spectrum of carbon materials, somewhere in between graphite and amorphous carbon [59].

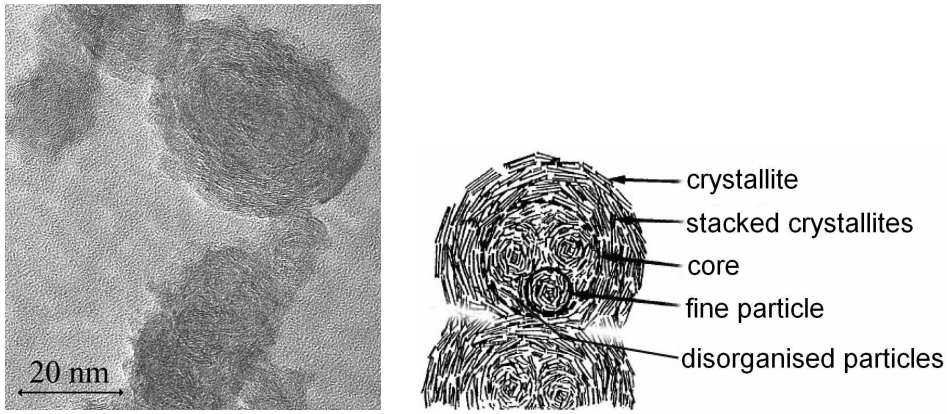

(a) TEM of soot particles [37] **(b)** Internal structure of a turbostratic particle [37]

Figure 1.6: Structure of soot particles

A parameter that can be correlated with activity, is the curvature of graphene segments, as observed, for example, by Knauer et al. [60] employing high-resolution transmission microscopy (HRTEM). Curvature, being defined as the ratio between the length of the segment as observed in HRTEM images and the shortest distance between its terminal points, is an indicator of the degree of graphitisation. Greater values of curvature indicate a lesser degree of order, higher defect content and thus higher functionalisation and reactivity [60]. According to Vander Wal and Tomasek [57] and Jones [52], for a given segment length, higher curvature of graphene layers is due to the presence of 5-membered rings, which indicates weaker C-C bonds and therefore increased bulk reactivity. Ideal graphitic lattices are planar hexagonal structures of sp^2-bonded carbon atoms, with a bond angle of 120 °[47, 53]. Differences in atomic arrangement and degree of organisation give rise to very different

forms of carbon, which are characterised by very different physical and chemical properties [53]. The degree of hybridisation of a carbonaceous material, defined by Equation 1.4 as the percentage of sp^2-bonded carbon, is in fact positively correlated with the degree of graphitisation, as Knauer et al. observe by electron energy loss spectroscopy (EELS) [49]. UV-Vis spectroscopy may also be used to investigate the electronic structure. High UV-Vis adsorption values indicate large proportions of sp^2-bonded carbons [49].

$$sp^2 = \frac{\left[\frac{area(\pi*)}{area(\pi*+\sigma*)}\right]_{sample}}{\left[\frac{area(\pi*)}{area(\pi*+\sigma*)}\right]_{100\%sp2ref}} \tag{1.4}$$

Raman microspectroscopy (RM) may be applied to soot and related carbon materials to extract the two bands of spectroscopic intensities, G and D, representative in general of graphitic and non graphitic (defect) content [58, 60]. G is the only band of intensities found in pure graphite and it has a characteristic full-width at half-maximum (fwhm) of 50 cm^{-1} and a peak located at 1580 cm^{-1}. The character (i.e. relative intensity and fwhm) of D on the other hand, varies between different carbon materials. Knauer et al. go even further and distinguish four different components of D, each responsible for different aspects of non graphitic behaviour (Figure 1.7). In particular D1, which can provide information on non-graphitic carbon content such as heteroatoms or the edge of a graphene layer [47] and D3, which provides information on structural order [60, 58]. According to Sadezky et al. [47], the applicability of RM parameters as distinguishing features of carbon materials may however be limited by the heterogeneity of these materials.

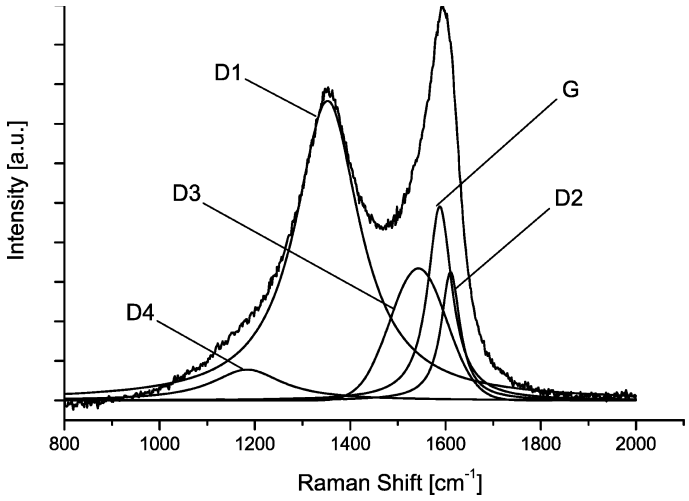

Figure 1.7: Raman spectrum of untreated EURO VI soot [60]. The G peak is representative of graphitic content, whereas D1, D2, D3 and D4 indicate defect content.

Alfè et al. [49] choose to describe the degree of graphitisation of various types of soot by parameters quantifying the graphitised portion of the soot particles. These portions are also known as basic structural units (BSU) or coherent domains and are described by the number of parallel stacked graphene layers, N, their diameters, L_a, their heights L_c and the mean interlayer spacings, d. The authors visually evaluate these geometrical characteristics from fringe lengths in transmission electron microscope (TEM) images, hypothesising a random distortion ratio of 40% and taking the mean over 15-20 images. It is found that the d is almost the same for all types of investigated soot (0.38 nm), although it is significantly different from the value typical of graphite ($d_{graphite} = 0.3354$ nm). The remaining BSU parameters are in some instances dissimilar for different soots, and in others quite similar. It is recalled that smaller values of L give rise to a higher proportion of edge atoms, which being more easily accessible, are more reactive [57].

Oxygen and hydrogen sites likely promote carbon reactivity since chemisorption on non aromatic sites is usually favoured compared to aromatic sites [51, 58]. Heat treatment and ageing, apart from ordering crystallite layers, provokes the loss of O and H atoms, most of the oxygen being lost at temperatures $\leq$ 700 °C and most

hydrogen atoms above this temperature. [51, 49]. H/C ratio as a bulk property is dependent on nano structure, i.e. degree of graphitisation. Thus soot formed at high temperatures is likely to have a lower H/C ratio and therefore be less reactive[58]. Soot with higher H/C ratios also has higher values of aromaticity. The aromaticity is defined as the ratio of carbon atoms in aliphatic side chains versus carbon in aromatic rings, as deduced from the areas under the curves in an X-ray diffractogram. When H and O atoms are lost, aromaticity increases, as does the proportion of sp^2-bonds. High aromaticity is indeed also an indicator of low reactivity [58].

Soot particles are characterised by limited overalll porosity and absence of micropores [58]. Porosity controls the accessible surface area and diffusion rates (the latter in turn control reactant concentrations). It is worth noting that there is a certain correlation between chemical structure and microporosity, as the imperfect arrangement of crystallite layers in amorphous carbons is responsible for micropores [4]. Larger pores on the other hand, tend to be of physical origin, rather than due to chemical structure.

Trace elements may act as catalysts, thus increasing overall soot reactivity. These impurities are essentially located at crystallite edges [51]. Table 1.3 synthesizes the structural properties which may be connected with material reactivity. For practical use, a macroscopic property such as H/C and O/C ratio would be most suitable for describing the effect of structure on oxidative reactivity.

A compilation of global rate constants for different carbon materials (Figure 1.8) demonstrates how reactivity varies according to the nature of the carbon material.

Kinetic models describing the surface reactions of carbon oxidation may not always take into account the exact nature of the intermediate SOCs and their differing reactivities. Thus the energetics of the carbon surface are often described by average properties, when in actual fact each complex possesses different kinetic parameters. To take into account this dispersion of kinetic parameters without adding further species participating in the equations, some authors have introduced the concept of distributed activation energies. Thus one single complex C*(O) may possess a

Table 1.3: A summary of some important structural parameters of carbonaceous materials

Nano parameters	
variable	**measure**
aromaticity	X-ray diffraction
H aromaticity	
sp^2 hybridisation	EELS, UV-Vis
cluster size	
curvature of graphene layers	HRTEM
number of graphene layers in BSU	TEM
length of graphene layers in BSU	TEM
height of graphene layers in BSU	TEM
interlayer spacing in BSU	TEM
micro porosity	

Bulk properties	
variable	**measure**
H/C	RM
particle porosity	
particle density	HRTEM
ASA, TSA	
BET	
particle diameter	

Material formation conditions	
variable	**measure**
temperature at formation	
residence time at formation	
maturity	

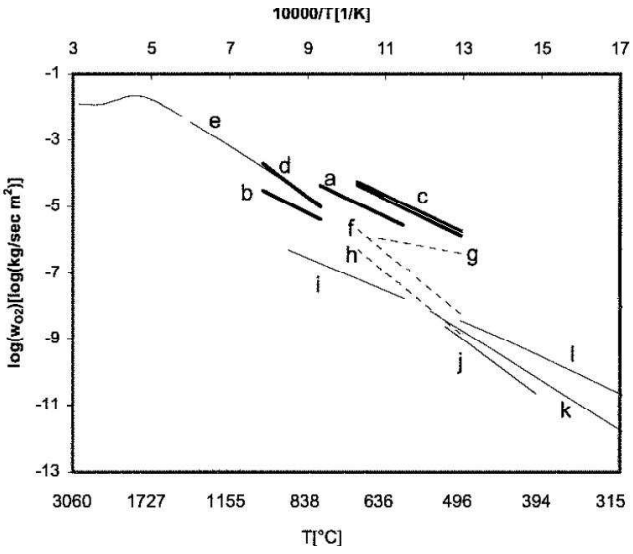

Figure 1.8: Arrhenius diagram of the specific rates of carbon particle oxidation (Jung et al.). (a)Diesel soot from fuel with 2 percent lube oil, (b)Diesel soot, (c)Fuel with Ce additive, (d)Diffusion flame soot, (e)graphite, (f)Ca-catalysed diesel soot, (h)uncatalysed diesel soot, (i)carbon black, (j)Printex-U flame soot, (k),(l)Diesel particulate [61]

broad range of activation energies [41, 4, 42] described by the function $f(E)$, where $f(E)\Delta E$ is the fraction of the population of C*(O) complexes having activation energy comprised between E and $E + \Delta E$. Integration over all E yields unity, $f(E)dE = 1$. Use of $f(E)$ instead of a single value of $E = E_0$ leads to a more general equation, which contains the specific case

$$f(E) = \delta(E - E_0) \Rightarrow \int_{E_{min}}^{E_{max}} f(E)A \cdot exp\left(\frac{-E}{RT}\right) dE = A \cdot exp\left(\frac{-E_0}{RT}\right) \qquad (1.5)$$

Such a distribution of activation energies may be implemented for any of the reactions present in a surface mechanism, but information in literature mostly concerns the simple CO formation step. In fact, the characteristic parameters of a distribution of activation energies for the above reaction may be determined via temperature programmed desorption experiments (TPDs). It has been shown that the probability of a SOC having a specific energy of desorption is approximately Gaussian [42].

Physical Soot Structure and its Relation to Reactivity

The reaction rates measured during experiments are not necessarily equal to the intrinsic rate of chemical reaction, but may actually be representative of some other process, such as transport phenomena [62]. Oxidation of a carbon particle is in fact a succession of several phenomena: Diffusion of gaseous reactants across the boundary layer to the particle surface, diffusion of reactants in the pores of the solid particle, adsorption of reactants onto the solid's surface and formation of SOCs, chemical reaction on the surface, desorption of reaction products from the surface of the pores, diffusion of products in the pores, diffusion of reaction products from the external surface of the solid, across the boundary layer towards the gaseous phase [51, 63].

Several oxidation regimes are distinguished (Figure 1.9), depending on which of these steps is rate limiting, and therefore on temperature and concentrations of reactants and other operating conditions (pressure, gas velocity) and solid properties (porosity, active surface, impurities, presence of catalysts). In choosing experimental conditions and setup, it is therefore important to take temperature and concentration into account and if necessary adjust for the limiting regime by using a transport model.

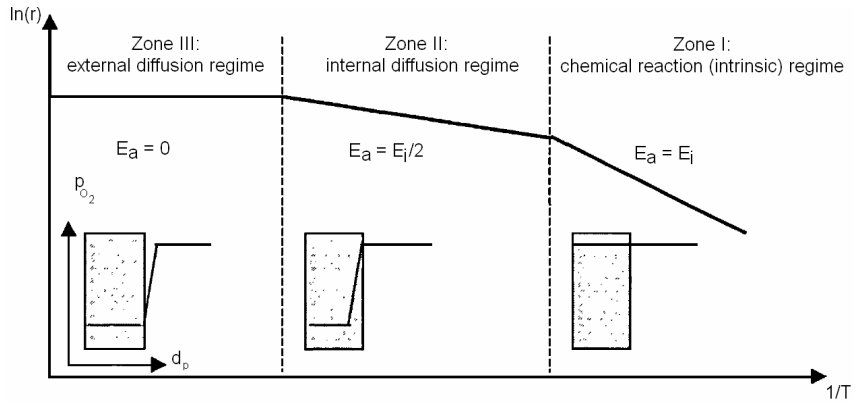

Figure 1.9: Oxidation regimes in an Arrhenius diagram. Here r = rate, d_p = particle diameter, p_{O2} = partial pressure of O_2

Zone I: At low temperatures, the rate of consumption of oxygen is only controlled by the chemical reaction and kinetic data may be determined easily as measured values correspond to intrinsic ones. Chemical reaction is relatively slow, compared to diffusion outside of the particle and inside the pores of the particle. Thus, as can be seen in the inset in Zone I, the concentration of reactant gas assumes the same value both inside and outside the porous particle. In Zone II, chemical reaction is more efficient than internal diffusion and the overalll rates are therefore controlled by this diffusion in the solid's pores. Any gas molecules which reach a pore by diffusion are immediately consumed by reaction, so that gas concentration within the pore is much lower than that outside the particle. At the high temperatures of Zone III, rates are significantly influenced by boundary layer diffusion, also making accurate extraction of kinetic parameters difficult. Reactant gas concentration is not sufficient within the boundary layer around the particle and inside its pores. If kinetic parameters were to be extracted from rates measured in the physical zones, II and III, they would not be representative of the intrinsic chemical reaction rate. For e.g., the apparent activation energy derived from the overalll rate in Zone II is $E_{app} = E_{int}/2$ and in Zone III: $E_{app} = 0$ [64].

Surface Area

In most carbon oxidation models, the surface area S_a is the area which, exposed to gaseous reactants, is covered by surface functionalities which then decompose into reaction products. It comprises the external area of the carbon particles, as well as the surface areas of accessible pores within the particle. It is sometimes modelled as evolving in time, due to opening of previously closed pores. The random pore model (Eq. (1.6)) put forward by Bhatia and Perlmutter [65, 66] describes the evolution of absolute surface area or specific surface area per unit mass [m^2/g] in function of conversion x and a structural parameter, $\psi = 4\pi L_0(1-\epsilon_0)/S_{a0}^2$, where L_0, ϵ_0 and S_{a0} are total pore length, porosity and reaction surface area per unit volume at $x = 0$ respectively.

$$S_a/S_{a,0} = \sqrt{1 - \psi \ \ln(1-x)} \tag{1.6}$$

This model assumes that pores are cylindrical and their inner surfaces make up the reaction surface of the particle. As material is consumed, the pores become larger and so do their reaction surfaces. At some point, neighbouring pores intersect, as the solid separating them is consumed and replaced by product. The global oxidation rate may thus be generalised by taking into account the influence of the evolution of surface area [1, 35]. Thus Equation 1.1 becomes

$$r_j = N_T \cdot k_j(T) \cdot C^n_{oxidant} \tag{1.7}$$

where N_T is the total number of active carbon sites, which is often expressed as

$$N_T = \Gamma S_a \tag{1.8}$$

where Γ is the active site density, charcteristic of the carbon material, and S_a, also termed total surface area (TSA), comprises the external area of the carbon particles, as well as the surface areas of accessible pores within the particle. However, the proportionality 1.8 is too simple, and probably holds for only a fraction of the TSA [35]. For this purpose, the active surface area (ASA) and reactive surface areas (RSA) have been proposed. Nevertheless, considering the definition dependent on reaction conditions and difficulty in experimentally determining these surface areas, Equations 1.8 and 1.7 are commonly used for deriving kinetic models. Both elementary and global reaction rates may be written this way. The concepts of ASA and RSA are discussed in Section 4.7. TSA can be described as a function of conversion by using an nth order model or grain model (specific case: shrinking core model), or a random pore model.

In an nth order model, surface area can be written as

$$\frac{S_a}{S_{a,0}} = (1-x)^{n_x} \tag{1.9}$$

where x is the conversion and n_x is the reaction order with respect to carbon. For $n_x = 2/3$, the nth order model is known as the "shrinking core model", because the surface area is directly proportional to the outer surface area of the carbon particle, which is assumed to be spherical.

The model is derived by Bhatia and Perlmutter for a specific reaction surface area S_a per unit volume [m^2/m^3], but may be written for surface area per unit mass [m^2/kg] as

$$\frac{S_a}{S_{a,0}} = \sqrt{1 - \psi \; ln(1 - x)} \tag{1.10}$$

by using the density of the solid and assuming that particle porosity varies linearly with conversion: $\varepsilon = \varepsilon_0 + (1 - \varepsilon_0)x$. Similarly, the expression 1.10 is valid for absolute surface area [m^2]. The dependence of surface area on conversion described by the Bhatia-Perlmutter model is shown in Figure 1.10a. The maximum in Figure 1.10a is caused by the concurrence of two opposing effects: growth of reaction area due to widening of pores and loss of reaction area due to intersection of pores. In 1.10b, $S_a/S_{a,0}$ increases monotonically, tending towards infinity for $x \rightarrow 1$, which is representative of solid mass being consumed completely towards the end of the reaction.

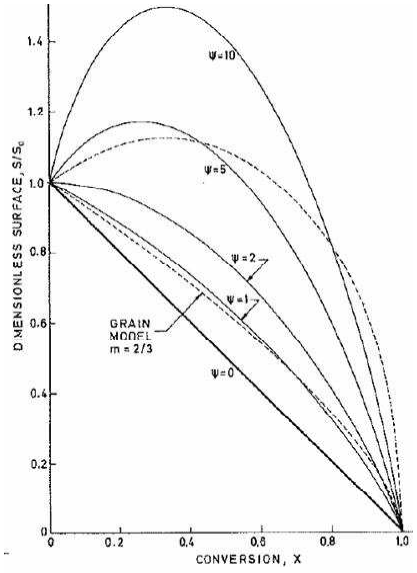

(a) S_a per unit volume (m^2/m^3) [65]

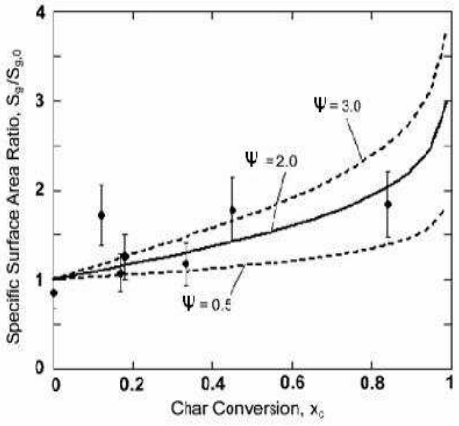

(b) S_a per unit mass (m^2/kg) [42]

Figure 1.10: Development of the specific reaction surface with conversion according to the random pore model

With reference to Figure 1.10a, it can be seen that the grain model with $n_x = 2/3$ is roughly equivalent to the random pore model with $\psi = 1$. This suggests that the concept of reaction order with respect to the mass of unconsumed solid is intimately associated with pore structure [65].

Total surface area accessible to reactant gas (TSA) is commonly determined via the BET adsorption isotherms [67]. However, it has been pointed out that BET provides a valid estimate of carbon surface areas only for average pore sizes between 0.8 and 1.1 nm [67]. Not surprisingly, BET area profiles do not agree with those predicted by the random pore or grain models, as shown by Suuberg et al. [67] in Figure 1.11. It has been repeatedly shown that BET area increases with conversion up to a certain point, where after it becomes constant [67, 37, 59]. Furthermore, BET surface areas do also not correlate well with reaction rates [67]. Suuberg proposes that micropores are not fully utilised, as presumed by the random pore model. Therefore BET area, which is generally dominated by micropore contributions should not be expected to

correlate with reaction rate.

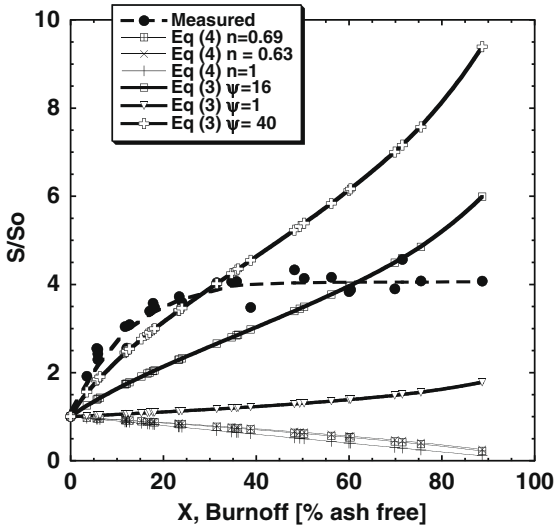

Figure 1.11: Variation of BET surface area with conversion, compared with different models of surface area variation [67]. Eq (4) and Eq(3) correspond to Equations 1.9 and 1.10 respectively.

The lack of agreement between surface models, reaction rates and BET areas could thus be explained by the inadequacy of BET as a measure for determining TSA. As an alternative explanation, the literature has divided the TSA into fractions, only one of which can presumably satisfy Equation 1.8 and be correlated with the oxidation rate of carbon particles [68]. The principal candidates are the active surface area (ASA) and the reactive surface area (RSA). These concepts are not defined in an absolute way, but rather in relation to the experimental methods with which their values may be determined. In fact, ASA is usually determined as the surface area covered by C-O complexes under low temperature chemisorption conditions, as measured by monitoring evolved CO and CO_2 during temperature programmed desorption (TPD) [69, 70]. The idea is that each complex has taken the place of a formerly active site, contributing to ASA. Of course, the precise value obtained depends on the temperature and other conditions of both chemisorption and desorption and on the duration of TPD, as not necessarily all C-O complexes have been desorbed when the TPD is stopped. This method also requires a hypothesis to be made about

the nature of the desorbed C-O complexes. When the evolution of the measured ASA with respect to conversion is to be investigated, TPD is performed on the carbon sample at different stages of conversion, that is, after partial reaction. Many investigations have been concerned with gasification by CO_2 or H_2O, and some the oxidation by O_2. It is obvious that the measured ASA values will depend on both the type of reaction that is being investigated and on the conditions in which it takes place. In this context, the RSA is introduced. Its measure presupposes that the C-O complexes may be divided into two types: stable complexes which do not participate in the investigated reaction because their activation energy is too great, and unstable intermediate complexes, which participate in the reaction thanks to a lower activation energy [69]. The latter cover sites which have contributed to the RSA. Again, RSA is determined by TPD, and depends on experimental conditions, like the ASA, and on the supposition that two types of complex exist. RSA measured in the adequate conditions was indeed found to increase monotonically with conversion.

1.4.2 Catalysed Oxidation of Soot

Catalysed Oxidation by O_2

Catalytic combustion is limited to the surface of a solid, and is under most circumstances (when particulate is not coarse etc.) limited by kinetics only (and not by mass transfer), leading to Arrhenius behaviour [71]. Thus the process can occur at very low temperatures, provided one of the reactants is activated. In the C-O_2 reaction this is preferentially O_2, which dissociates into oxygen atoms that are stronger oxidisers. Solids able to do this belong to two classes, noble metals and transition metal oxides. Good metal oxide catalysts (see Figure 1.12) must have the capability of switching very readily between two ionic valence states [71].

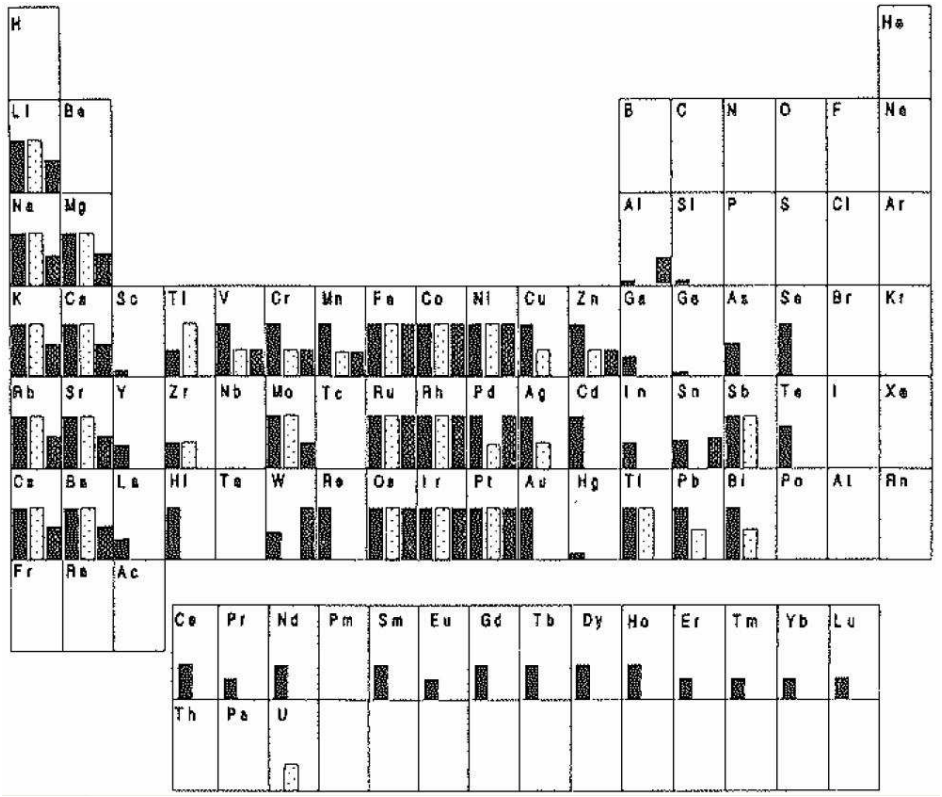

Figure 1.12: Catalytic activity for gasification in O_2 is represented by the height of the left bar for each element [72]

A literature review finds that global activation energy values for catalytic combustion by O_2 are comprised between 13 and 209 kJ/mol, compared to the 100 - 210 kJ/mol for the non catalytic reaction [37]. That is, much lower values of E_a are possible with a catalyst. Temperature of maximum oxidation rate is found to be lower by 195-314 °C [37].

Most research on diesel particulate filters focuses on catalytic filter regeneration, as the application of catalysts can significantly lower ignition temperature. A catalyst can be either added to the fuel, in which case it is incorporated into the soot as it forms, or positioned in the filter, by impregnating a washcoat. In experimental studies, catalysts are often studied by physically mixing collected soot with catalyst particles. This mix may be in "loose contact" or "tight contact", depending on how it is prepared [39]. Mixing soot and catalyst powders with a spatula is defined by

Neeft as loose contact, while tight contact means that the powders are mixed by a mechanical mill. The tight contact mode makes it possible to study intrinsic kinetics [73], while loose contact is more similar to real conditions, as mass transfer limitations become important. On the other hand, diesel soot may be filtered from an exhaust stream on a bed of catalyst particles; this situation, which seeks to replicate real conditions, is defined as "in situ contact" [1]. Neeft et al. measured catalyst activities in function of the degree of contact (Figure 1.13). It was found that combustion temperatures of samples with loose contact were similar to samples with in situ contact; it was therefore concluded that the contact that arises during practical conditions is similar to loose contact. Furthermore, it was also concluded that the type of contact controls what reaction mechanism (redox or spillover) predominates.

Copper as a fuel additive has been found to be very efficient as a catalyst [39] but is environmentally unacceptable. Iron is also effective, but cerium seems to be the preferred fuel additive. Metal chlorides were investigated in a physical catalyst-soot mix and Cu found to be superior to Mn and Co. The effect of metal oxides was also investigated and PbO found to be the most active, followed by CuO and MnO_2 [39]. Thus Cu, Fe and Co are more active than Ni and Zn. Other metal oxides that were found to have a catalytic effect are Co_3O_4, V_2O_5, Fe_2O_3, La_2O_3 and NiO [39]. Cr_2O_3, MoO_3 and AgO were still effective, but at a reduced level. It has been shown that graphite oxidation is promoted by carbonates, oxides and hydroxides of the alkali metals. Metals can be promoted by the addition of a promoter such as the alkali metals or chlorides [39].

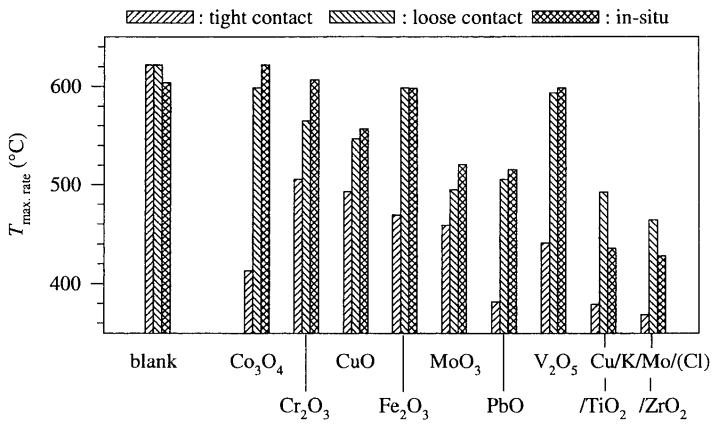

Figure 1.13: Comparison between the temperatures at which the maximum rate of soot oxidation is achieved for different catalyst powders [1]

A survey of the literature shows that ceria (CeO_2) and other cerium compounds are the preferred catalysts. 70% of reviewed publications (mainly from 2006 - 2009) concern Ce-based catalysts, followed by 40% for Pt. Relatively few articles refer to Fe_2O_3 catalyst and alkali (K, Ba) promoters, however it was found that good catalysts have high selectivity towards CO_2.

In a catalysed DPF, the surface reaction mechanism becomes more complicated than in an uncatalysed filter. In addition to the carbon surface, the catalyst surface must also be considered. Furthermore, the nitrogen oxides take on a a more important role in catalysed carbon oxidation. The catalysed reaction mechanism therefore involves many more gas phase and surface species and reactions. Literature generally considers two types of surface mechanism involving catalysts: the Mars-van Krevelen redox mechanism (electron exchange mechanism) and the oxygen spillover mechanism (oxygen exchange mechanism).

The Mars-van Krevelen mechanism is followed by those metallic oxides capable of oscillating between two valence states. The carbon atoms in contact with the metal oxide catalyst take either one or two O atoms from the oxide, Reactions (1.11), (1.12). Consequently, the catalyst is reduced and is then oxidised again. Basically, the catalyst acts as a renewable oxygen donor.

$$* C + 2\ (-MO) \rightarrow CO_2 + 2\ (-M-) \tag{1.11}$$

$$*C + (-MO) \rightarrow CO + (-M-) \tag{1.12}$$

$$2\ (-M-) + O_2 \rightarrow 2\ (-MO) \tag{1.13}$$

Backreedy [74] proposed a redox type model in 2002, using FeO as a catalyst. In its reduced state, the metallic oxide becomes -Fe. In 2007 Moulijn confirmed the mechanism by proving the participation of lattice oxygen from the metal oxide [75]. Recently Issa et al. used this type of mechanism in two successive articles [76, 77] to build a model of carbon black (CB) oxidation using ceria as a catalyst. Thus carbon is oxidised by the catalyst under its oxidised form (1.14). Reduced metallic sites are subsequently reoxidised with oxygen (1.15). Kinetic parameters for this mechanism are provided assuming an Arrhenius dependency on temperature and direct proportionality to contact area A_i and catalyst/CB ratio τ ($r = k(T)A_i\tau \cdot m^1_{oxidant}$). Order with respect to carbon is assumed to be equal to unity. Activation energies determined in the two papers are, respectively, E_a=124 kJ/mol, obtained from isothermal experiments and E_a=134 kJ/mol.

$$* C + 2\ CeO_2 \rightarrow CO_2 + 2\ Ce_2O_3 \tag{1.14}$$

$$2\ Ce_2O_3 + 0.5\ O_2 \rightarrow 2\ CeO_2 \tag{1.15}$$

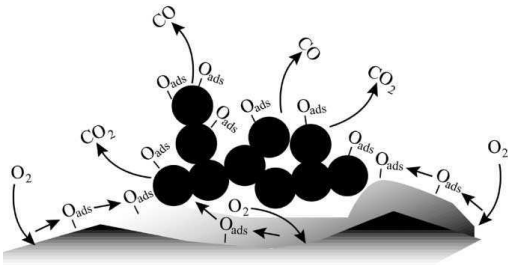

Figure 1.14: Spillover mechanism on a catalyst surface [1]

The oxygen spillover mechanism is illustrated in Figure 1.14. It applies to certain catalysts which have the ability to catalyse the formation of a mobile compound that is more reactive than O_2. For example, O_2 is dissociated into O atoms, Equation (1.16), which are transferred to the soot particle, Equation (1.17). (O*) indicates an adsorbed oxygen atom able to migrate on the catalyst surface. This mechanism enables the reaction to go ahead without there being actual contact between the catalyst and the carbon material [1]. Spillover rates can not be measured directly, it is usually necessary to interpret data enclosing a number of sequential steps (via isotopic TAP studies [78]) or a single step contributing to the spillover rate, such as surface diffusion [79].

$$O_2(g) + 2 * \rightarrow 2\ (O*) \tag{1.16}$$

$$(O*) \xrightarrow{\text{migration on catalyst}} (O*) \tag{1.17}$$

$$(O*) + *C \rightarrow *C(O)... \rightarrow CO, CO_2 \tag{1.18}$$

Bianchi et. al [43] propose a mechanism for the catalytic oxidation of soot, using a commercial fuel additive. This additive contains cerium sulphate ($Ce_xO_yS_z$) particles, which act as an oxygen reservoir for combustion of SOCs. $Ce_xO_yS_z$ decomposes and resulting O atoms diffuse to the soot surface, Eq. (1.19), according to the spillover mechanism. Equation (1.20) is the oxidation of SOCs on the soot surface and Equations (1.21) and (1.22) the desorption of these SOCs. Oxygen atoms on the soot surface are denoted by O_s, while C_f and CC_f are active carbon sites. C_n are bulk carbon sites. C_{n-1} indicates that a bulk carbon was transformed into a surface site. $CC_f(O)$ are stable SOCs, while $C(O)C_f(O)$ are unstable.

$$Ce_xO_yS_z \rightarrow O_s + Ce_xO_{y-1}S_z \tag{1.19}$$

$$C_nCC_fO \rightarrow CO_2 + C_{n-1}CC_f \tag{1.20}$$

$$C_nCC_fO \rightarrow CO + C_{n-1}CC_f \tag{1.21}$$

$$C_nC(O)C_f(O) \rightarrow CO_2 + C_{n-1}CC_f \tag{1.22}$$

Kinetic parameters of the three elementary steps are obtained from temperature programmed desorption (TPD) experiments, where the order of the decomposition reaction is assumed to be equal to 1 (equation 1.23). Note that O_a indicate oxygen atoms on the catalyst surface before they migrate to the soot surface. The pre-exponential factors of Equations (1.23) and (1.24) are considered equal to the theoretical value $\sim 10^{-13}$ s^{-1}. This value has been recommended by several authors. Activation energies are determined to be: $E_{d,a}$=230+70(1-θ_{SOC}) kJ/mol, E_{O_s} <230, kJ/mol, E_{C_fO}=260, kJ/mol. Calculations [43] show that the diffusion of O atoms is quick enough not to have any significant impact on the experimental results. It is also observed that the $Ce_xO_yS_z$ decomposition, rather than the subsequent oxidation of SOCs, controls CO_2 formation.

$$-\frac{d[O_a]}{dt} = k_{d,a}[O_a] \tag{1.23}$$

$$\frac{d[O_s]}{dt} = k_{d,a}[O_a] - k_O[O_s][C_fO] \tag{1.24}$$

$$\frac{d[C_fO]}{dt} = k_{d,SOC}[C_fO] + k_O[O_s][C_fO] \tag{1.25}$$

Jeguirim [80] uses a spillover mechanism to describe the action of oxygen in the oxidation of CB with a commercial Pt/Al_2O_3 catalyst. Dolcetti et al. [81] test the effect of various alkali metals as promoters for Ce based catalysts. Potassium is found to be the most effective. Promotional effect is observed between a minimum and a maximum amount, beyond which activity is decreased [81, 73]. The authors put forward two hypothetical mechanisms of the promoting action of K: firstly, a redox cycle interacting with the catalyst's redox cycle, and, secondly, an oxygen exchange mechanism. This latter hypothesis is deemed more likely [81]. Indeed, a similar mechanism is proposed by Gross et al. [73]

Catalysed Oxidation by Nitrogen Oxides

Investigations on the catalytic reaction between soot and NO_x have focused on single or mixed metal oxides, perovskite-type and spinel-type oxides and noble metal-based

catalysts (especially Pt) [30]. Again, it seems that catalysts composed of cerium oxide and Pt-based catalysts are the most active. Most studies suggest that catalysts promote soot oxidation indirectly because the attack of NO on carbon proceeds via NO_2, so that catalysts that facilitate the oxidation of NO to NO_2 are effective. Similarly, for Ce-Zr mixed oxides, a linear relationship between temperature of maximum NO_2 production and temperature of 50% soot conversion has been obtained [82]. This result suggests that the oxidation rate of carbon by NO_2 cannot be increased by the addition of a catalyst [30]. However, this hypothesis has not been verified.

The already-mentioned indirect promotion of soot oxidation is a principal commonly used by continuously regenerating trap (CRT) technology, where NO formed in the engine is first oxidised to NO_2 by the remaining oxygen over a catalyst in a flow-through configuration. NO_2 is then able to oxidise the soot deposited on a downstream DPF, to produce CO_2 at typical exhaust temperatures for diesel engines. This option requires low sulphur fuel to prevent poisoning of the NO oxidation catalyst.

Ceria-based materials oxidise NO to NO_2 efficiently, even under loose contact [82]. For ceria, the maximum of NO oxidation to NO_2 is observed around 450 °C, above which conversion is limited by the thermodynamics [82]. Thermal stability of the catalyst is an important requirement, considering that the temperature in a DPF may attain 1100 °C and gradients as much as 100 °C/cm [82]. Stability of pure CeO_2 is improved by Zr^{4+} doping, and Ce-Zr mixed oxides calcined at 1000 °C also present enhanced catalytic activity and selectivity towards CO_2 [82], the improvement being most significant for $Ce_{0.76}Zr_{0.24}O_2$. The main surface species present after adsorption (in the 30-350 °C range) of both NO_x and NO_x/O_2, are nitrites and nitrates in chelated or bridged configurations [82]. Because of its desirable properties, this particular catalyst composition has been chosen for use in experiments and for investigation in this PhD thesis. While Atribak et al. [82] have characterised the intermediate species and put forward reactions involved in this catalyst's activity, no studies concerning detailed mechanisms and elementary parameters have been found.

1.4.3 Experimental Approaches for Kinetic Studies

The classical approach for studying chemical kinetics is to perform steady-state kinetic measurements while changing the experimental settings of temperature, pressure, concentration, composition, space, time etc one by one, until the whole experimental space has been covered [62] and then adjust the parameters of a kinetic model to fit experimental data. In particular, the oxidation of carbon particles may be observed in isothermal oxidation (IO) experiments, where the temperature of the carbon particles is kept constant. It is, however, also possible to use unsteady-state techniques, where the temporal response of the reaction system is followed upon an imposed change in a reaction variable (temperature, flow, concentration, labelled components). For e.g., carbon particles can be oxidised in temperature-programmed experiments (TPO). Such **transient kinetic studies** can cover a whole range of operating conditions in only a few experiments and much less time is needed. It is expected that this may result in more reliable extrapolation of kinetic models beyond the range of applied experimental conditions [62]. This type of experimental study also offers phenomenological insight into reaction pathways. Transient techniques, also known as stimulus-response techniques, are characterized by imposing a change in state variable (e.g. temperature) on a reacting system and following the temporal response of this system [62]. Thus three main elements are considered, a stimulus, a reaction system and a system of analysis to follow time dependent system response. Typical stimuli are step functions, pulses and time dependent functions. The step function marks the start of a reaction after the injection of reactant, a rapid temperature or pressure increase, or a change in flow rate. Time dependent functions comprise linear or periodically programmed changes of the independent variable, temperature, for e.g.

Although the stimulus-response transient operation, it can be applied under unsteady state as well as steady state operation of the reaction system [62]. Steady state operation occurs when the reacting system is not disturbed by the stimulus and transient operation when the operational variables change in time. An appropriate reaction system should be chosen based on whether the studied reactions are slow or fast, endo or exhothermic and on the likelihood of significant transport limitations that could interfere with the determination of kinetic rate data [63]. If transport limitations

are present, their effect may be taken into account by appropriate reactor modelling. The choice may also be influenced by other phenomena causing non ideality, such as axial dispersion in a tubular reactor and inadequate macromixing [63]. There are several techniques used to generate conditions where transport is not limiting. The most common of these is the use of inert particles mixed with the reactive particles, to artificially increase the active reactor bulk volume. This dilutes any heat effects and, by dilution with fine particles, axial dispersion can be limited. To avoid intra particle limitations, the only option is to operate with a smaller particle size. The goal of a kinetic study is to use a simple reactor for the experiments, so that only simple models are required [63] and the extraction of accurate parameters facilitated.

Depending on the rate of change of the variable that is used to detect the response of the reaction system upon the stimulus, a suitable analysis technique should be chosen. Two main techniques are in use for investigating the oxidation reactions of carbon particles: Flow techniques and thermogravimetric analysis (TGA) [83]. Other techniques for analysing the response of the reaction system include heat-based measurements such as isothermal and adiabatic calorimeters, differential thermal analysis (DTA), basket heating, crossing-point temperature (CPT) and Chen's method [62]. Various physical and chemical analytical techniques have been applied to identify and quantify surface oxygenated complexes. These techniques include physical and chemical titration, infrared spectroscopy (IR), Fourier transform infrared spectroscopy (FTIR), X-ray photoelectron spectroscopy (XPS), secondary ion mass spectrometry (SIMS) and nuclear magnetic resonance (CNMR) [62]. TGA determines the change in mass of a solid sample caused by the loss of volatile products as some function of temperature is applied to the sample. The mass is measured using a microbalance which is capable of determining a mass loss of 10^{-6} grams [83]. Thermogravimetric analysis (TGA) allows a nearly direct measurement of reaction parameters, without the added uncertainty of parameter extraction through transport models [38]. In **TPO experiments with flow reactors**, a temperature ramp is applied to the sample, and concentrations of gaseous species observed. From these, rate of production may be derived in function of temperature, and subsequently kinetic parameters extracted. In steady-state operation, a constant temperature is applied (IO) and in order to obtain kinetic parameters valid for a range of temperatures, they have to

be fitted with data from several IO experiments. However, interpretation of the TGA information presents a number of practical difficulties for determining the true chemical kinetic parameters[4]. Indeed, the literature survey shows that the most commonly used reactor for investigating the oxidation reactions of carbon particles is a fixed bed flow reactor. The minimum regeneration temperature for passive filters is around 275-300 °C [19]. Typical diesel exhaust temperatures are often lower than that. Most TPO data in recent studies concerns temperatures around 473-973 K, while IO data pertains mainly to 573-743 K. TGA data on the other hand also refers to higher temperatures, up to 1873 K, which is not surprising as it is a technique that is relatively free from transport limitations.

[4]changes in the sample mass reflect formation of both gaseous and solid products, the magnitude of mass change may be close to the instrumental sensitivity, desorption of inherent moisture may significantly affect the experimental data [62]

Chapter 2

Experimental Methodology

Abstract

La cinétique pour des systèmes complexes comme le FaP est généralement analysée dans des réacteurs simples où elle peut être étudiée indépendamment de l'écoulement et des transferts thermiques. Dans cette étude, on utilise des expériences en température programmée dans un réacteur à lit fixe. Ce chapitre décrit la technique expérimentale et le système réactif utilisé.

⋆

Kinetics for a complex system such as a DPF are generally determined experimentally in simple laboratory reactors, in an effort to study them independently of flow issues, thermal issues, etc. In this study, the experiments used for determination of kinetic parameters are temperature programmed desorption or oxidation experiments performed in a fixed bed reactor. This chapter describes the experimental techniques, as well as the materials used.

2.1 Materials

The ceria-zirconia ($Ce_{0.73}Zr_{0.27}O_2$, Rhodia) supported platinum (0.45 wt.% Pt) catalyst was prepared by the incipient wetness method with an aqueous solution containing the appropriate amount of the platinum precursor $H_{12}N_6O_6Pt$. After impregnation, the catalyst was left at room temperature for approximately 1 hr, and then dried at 100 °C for ca. 12 h. It was then calcined for 3h at 500 °C, in air. Brunauer-Emmett-Teller (BET) surface area was found to be 105 m^2/g. N_2 adsorption at 77 K also allowed for pore characterization of the materials. The mean pore radius was 11.6 nm.

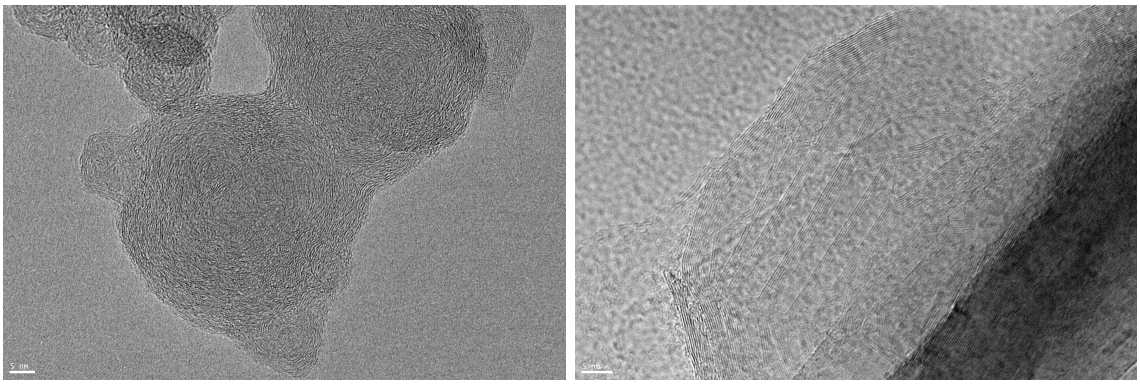

(a) Diesel soot **(b)** Graphite

Figure 2.1: TEM images of two carbon materials.

Diesel engine soot was supplied by IFP Solaize [84]. It was generated by a multi-cylinder common rail diesel engine (DW10) from PSA, using conventional diesel fuel at operating conditions typical of the ECE urban driving cycle (1500 rev/min, 5 bar). Further details concerning the generation and collection of the soot are given in [84]. Engine specifications as well as properties of the diesel fuel are given in Table 2.1. Elementary composition of the soot was determined by particle-induced X-ray emission (PIXE): 86.30% C, 8.78% O, 1.07% H, 0.14% N; and primary particle size of the soot was deduced to be 21 nm from transmission electron microscopy (TEM) images. Examples of such images are shown for both materials in Figure 2.1, and allow for

the observation of the much more ordered graphitic structure in graphite, compared to soot. Graphite (<44 μ) was provided by Alfa Aesar. Brunauer-Emmett-Teller (BET) surface area was found to be 414 m^2/g for soot and 4 m^2/g for graphite. For soot and graphite, the smallest significant pore radii were 1.5 nm and 1.2 nm respectively; and the majority were located between 10 - 13 nm and 10 - 11.5 nm, respectively.

Engine	
Engine code	PSA DW10 BTED4 Euro 4
Displacement	1998 cm^3
Fuel injection	common rail direct injection
EGR	none
Max. rated power	100 kW at 4000 min^{-1}
Max. rated torque	320 Nm at 1750 min^{-1}
Compression ratio	18
Fuel	
Cetane number	50.7
Lower heating value	41.72 MJ/kg
Aromatic content	22 wt. %

Table 2.1: Engine specifications and diesel fuel properties

2.2 Reactivity Experiments

The reactivity tests performed in this study are TPEs with samples of diesel soot, graphite and/or $Pt/Ce_{0.73}Zr_{0.27}O_2$ and different mixtures of O_2 and NO diluted in Ar. For parameter estimation, a number of experiments from the literature are also simulated, notably those with NO_2, carbon materials other than soot and graphite and catalysts other than $Pt/Ce_{0.73}Zr_{0.27}O_2$. After being weighed (soot and graphite sample mass was ca. 5 mg and catalyst mass 25 mg, unless mentioned otherwise), the sample in question was placed in the U-shaped quartz reactor (i.d. = 8 mm) shown in Figure 2.2 by means of a funnel, forming a fixed bed of a depth of approximately 2 mm, on a porous frit.

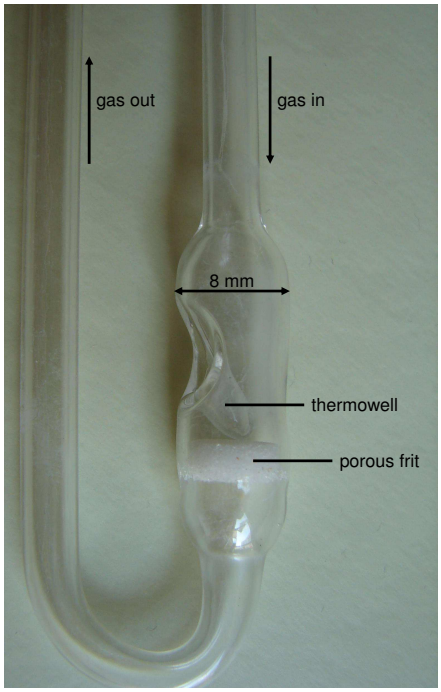

Figure 2.2: Quartz reactor

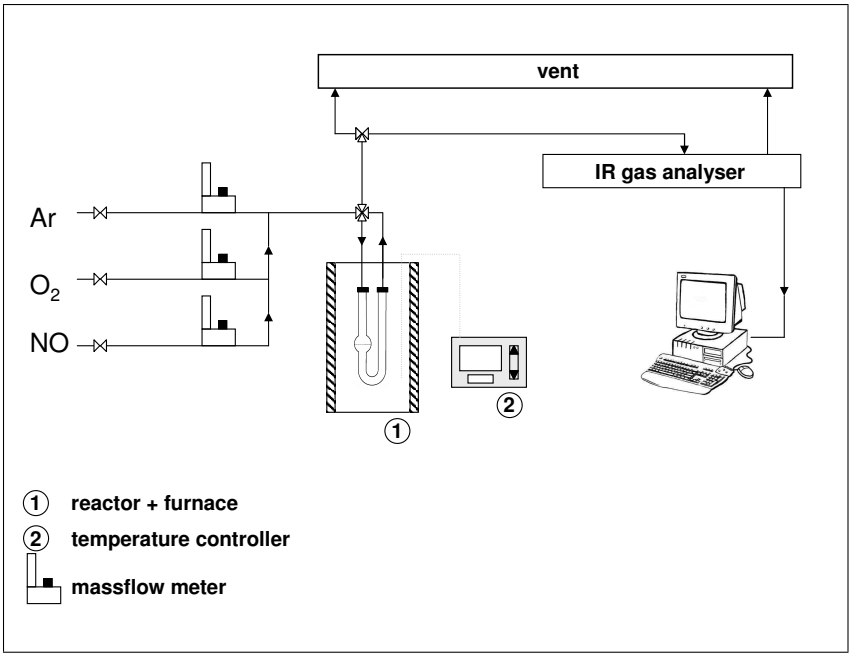

Figure 2.3: Setup for the reactor studies

Total flow rate through the reactor was 250 ml/min (STP). The reactive mix during TPOs contained 200 ppm NO and/or 10% O_2 diluted in argon, all supplied by Air Liquide. The reactor was placed inside a thermally isolated furnace (see Figure 2.3 for the setup) and flushed with Ar at room temperature for approximately 12 min. Some air was flushed out of the reactor and small amounts of hydrocarbons were in some cases observed during the purge, especially for soot samples. Once these signals had subsided, the reactor feed was closed while concentration signals in the reactive gas mixture stabilized. Then the reactor feed was switched to the flow of reactive gas. Sample temperature was monitored by a K-type thermocouple located in a thermowell centred in the particle bed and gas mixtures were produced using calibrated Brooks 5850TR mass flow controllers. The CO, CO_2 and N_2O analyzer (Siemens Ultramat 6) functions according to the infrared adsorption principle. NO and NO_2 mole fractions were measured by chemiluminescence. Mass spectroscopy signals for 40, 44, 46, 32, 30 and 28 were also recorded. It was chosen not to dilute the particle bed with an inert such as SiC, as no significant deviation of the measured temperature from the imposed temperature program was observed due to the shallow particle bed.

For soot+catalyst experiments, soot and catalyst samples were mixed by shaking in a closed container (loose contact) before being placed in the reactor. In one case only were the two components ground together in a mortar in order to obtain tight contact.

In order to avoid annealing the carbons, as well as unwanted reaction with ceria, all experiments used for fitting were performed without first desorbing existent adsorbed species from the soot/graphite or any other thermal pre-treatment. One comparison was however made of the TPO of soot under 10% O_2 with the same experiment performed on a sample which had first been subjected to a temperature ramp of 10 °C/min under a flow of Ar. Overall, the effect of the pre-treatment on a TPO with O_2 is to increase peak global reaction rate by $(x_{CO_x,treated} - x_{CO_x})/x_{CO_x}$=18% and similarly between 550 and 650 °C. It is interesting to note that the effect of the thermal pre-treatment on CO_2 is relatively small, while the production of CO increases more significantly. The amounts of CO_x produced during pre-treatment are similar to those observed by Tighe et al. [85].

Chapter 3

Detailed Kinetic Modelling of DPF Chemistry

Abstract

La détermination des paramètres cinétiques à partir des expériences en température programmée (Chapitre 2) nécessite un modèle de réacteur. De plus, puisqu'il s'agit de réactions hétérogènes gaz-solide, il est nécessaire de spécifier aussi un modèle de la surface réactive (suies ou catalyseur). Dans cette étude, la chimie de surface est décrite par l'approximation du champ moyen. Cela signifie que les hétérogénéités de la surface réactive ne sont pas décrites explicitement, mais uniquement par des paramètres cinétiques moyens, appliqués à touts les sites actifs. Cette approche permet de mieux connaître la physique de la surface, car le schéma microcinétique ou detaillé peut impliquer de nombreuses étapes et espèces intermédiaires, élémentaires ou non (regroupant plusieurs espèces). Dans ce chapitre, on introduit les modèles de réacteur à lit fixe et de surface réactive, ainsi que la méthodologie employéé pour l'estimation des paramètres par comparaison avec les profils expérimentaux.

⋆

Estimation of kinetic parameters from temperature programmed experiments such

as those described in Chapter 2 requires a reactor model. Moreover, since the study is concerned with heterogeneous gas-solid reactions, a model of the soot or catalyst surface is also necessary. Here, surface chemistry is described by the mean field approach, where heterogeneous features of the reactive surface are not explicitly taken into account, but only via average mechanistic parameters applied to all active sites. More physical insight is however gained than in global kinetics, because the relatively detailed reaction mechanisms contains numerous steps and intermediate surface species. Microkinetic or detailed schemes in this study are intended as those with numerous elementary or lumped steps and species. The reactor model which describes the fixed bed as a CSTR and the surface model are both described in this chapter, as well as the methodology used for fitting model calculations to experimental data.

3.1 Method for Extraction of Quantitative Kinetics

The purpose of the model described in this section is to characterize the main reactivity trends of soot and various Pt and Ce-based catalysts with mixtures of NO, NO_2 and O_2. Since the aim is to reproduce not only global reaction rate, but also the principal reaction products, the traditional steady-state method used for determining global reaction parameters cannot be employed here. Multiple reactions are required, each of which is described by a rate equation. We therefore have to evaluate a large number of kinetic parameters, i.e., the pre-exponential factors and activation energies of the reaction steps in Tables 3.1 and 3.2. Parameters are then determined by fitting calculated species profiles to experimental data. The method adopted here relies on the following points: 1) Dynamic, temperature programmed experiments, 2) numerous parameters require several species profiles, 3) reproduction of principal trends with simplest possible mechanism, 4) manual (no use of an optimization program, but rather by visual inspection), piece-wise fitting.

Extrapolation of kinetics from temperature-programmed (TP) techniques necessi-

tates a description of the extrinsic dynamics of the experimental setup, i.e., a reactor model, which is described in the following section. Using TPEs to fit kinetic parameters ensures validity over a large range of temperatures and the resulting mechanism is more likely to be robust to other changes of operating conditions, such as reactant concentrations [62].

The parameters which have to be determined are numerous, and in order to evaluate them in a physically meaningful manner, the constraints also have to be numerous [86, 87]. Thus, as an example in the 13 steps of the mechanism concerning soot alone (see Chapter 4, Table 3.1), there are 26 parameters to be determined and 25=5×5 experimental gas species profiles to be respected in 5 separate experiments. Very few measurements of surface species concentrations during the course of soot oxidation are available in the experimental literature. However, especially for an NO_2 gas feed, surface species present at certain temperatures have been identified and can be compared with the calculated surface concentrations to ascertain whether surface behaviour of the model is reasonable.

Since the parameters of a detailed mechanism are inter-dependent, they cannot be determined separately. By fitting calculated concentrations manually however, we may separate "blocks "of reactions, each deemed important for a particular gas feed, and fit them in a piece-wise manner. In other words, these subsets of the mechanism were each tested and validated against experiments with simple reactive gas flows, such as O_2 or NO + O_2 alone. The different "blocks" of reaction steps are then assembled and re-adjusted for the final fit, so as to be compatible with all other gas feeds. This procedure was followed in a number of cases in Chapters 4 and 5. For instance, the parameters of steps R1, R2 and R3 were evaluated using soot-O_2 experiments [88]. Then parameters of R4b R6f, R7, R9f and R10 were determined in a preliminary manner by fitting with soot-NO_2 adsorption, temperature programmed desorption (TPD) and isothermal oxidation (IO) experiments from literature [89, 85]. Similarly, R4f, R5f and R8 were determined from a fit with the soot-NO experiment [90], using those previously found for the NO_2-block. The latter were then slightly re-adjusted, so as to be compatible with both NO_2 and NO experiments. In a similar way, the parameters for R6b and R9b were determined from a fit with the soot-

$NO+O_2$ experiment. In addition to separating into reaction subsets, steps within a given "block "can in some instances be held to be principally responsible for certain species profiles. For instance, R8 is solely important for N_2 formation and does not affect any of the other steps. All simulated results shown here were determined with the same set of final kinetic parameters.

In a similar manner, the catalyst-gas related parameters in Chapter 5 were estimated following a piece-wise approach in the construction of the model. The different "blocks" thus obtained were then assembled and validated with data from the composite system. In particular, R1-R2 in Table 3.2 were calibrated alone using data from reaction of cerium oxides with O_2. Similarly, R3-R8 were calibrated using experiments performed with cerium oxides under an atmosphere of NO + O_2, while leaving the parameters of R1-R2 unchanged. In the same way, Pt + O_2 and Pt + O_2 + NO experiments were used to determine the parameters of R9-R10 and R11-R16, respectively. Both TPD and oxidation experiments were used for calibration. The model is therefore able to reproduce catalyst adsorption and desorption behaviour as well as the NO oxidation by O_2. Again, although the number of fitted parameters is large, the model is also required to be compatible with a number of species concentrations (O_2, NO and NO_2) and experimental conditions (TPO, TPD, Pt only, CeO_2 only, differing composition of reactive flow). It was assumed that constants calibrated against Pt/Al_2O_3 could be used to simulate either Pt alone or Pt/Al_2O_3 within more complex catalytic systems, thus effectively neglecting the impact of the alumina support on the oxidative activity of the catalyst.

A subsequent rate-of-production (ROP) analysis allows us to identify the role of the various reactants and intermediate species, and a sensitivity analysis identifies dominant reaction steps and allows us to judge the integrity of the calibrated mechanism. Normalized sensitivity coefficients are calculated as $s_{j,i} = \frac{A_i}{C_j}\frac{\partial C_j}{\partial A_i}$, where C_j is the jth gas species or remaining sample mass and A_i is the pre-exponential factor of the ith step.

A major premise of this kind of piece-wise parameter estimation is that the different "blocks" may be merged to model the composite system. It is part of the scope of

this study to investigate up to what point this assumption is useful.

3.2 Reactor Model

Because of the complex nature of chemical kinetics, fast models are needed in order to study reaction kinetics. 3D models, while exact in flow patterns, are too slow to allow for calibration of kinetic models [28]. For this reason, a simple laboratory system that may be modelled by a 0D description is used for estimation of kinetic parameters. The most commonly used setup for such studies is the fixed-bed reactor in which a flow of gas passes trough a stationary layer of catalyst or soot particles. Two main ways of operating such a system are in use: Temperature of the reactant gas flow may be changed in some programmed way, usually as a linear ramp, in this case one speaks of a temperature programmed experiment/oxidation (TPE/TPO). The sample may be kept at constant temperature, in this case the oxidation experiment is called isothermal (IO). Over and above the derivation of global kinetic parameters, the TPO technique has a phenomenological interest, as it demonstrates at what temperatures intermediate species are produced and therefore kinetic parameters specific to semiglobal and elementary reactions may be extracted. To extract global kinetic information, IO experiments may also be used. Here the sample is heated to the desired temperature under an inert gas. Then the reactive mixture is introduced and provokes reaction.

Fixed bed reactors (e.g. (Figure 3.1, left) are traditionally described by an ideal plug-flow reactor (PFR) model in which balance equations are written for an infinitesimal slice of reactor, of width dz (Figure 3.1). This model assumes homogeneous mixing in all directions (radial and axial) within the slice, and no interaction between slices. On the scale of the whole reactor, homogeneous mixing is assumed within each slice, but not along the axial direction. Variable dependency on the spatial coordinate z is thus described by integrating for all slices over dz. It can be shown that a large number of ideal continuously stirred reactor (CSTR) reactor models in series approximate the PFR reactor model. This multi-0D approach presents a good compromise between CPU performance and physical accuracy and is employed in the present

study. In order to assess the validity of the assumption of a single differential reactor (homogeneous approximation), the axial Peclet number is calculated as follows [64, 91]:

$$Pe = \frac{ud_p}{D_a} \tag{3.1}$$

where $u = v/\varepsilon$ is the interstitial velocity, assumed constant and d_p the equivalent particle diameter [91]. This expression for Pe is based on the dispersion model in which a non-ideal PFR with much variation between adjacent slices is described by in addition to convective bulk flow, a dispersion of material in the axial direction is present [64]. This axial dispersion is expressed analogy to Fick's law of diffusion, so that every component in the mixture is transported through any cross-section of the reactor at a rate equal to $-D_a A_C \frac{dY}{dz}$, where D_a is the (longitudinal) dispersion coefficient, which may be estimated according to the particular reactor geometry and A_c the reactor's cross-sectional area. Axial dispersion is not representative of any single physical phenomenon such as molecular diffusion, but regroups all the phenomena that contribute to the system's deviation from the convective-transport-only ideal reactor model. These may include, for e.g., molecular diffusion and turbulent diffusion due to turbulent eddies.

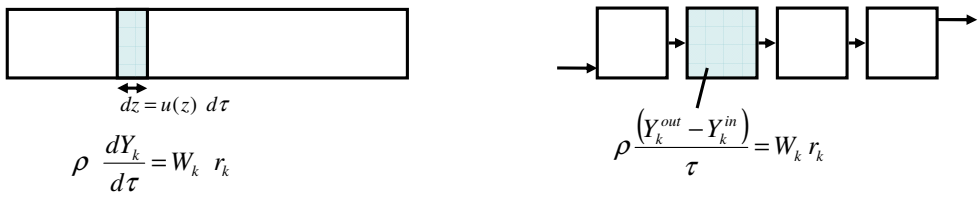

Figure 3.1: Left: A PFR in stationary conditions; Right: A series of CSTRs

Pe is used to calculate the residence time distribution (RTD) of a dispersive PFR. By comparing this value to the RTD of N CSTRs in series, the number N of 0D CSTRs needed to capture the non-ideal phenomena of the fixed-bed reactor may be determined. Since the bed of carbon/catalyst particles is very thin (often $< 1mm$), it is found that it can indeed be modelled by a single CSTR, Figure 3.1.

The reactor model describing the flow through a fixed bed was coded in C and the solver of the IFP-Exhaust library of the AMESim (LMS.IMAGINE.Lab) environment was used via the graphical interface shown in Appendix B. The modelling approach of this software is based on bond-graph theory, according to which any physical system can be represented by a resistive or capacitive element in an electrical analogy [92]. In this environment, each 0D reactor is composed of capacitive and resistive elements. Capacitive elements are similar to an open volume where pressure and temperature are deducted from mass and energy balances, whereas resistive elements are used to compute mass and enthalpy flow rates using the Darcy pressure drop law for flow in porous media, as is in Equation 3.3. The mass balance equation for a gaseous species i in a capacitive element is hence:

$$\frac{dm_i}{dt} = \dot{m}_i^{in} - \dot{m}_i^{out} + \omega_i \quad [kg/s] \tag{3.2}$$

where $\dot{m}_i$ are the mass flow rates in/out of the capacitive element and ω_i is the chemical source term for species i. Section 4.7 explains how this term is calculated. In the low Reynolds number (laminar flow) regime, flow through a porous matrix is governed by a linear Darcy's law [64], [93], [94], [95], which links the fluid flux in terms of the superficial (or apparent) velocity, v, with the applied pressure gradient ΔP by the linear relation

$$\frac{\Delta P}{L} = \frac{\mu}{k} \cdot v \tag{3.3}$$

where L is the width of the particulate layer, μ is the dynamic viscosity of the fluid and k is a proportionality constant known as permeability [96]. To a large extent, the proper description of the fluid flow through a porous medium depends on precise relations between the physical properties involved, such as permeability and porosity. Kozeny developed a simple capillary model for a porous medium and derived such a relation. This was generalised by Carman, to account for the fact that the streamlines in a porous medium are not straight and parallel to each other, an effect described by the hydraulic tortuosity, $\tau = \frac{\langle L_e \rangle}{L}$, where L_e is the average length of the actual path taken by the fluid. Kozeny's model assumes that actual velocity in the pores

(interstitial velocity) follows Poiseuille's Law for laminar flow:

$$u_T = \frac{D_e^2 \Delta P}{32 \mu L_e} \tag{3.4}$$

where the hydraulic diameter D_e is $D_e = \frac{4\varepsilon}{S(1-\varepsilon)}$ and $S_g = \frac{S_{grain}}{V_{bed}}$. The interstitial velocity is given by

$$u_T = v \frac{S}{S_T} = v \frac{L_e}{\varepsilon L} \tag{3.5}$$

where S is the cross-sectional area of the bed of porous material and L its height. From the above equations and considering the mean particle diameter $D_p = 6/S_g$, the following semi-empirical relation can be derived:

$$k_{KC} = \frac{\varepsilon^3}{(1-\varepsilon)^2 S_g \frac{1}{\kappa}} = \frac{D_p^2 \, \varepsilon^3}{150(1-\varepsilon)^2} \tag{3.6}$$

κ being a fitting parameter, which includes the effect of the non-measurable parameter L_e. Substituting in Darcy's law, one obtains Kozeny's law[1]:

$$\frac{\Delta P}{L} = \frac{150(1-\varepsilon)^2 \mu}{\varepsilon^3} \cdot v \tag{3.7}$$

Elongation of streamlines not only affects the flow rate, but also other types of transport phenomena in the porous medium. This has resulted in several theoretical attempts to define the tortuosity. There is no clear consensus on the relation between these definitions. Among all these definitions, $\tau = \frac{\langle L_e \rangle}{L}$ is not only the simplest, but also widely adopted in theoretical studies, because it ties tortuosity with the underlying geometry and topology of the porous medium [96].

For non laminar flow regimes, the Forchheimer or Ergun extension is added to Darcy's law [64, 93, 19]:

$$\frac{\Delta P}{L} = \frac{\mu}{k} \cdot v + \frac{\beta}{L} \cdot \rho \cdot v^2 \tag{3.8}$$

[1]Kozeny's law is not universal and does not hold for complicated porous geometries [96]

where β is the inertial resistance or Forchheimer coefficient. It can be shown that $\beta = 1.75$:

$$\frac{\Delta P}{L} = \frac{150(1-\varepsilon)^2\mu}{\varepsilon^3} \cdot v + 1.75 \cdot \rho \cdot v^2 \tag{3.9}$$

The reactor model in this study employs a linear Darcy's law (i.e., the Kozeny law) to describe the flow of reactant gas through the bed of particles. The use of Darcy's law, instead of the extended Ergun version 3.9 is justified by calculating the value of the dimensionless Reynolds number[2] $Re = \frac{d_p u}{\nu}$ and thus verifying that the flow regime is laminar.

The energy balance only takes into account heat transfer between the gas and solid phase by convection. Heat of reaction and radiative and conductive transfer is deemed not to be important for the simulated experiments since T <1000 °C.

3.3 Surface Chemistry Model

From literature, the reactions in Tables 3.1 and 3.2 were proposed as the minimal set necessary to produce CO, CO_2, NO, NO_2 and N_2 with soot and NO, NO_2 and O_2 with the catalysts. These mechanisms are discussed in further detail in the relevant chapters. In Table 3.1, the carbon sample is seen as a single layer of C atoms; for every consumed carbon atom, an unreactive "void site " $*$ is thus created and the amount of active sites C* will thus depend on the extent of conversion. In order to evaluate the corresponding kinetic parameters (Table 4.2, Chapter 4 and Table 5.3, Chapter 5), the molar rate of every reaction is calculated according to the Arrhenius law (Equation 3.10),

$$r_j = A_j \; exp\left(\frac{-E_j}{RT}\right)\left(\prod_{i=1}^{N_g}\nu_{i,j}\; x_i \prod_{k=1}^{N_s}\nu_{i,j}\; \theta_k\right) \quad [mol/m^2/s] \tag{3.10}$$

$$\tag{3.11}$$

[2] d_p=particle diameter, u=particle-to-fluid relative mean velocity and ν=kinematic viscosity

Table 3.1: Surface reaction mechanism for soot with NO_x and O_2

	Reaction	**Ref**
R1	C* + 1/2 O_2 → C*(O)	[97, 38, 98]
R2	C*(O) → CO + *	[89, 99, 97, 38, 98]
R3	C*(O) + 1/2 O_2 → CO_2 + *	[97, 38]
R4f	C* + NO → C*(NO)	[100]
R4b	C*(NO) → C* + NO	[100]
R5f	C*(NO) + C* → C*(N) + C*(O)	
R6f	C*(NO_2) + C* → C*(O) + C*(NO)	[101]
R6b	C*(O) + C*(NO) → C*(NO_2)	[102]
R7	C*(NO_2) + C*(O) → C*(ONO_2) + C*	[101]
R8	2 C*(N) → N_2 + C*	[103, 104, 105]
R9f	C* + NO_2 → C*(NO_2)	[106, 107, 108, 109]
R9b	C*(NO_2) → C* + NO_2	[109]
R10	C*(ONO_2) → CO_2 + NO + *	[89, 109, 101]

where A_j are the pre-exponential factors, E_j the activation energies in kJ/mol, x_i the mole fraction of species i and θ_k the dimensionless coverage of surface species k and N_g and N_s the number of gas and surface species, respectively.

The chemical source terms ω_i for gaseous species i are calculated according to Equation 3.12,

$$\omega_i = S_a M_i \sum_{j=1}^{N} \nu_{i,j} r_j \quad [kg/s] \tag{3.12}$$

where S_a and M_i respectively are the active surface area of the considered catalyst or carbon material and molar mass of the i-th gas-phase species, N is the total number of reactions considered, $\nu_{i,j}$ the corresponding stoichiometric coefficients and r_j the reaction rate of the j-th reaction in mol/m^2/s. Surface coverage of the k-th surface species, θ_k, is described via:

Table 3.2: Surface reaction mechanism of the interaction of NO_x and O_2 with ceria and platinum

Reactions on support
R11 2 Ce + O_2 → 2 Ce-O
R12 2 Ce-O → 2 Ce + O_2
R13 Ce + NO_2 → Ce-NO_2
R14 Ce-NO_2 → Ce + NO_2
R15 Ce-NO_2 → Ce-O + NO
R16 Ce-O + NO → Ce-NO_2
R17 Ce-NO_2 + Ce-O → Ce-NO_3 + Ce
R18 Ce + Ce-NO_3 → Ce-NO_2 + Ce-O
Reactions on platinum
R19 2 Pt + O_2 → 2 Pt-O
R20 2 Pt-O → 2 Pt + O_2
R21 Pt + NO → Pt-NO
R22 Pt-NO → Pt + NO
R23 Pt-NO + Pt-O → Pt-NO_2 + Pt
R24 Pt-NO_2 + Pt → Pt-NO + Pt-O
R25 Pt + NO_2 → Pt-NO_2
R26 Pt-NO_2 → Pt + NO_2

$$\frac{d\theta_k}{dt} = \frac{r_k}{\Gamma} \tag{3.13}$$

in which r_k is the rate of generation or consumption of species k due to adsorption, desorption or chemical reaction and Γ the material-specific site density of the catalyst or carbon material, in mol/m^2. For CeO_2, site density is taken to be 2.7×10^{-5} mol/m^2, whereas for Pt, a value of 1.7×10^{-5} mol/m^2 is used [87]. Site density for carbon materials is taken to be ca. 2×10^{-5} mol/m^2, based on the area occupied by a single carbon atom [100]. Some of the adsorption steps are described with pre-exponential factor and activation energy, like the other steps. In this case no physical significance can be ascribed to the value of activation energy. In the case of other adsorption steps, a sticking coefficient is provided, from which the pre-exponential factor is then calculated as

$$A_{ads} = s_{0,j}\sqrt{\frac{RT}{2\pi M_i}}. \quad [m/s] \tag{3.14}$$

Note that this study does not describe the chemical structure of the system in detail, as the solid phase is represented globally, via an active surface and carbon/catalyst atoms are assumed to exist in a monolayer. The surface area S_a used in calculations is not the measured BET area. Rather, it is determined so as to fulfil the carbon balance performed on the experimental CO_x profiles: S_a = (mol C in CO_x)/Γ, so that it is representative only of the total number of C atoms, and not of their physical arrangement. In the case of catalysts, its value is determined by fitting, with the rule of thumb that $S_a < S_{BET}$, or, if the catalyst is a noble metal, the area can be calculated from the dispersion. Some information on the physical structure is contained in the value of Γ, namely the number of moles of carbon/catalyst per m^2. Note also that the model is based on the mean field approximation, with the assumption that adsorbed species are randomly distributed on the surface, which is viewed as being locally uniform. Site heterogeneity is thus averaged out by mean rate coefficients [110, 111].

3.4 Evolution of Reactive Surface Area

What extent of the TSA is RSA, is essentially a matter of surface chemistry [112] and operating conditions [113]. It is well known that the ratio RSA/TSA varies with temperature, pressure and carbon conversion [112, 114], as RSA is measured by chemisorption at a certain temperature, chosen more or less arbitrarily [69, 114]. Thus, even if measures of RSA were available, one could use them as an input for our model over a limited temperature range only. Li et al. [114] fit a parameter "B" to C+NO oxidation data over a range of temperatures. This parameter acts almost as a "switch" between a low-temperature and a high-temperature kinetic regime. It represents the variation of RSA/TSA with temperature. Our model can reproduce oxidation behaviour over a range of temperatures without recurring to a parameter like B, because it contains a dynamic description of the carbon surface. The word "dynamic" in this study refers to the time- and temperature-dependent behaviour of the complex C*(O). The effect of B in our model is already included in the kinetic parameters k_i [112]. The value of RSA used as input for the model then, is the total area which gave rise to products over the whole course of the reaction and there is no need for a physical measure based on the definition of a random desorption temperature. A physically more meaningful model of surface chemistry might describe the reactivity of the C*(O) complex by using a distribution of activation energies [41], rather than the switch between two regimes used by Li et al.

A comparison of soot and graphite oxidation by NO shows that different reaction products are not affected in the same way by carbon structure. Because of the rate formalism $r_j = k_j \cdot S_a$, including chemical structure factors in S_a would make it impossible to reproduce these diverse effects. All the rates r_j would in fact be affected equally by a change in S_a. see Section 4.7 for further discussion.

3.5 Transport Limitations

Film diffusion limitations are typically not significant in fixed bed reactors at low operating temperatures (< 1000 °C) [115] and a calculation of the gas-solid mass transfer coefficient for O_2 and CO confirms this (fraction of external resistance < 2.5

$\cdot 10^{-3}$). Here, potential mass transfer limitations due to intra-particle (or internal) diffusion are addressed. According to the Thiele approach [116], the effectiveness factor η is calculated. The molecular binary diffusion coefficients D_{bin} of the two components of the flow of gas (reactant O_2 and inert N_2 or Ar) are computed according to the Chapman-Enskog Theory [117],

$$D_{bin} = \frac{3}{16} \frac{\sqrt{2\pi k_B^3 T^3 / M_{i_1,i_2}}}{P \pi \sigma_{i_1,i_2}^2 \Omega^{(1,1)}} \quad [m^2/s] \tag{3.15}$$

where $\Omega^{(1,1)}$ denotes the first collision integral. The values of the Lennard-Jones properties σ_{i_1,i_2} and k_B are computed from the GRI Mech 3.0 transport database. According to the Bosanquet formula, an effective diffusion coefficient is then calculated for each mixture component, to take into account the fact that diffusion is occurring in a porous medium:

$$\frac{1}{D_{eff}} = \frac{\tau}{\varepsilon_{int}} \left(\frac{1}{D_{bin}} + \frac{3}{4r} \sqrt{\frac{\pi M_{i_1,i_2}}{2RT}} \right) \quad [m^2/s] \tag{3.16}$$

where r is the pore radius and the diffusion is adjusted for pore tortuosity τ and particle porosity ε_{int} [118]. The Thiele modulus [64] is then calculated for each reaction step in the mechanism. The effectiveness factor can be calculated as [119]:

$$\eta = \frac{r_{actual}}{r(C_{surf})} = \frac{1}{\Phi \tanh(3\Phi)} - \frac{1}{3\Phi} \tag{3.17}$$

This expression for η assumes that the reaction it describes is of first order with respect to O_2, monodirectional, that it contains a single limiting reactant whose stoichiometric coefficient equals 1 and that the porous particle considered is spherical. It is the ratio of the reaction rate actually observed, r_{actual} to the reaction rate that would be calculated if the surface reactant concentration were to persist throughout the interior of the particle (i.e., no reactant gas concentration gradient within the particle; this would be the case if diffusion were not limiting) [120]. The effective-

ness factor η (Figure 3.2) may assume values between 0 and 1. Its value allows to distinguish whether the system is operating in a regime limited by internal diffusion or by the chemical reaction rate:

- $\Phi < 0.3 \Longrightarrow \eta \rightarrow 1 \Longrightarrow$ chemical reaction limiting
- $\Phi > 3 \Longrightarrow \eta \propto \frac{1}{\Phi} \Longrightarrow$ internal diffusion limiting
- $0.3 < \Phi < 3 \Longrightarrow$ intermediate regime

For all cases simulated during the course of this study, $\Phi \ll 0.3$. This holds even for "extreme" values such as tortuosity = 5-10 and porosity = 0.5, which correspond to a very large diffusion distance. The operating regime can therefore be considered to be kinetic.

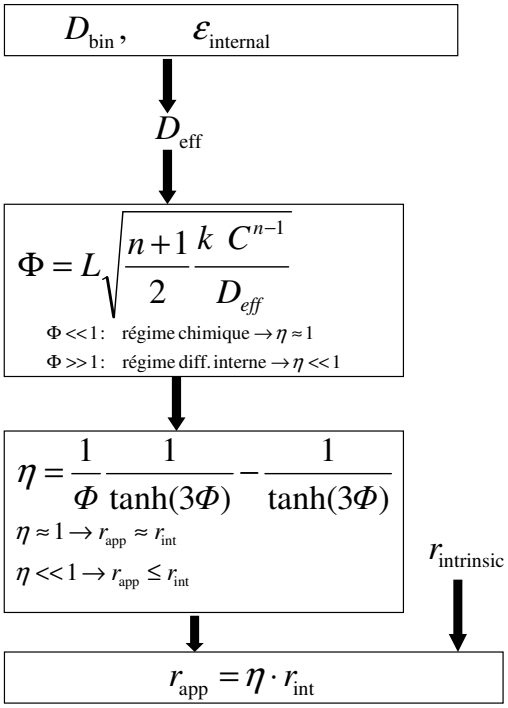

Figure 3.2: Thiele approach for quantifying intra-particle diffusion limitations

Chapter 4

Soot Oxidation by O_2, NO and NO_2

Abstract

Dans ce chapitre, les paramètres cinétiques pour l'oxydation des suies par O_2 et les NO_x sont déterminés en ajustant les profils calculés des produits réactionnels majeurs et de la réactivité globale. Selon le mélange réactif, il est possible d'obtenir N_2 et NO_2 ou CO_2. Cet effet est dû à la concurrence entre deux réactions de surface, les deux consommant l'espèce de surface C(NO). L'adsorption et la conversion globale sont plus efficaces lorsque l'on ajoute de O_2 à NO, puisque la présence d'oxygène moléculaire favourise l'étape concurrente de réaction avec C*(NO). Pour l'oxydation par NO, les étapes d'adsorption et désorption sont cinétiquement déterminantes, les étapes de formation de CO et de CO_2 devenant de plus en plus importantes avec l'accroissement de la concentration en oxygène. Pour l'oxydation par NO_2, l'adsorption et la désorption sont déterminantes au-delà de 600 °C, au-dessous de cette température, l'étape déterminante est plutôt la formation de C*(ONO_2) sur la surface. Une comparaison entre des expériences d'oxydation de suies et du graphite montre qu'une modification de la valeur de la surface BET ne suffit pas à modéliser les tendances observées pour la chimisorption de NO et la formation de CO et CO_2.*

La physique (via le paramètre de structure ψ) et la chimie (via les paramètres cinétiques

k_j) de la surface ont tous les deux un impact sur la réactivité des matériaux carbonés: $r = kS(x,\psi)C_{O2}$, où x représente la conversion. La Section 4.7 vise à décrire l'effet de la chimie de surface (c'est-à-dire de la structure graphitique) sur la réactivité en terme de paramètres cinétiques (k_j) uniquement. Étant donné que l'on ne dispose pas de mesures de la surface RSA, les valeurs de ψ restent sans grande signification physique. L'impact de la graphitisation de la structure carbonée est représenté au travers un parametrage des constantes cinétiques d'oxydation. Des paramètres cinétiques sont estimés pour l'oxydation de nombreux matériaux carbonés ayant des réactivités assez différentes. Ces matériaux sont tous caractérisés par une faible teneur en minéraux et une structure graphitique plus ou moins ordonnée. Des expériences avec les suies Diesel et du graphite ont été réalisées et les données expérimentales concernant un noir de carbone, des suies issues d'un brûleur et du coke ont été traites de la bibliographie. Les paramètres cinétiques des étapes de production de CO_2 et CO sont estimés en fonction du contenu en C du matériel. On constate que les energies d'activation des étapes mentionnées augmentent linéairement en fonction de la teneur en carbone dans le matériau. La valeur des k_j englobe des effets du taux de cristallinité et de la chimie surfacique.

⋆

Kinetic parameters for soot oxidation by O_2 and NO_x are estimated by fitting for product selectivity and global rates. Depending on the gas mixture, the competition of two surface reactions for lumped C*(NO) complexes determines whether N_2 or NO_2 and CO_2 are produced. NO adsorption and soot conversion are much improved when O_2 is added to NO because the presence of oxygen on soot favours the competing step of reaction with C*(NO). For NO, the adsorption/desorption steps are rate determining; the importance of CO and CO_2 formation steps grows with increasing O_2 concentrations. For soot+NO_2, adsorption/desorption of NO_2 controls the rate above 600 °C, below this temperature, it is the surface formation of C*(ONO_2). Experiments with soot and graphite show that differences in BET area are not sufficient to model tendencies in NO chemisorption and CO and CO_2 formation.

Surface physics (pore structure parameter ψ) and chemistry (kinetic parameters k_j) both have a bearing on carbon reactivity: $r = kS(x, \psi)C_{O2}$, x being the conversion. The goal of Section 4.7 is to describe the effect of surface chemistry (nanostructure) on reactivity in terms of kinetic parameters (k_j) only. Because of the lack of RSA data, meaningful values of ψ cannot be obtained here. As for k_j, the role of chemical carbon structure, it is dealt with as follows: On the basis of a review of carbon structural characteristics in Chapter 1, the effect of the degree of graphitisation on soot oxidation is modelled by specially estimated kinetic parameters. To this end, a kinetic study of the oxidation of carbon materials and an analysis of their differing reactivities are presented. Oxidation experiments of diesel soot and graphite were carried out and kinetics-limited oxidation experiments of graphite and a range of low-mineral graphitic carbons - a carbon black, ethylene flame soot, diesel soot and coke - were modelled. Kinetic parameters k_j are expressed in terms of carbon content. Activation energies in particular, increase with carbon content. The values of k_j enclose intrinsic reactivity effects due to the degree of crystallinity and surface chemistry (RSA/TSA).

4.1 Background

In both DPFs and four-way catalysts, the low-temperature (25 - 850 °C) reaction of soot with the nitrogen oxides present in exhaust is an important aspect. In DPFs, captured soot particles are oxidized by NO_x in the exhaust gas, and in four-way catalysts, the reduction of NO_x to N_2 is also desired. It is therefore of interest to study the kinetics of these reactions. Many studies concerning soot reactivity with NO_x and O_2 are carried out in more or less realistic environments, such as exhaust aftertreatment systems [121, 122], or in laboratory reactors with complex gas mixtures [123, 124, 125, 33]. Global rates of reaction of soot and similar carbon materials with NO_x and O_2 in absence of other reactants are mostly investigated in laboratory reactors [126, 127, 104, 128, 85, 129, 130, 89]. With equal molar concentrations of these feed gases, the rates are generally known to decrease in the following order [30, 131]

$$r_{NO_2} > r_{NO+O_2} > r_{NO} \sim r_{O_2} \tag{4.1}$$

although O_2 was found to be more reactive than NO at temperatures above 900 °C [132]. Not only global reactivity depends on the feed gas; CO/CO_2 ratio, evolution of NO, NO_2 and N_2 also differ widely [133, 131]. Under NO_2, the prevalent C-containing product is CO_2 [85, 134, 33], although a lesser amount of CO is also present and the principal N-containing product is NO [30, 109] (sometimes small quantities of N_2 or N_2O are formed [131]). The reaction of NO with soot yields N_2 and both CO_x depending on temperature [133, 128, 135, 100, 136]. Temperature-programmed experiments (TPEs) show that mainly small amounts of CO_2 are emitted at lower temperatures and larger quantities of CO above 850 °C ca. [128, 137, 108, 104], but that CO tends to decline again at even higher temperatures [104]. This change in favoured reaction product might well be connected with the transition between two Arrhenius regimes of global reactivity [138]. The reaction of carbon with NO has been found to be significant only above 500 °C [139, 140]. Addition of O_2 enhances the reaction of soot with NO [141, 142, 30], and NO and O_2 have been shown to compete for the soot surface [141]. CO and CO_2 evolution with NO and O_2 concentrations representative of diesel exhaust (6-20 % O_2, several hundred ppm NO) resembles that with O_2 alone [30, 143]. At lower oxygen concentrations, characteristics of the reaction with NO start to appear [135]. As under NO, N_2 is formed as well as small amounts of N_2O and some NO_2 [144, 143].

Several studies also investigate the surface intermediates formed during the soot-NO_x reaction via techniques such as FT-IR and DRIFTS spectroscopy [109, 101, 145, 134, 146]. This has allowed for the formulation of elementary or lumped steps leading to the consumption of soot and the formation of gaseous reaction products such as NO, NO_2, N_2, CO and CO_2 [63, 62]. The process is generally considered to start with adsorption of the reactive molecule onto the carbon surface: $C^* + O_2 \rightarrow C^*(O_2)$ [42], $C^* + NO \rightarrow C^*(NO)$ [100], $C^* + NO_2 \rightarrow C^*(NO_2)$ [106, 107, 108]. These ad-species ($C^*(O_x)$, $C^*(NO_x)$) can represent a variety of surface complexes in differing configurations such as the oxygenated lactone, carbonyl and quinone groups [101] and nitrites, nitro compounds or acidic functional groups of the $C^*(ONO_2)$

type [145, 109, 147]. Likewise, C* may represent different types of reactive carbon site [148, 149] It has been suggested that NO may adsorb as an $(NO)_2$ dimer, particularly on microporous carbons [136]. In more lumped models, chemisorption may be represented as dissociative; for instance, the adsorption and dissociation of oxygen is commonly modelled in a single step C* + $\frac{1}{2}$ O_2 → C*(O) [38, 97, 98]. In a similar way, NO may be considered to adsorb dissociatively, splitting into N- and O-complexes, C* + NO → C*(N) + C*(O) [105]. The C*(ONO_2) groups commonly observed on carbons under NO_2 [109, 101, 145] are seen as originating from the interaction of surface oxygen and gas-phase/surface NO_2 [89, 101]. Some authors propose that gas-phase oxygen adsorbs directly on C*(NO) complexes [150, 108] and others the reaction of NO and O while on the carbon surface: C*(NO) + C*(O) → C*(NO_2) [102]. C*(N) obtained from the dissociation of more complex nitrogen groups is found to be very stable [139, 140] and is generally held to produce N_2 at high temperatures, whether via a reaction between two C*(N) [105, 100] or rather by reaction with gaseous NO [151, 104].

However, very few values are known for kinetic parameters which would allow to calculate the rates of these steps in the ordinary conditions of reactor experiments or DPFs, although for some of the global models of the carbon + NO reaction, activation energies and reaction orders have been compiled [126, 152]. In order to reproduce the earlier-mentioned features of soot oxidation, it is clear that a kinetic model must include a number of reaction steps in parallel or series, but it is seldom practical to include all elementary steps, and surface species may therefore be "lumped" together [63]. A mathematical description of the reactor model then allows for extraction of quantitative kinetic data, most commonly by fitting TPEs to the mathematical expressions [62, 153]. In models of this type, a large number of steps and therefore kinetic parameters can lead to ambiguity in the estimation of the latter, as the system is likely to be mathematically underdetermined. It is thus important to strike the right compromise with the level of detail necessary to reproduce all available experimental data [154].

An important consideration for kinetic modelling of soot oxidation is the dependence of oxidative reactivity on the structural characteristics of the soot. This is an issue

common to a number of carbon materials, whose oxidation is of interest in industry. Examples are the regeneration of coked catalysts [155], the oxidation of char [55, 156, 157], and, more recently, the combustion of soot and carbon black in the context of the regeneration of diesel particulate filters [158, 1, 159]. The aim of this section is to create a model capable of describing the low temperature (< 1000 °C) oxidation of a range of carbon materials, despite their widely differing crystallinities and surface chemistries. As shown in Chapter 1, reactivity has been correlated with various parameters characteristic of carbon material structure, including elemental composition [88], surface area [58, 141] and many more microscopic parameters [160, 49, 161, 60]. Depending on the scale of modelling, a number of these may be appropriate for use in models. Although surface area as a macroscopic characteristic is often used in semi-detailed models, it appears uncertain how best to measure this area, as various alternatives have been proposed [162]. Moreover, to our knowledge no model using surface area to represent different carbon materials has been able to predict species selectivity throughout the reactions of soot with NO, NO_2 and/or O_2.

In this section we formulate a detailed mechanism involving five lumped surface species, and show that it is capable of describing the major trends of diesel soot oxidation with NO_x and O_2 in conditions of interest to the functioning of a DPF (25 - 850 °C, 70 - 1400 ppm NO_x, 6 - 20 % vol. O_2 [1]). The kinetic parameters of the mechanism are validated by fitting calculated gas species mole fractions to experimental measurements of the major species NO, NO_2, CO, CO_2 and N_2. It is shown that, with the proposed mechanism, different types of soot or carbon are better modelled by using different kinetic parameters, rather than a surface area.

4.2 Surface Chemistry

Based on the literature, the mechanism in Table 3.1, which is reproduced here as Table 4.1 was proposed as the simplest one capable of producing CO, CO_2, NO, NO_2 and N_2 under all the desired conditions (NO, NO + O_2, NO_2). This means that several surface species are lumped into a single description. C*(O) for instance, represents a whole group of oxygenated functionalities, of different geometries and

Table 4.1: Surface reaction mechanism for soot with NO_x and O_2

	Reaction	**Ref**
R1	C* + 1/2 O_2 → C*(O)	[97, 38, 98]
R2	C*(O) → CO + *	[89, 99, 97, 38, 98]
R3	C*(O) + 1/2 O_2 → CO_2 + *	[97, 38]
R4f	C* + NO → C*(NO)	[100]
R4b	C*(NO) → C* + NO	[100]
R5f	C*(NO) + C* → C*(N) + C*(O)	
R6f	C*(NO_2) + C* → C*(O) + C*(NO)	[101]
R6b	C*(O) + C*(NO) → C*(NO_2)	[102]
R7	C*(NO_2) + C*(O) → C*(ONO_2) + C*	[101]
R8	2 C*(N) → N_2 + C*	[103, 104, 105]
R9f	C* + NO_2 → C*(NO_2)	[106, 107, 108, 109]
R9b	C*(NO_2) → C* + NO_2	[109]
R10	C*(ONO_2) → CO_2 + NO + *	[89, 109, 101]

molecular weights. A single type of carbon site, C*, is proposed, again lumping edge sites, bulk sites, armchair sites etc. into one. The parameters corresponding to the proposed mechanism were fitted with data from the soot-NO, soot-O_2 and soot-NO_2 experiments performed during the course of this study, as well as two separate soot-NO_2 experiments from the literature [89, 85]. It should be pointed out that this process was limited to those studies containing sufficient information on the reactor and reaction products (NO, NO_2, N_2, CO_2, CO profiles). Other possible minor reaction products, such as N_2O were neglected because their concentration is generally not significant.

Parameter estimation was carried out according to the piece-wise technique detailed in Section 3.1 and the values obtained are shown in Table 4.2. In determining the values of soot-O_2 parameters, it was assumed that R2 and R3 are the rate-limiting steps. This is based on the considerations made by Hurt and Calo [38]. In order to ensure that adsorption (R1) was not limiting, the peak ratio of number of oxygenated surface intermediates, C(O), to active carbon sites, C* was maintained greater than 10%, based on the observations of [42]. The chosen value of E_1 was very low, so that the rate r_1 would be significantly higher than the other rates. Consequently, species

Table 4.2: Parameters for the surface reaction mechanism

	$\mathbf{A}_j$ **or** $\mathbf{S}_{0,j}$		$\mathbf{E}_j$ **[kJ/mol]**	**Ref**
R1	5.00×10^{6}	$cm^5/mol^2/s$	45	ts [88]
R2	3.60×10^{5}	1/s	164	ts[a]
R3	8.70×10^{10}	$cm^3/mol/s$	147	ts
R4f	4.80×10^{5}	$cm^3/mol/s$	15	ts
R4b	4.50×10^{4}	1/s	40	ts
R5f	1.00×10^{17}	$cm^2/mol/s$	125	[154],ts
R6f	1.00×10^{17}	$cm^2/mol/s$	57	[154],ts
R6b	1.00×10^{14}	$cm^2/mol/s$	32	ts
R7	1.50×10^{23}	$cm^2/mol/s$	112	ts
R8	1.00×10^{17}	$cm^2/mol/s$	150	[154],ts
R9f	9.00×10^{-7}		0	ts
R9b	1.00×10^{13}	1/s	85	[154],ts
R10	1.00×10^{5}	1/s	70	ts

[a] this study

profiles were more sensitive with respect to the parameters of R2 and R3 than to O_2-adsorption parameters in all cases.

4.3 The Mechanism of Soot Oxidation by O_2

A review of literature for the well-known carbon-O_2 reaction (Table 4.3) gives an idea of the ranges within which the activation energies are to be expected:

reaction	E_a [kJ/mol]
R1	10 - 170
R2	100 - 350
R3	17 - 130

Table 4.3: Literature review of activation energies for reactions R1 - R3 in different carbons [38, 163]

Reaction R1 is the dissociative adsorption of the oxygen molecule: O_2 is adsorbed and dissociates, forming C(O). Influence of C(O) coverage on the reaction rates is neglected. Reaction R2 ($E_a = 100 - 350$ kJ/mol) represents the decomposition of a C(O) complex and the only pathway to formation of the gaseous product CO. According to Hurt and Calo [38], the limiting steps of this three-step mechanism are R2 and/or R3 at $T < 1400$ °C. Reaction R3 is an Eley-Rideal step, representing direct (collisional) interaction between gaseous species and surface complexes. In this mechanism, it is the only path to production of CO_2. Unlike the CO-formation step, there is no agreement in literature on which global reaction to use to describe formation of CO_2 (although clearly there are studies investigating the microkinetics behind these steps [45, 164]). Within our semi-global description, CO_2 evolution can be described by R3 [165, 166]. Like R1, this step is a lumped description of several more elementary steps. It is not very well covered in literature, and only two single values of E_a are found (Table 4.3). The global oxidation rate of the particle will be limited by the slower between production and adsorption steps. According to Hurt and Calo [38], $E_{des} >> E_{ads}$ for most sites. This finding is confirmed by a screening of the literature, as activation energies for CO and CO_2 production assume the largest values, suggesting that formation of CO and/or CO_2 (desorption and complex reaction) are the rate limiting steps in the temperature range $T = 350$-1400 °C. When adsorption is not limiting, the faster of the two parallel formation steps determines the global rate.

When simulating TPOs, the model is capable of capturing the order of magnitude of the dependence on heating rate quite well, as Figure 4.19 shows for a case of coke oxidation (see Section 4.7). Moreover the significant impact of a change in heating rate can be further interpreted in view of Figure 4.2. The ascending slope of the C(O) concentration profile differs for different heating rates; at any given temperature, more C(O) complexes have accumulated on the carbon surface for the lower heating rate. The descending slopes are most likely governed by a competition between the two producing reactions, R2 and R3, and indeed the product profiles rise when C(O) profiles start to descend. From the experimental CO and CO_2 profiles, it can be seen that the ramp has a more significant effect on CO production. This is not surprising, as the CO-producing step, R2, has a higher activation energy. It seems

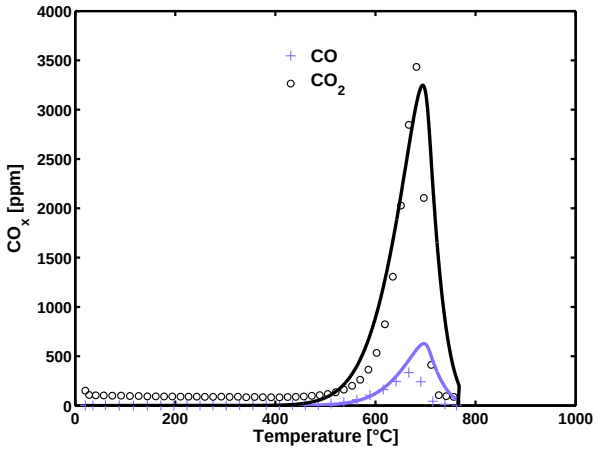

(a)

Figure 4.1: Experimental (symbols) and simulated (lines) species concentrations during TPO of soot with 10% O_2.

likely that the higher concentrations of gaseous products at a higher heating rate are due to reactions R2 and R3 taking place in a temperature range more favourable to CO and CO_2 production, than the temperatures at which they take place at a lower heating rate.

4.4 The Mechanism of Soot Oxidation by NO_2

Figures 4.3-4.10 show measured and/or calculated species profiles from experiments with differing gas composition and Figure 4.6 shows the sensitivity coefficients of remaining soot mass and NO or NO_2 mole fraction with respect to the rate constants. The model described in Chapter 3 was coupled with the kinetic parameters in Table 4.2 for simulations of all the soot oxidation experiments. In this chapter, the balance for species i is written as

$$Q\Delta x_i = Q(x_{i,feed} - x_{i,measured}) \tag{4.2}$$

for each instant of measurement, where Q is the molar flow rate and x_i the mole fraction of the ith species. The amount of i not accounted for by measured species concentrations is represented by Δx_i.

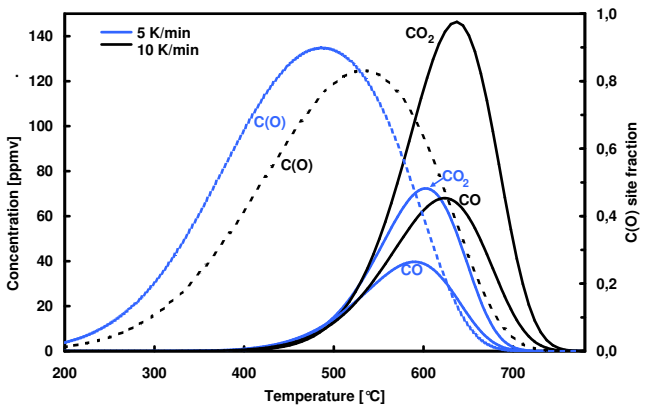

Figure 4.2: Impact of heating rate on simulated CO and CO_2 concentrations. TPOs of coke with 2% O_2.

Experimental curves for NO_2 adsorption on carbon black and subsequent temperature programmed desorption (TPD) are taken from Jeguirim et al. [89] and shown in Figure 4.3 together with calculated mole fractions. During adsorption, some NO_2 is consumed and NO is formed. Using the definition given earlier on in Equation 4.2, $\Delta x_N = x_{NO_2,in} - x_{NO_2} - x_{NO} = x_{NO_2,in} - x_{NO_x} > 0$. If no N_2 is formed, ΔN moles of nitrogen accumulate on the surface. During TPD, both NO_x and both CO_x are evolved. In contrast with what is known from IOs, the amount of CO_2 is not much larger than CO, but it is formed at significantly lower temperatures. From an oxygen balance, the amount of O on the carbon surface is $\Delta x_O = 2x_{NO_2,in} - 2x_{NO_2} - x_{NO}$. The amounts of nitrogen and oxygen atoms evolved during TPD are, according to the authors of the experiment, in reasonable agreement with those stored during adsorption; therefore no species other than those shown in Fig 4.3 are formed. The sharp NO_2 peak upon switching to TPD is not reproduced in simulations. According to the authors, this represents physisorbed NO_2, which is not accounted for by the mechanism in Table 5.1. The overall trends of NO_x and CO_x production are well described by the model. It reproduces the first (and major) CO_2 peak correctly, but not the later CO_2 formation. For CO, low-temperature reactivity is underestimated.

Together with the above TPD, an IO experiment of diesel soot at 400 °C with 880 ppm NO_2 by Tighe et al. [85] was used to fit parameters pertaining to NO_2. Exper-

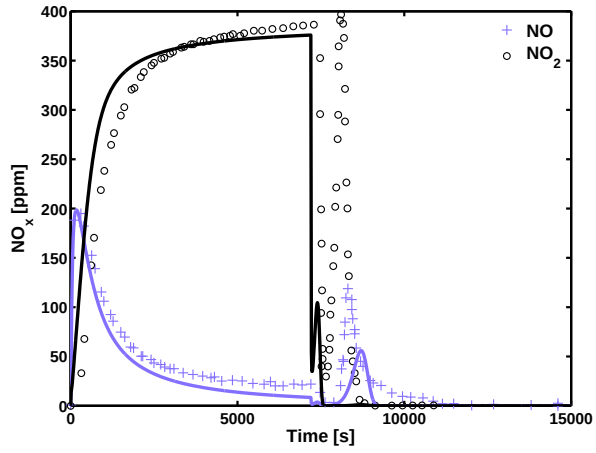

(a)

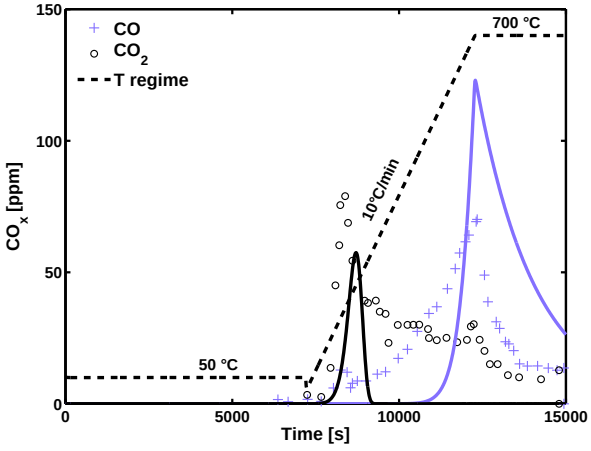

(b)

Figure 4.3: Experimental [89] (symbols) and simulated (lines) species concentrations during adsorption under 400 ppm NO_2 at 50 °C and subsequent TPD under He.

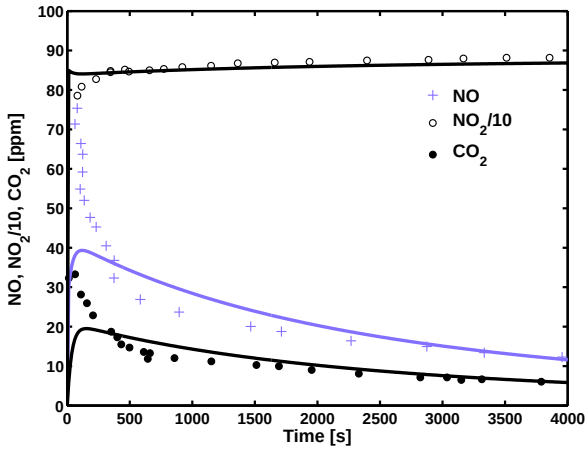

Figure 4.4: Experimental [85] (symbols) and simulated (lines) species concentrations during IO of soot at 400 °C with 880 ppm NO_2.

imental mole fractions and the corresponding model fit are shown in Fig.4.4. The small amount of CO which is formed (∼1 ppm), is not shown. According to N and O balances by the authors, NO_2 and NO are the only N-containing species, and the oxygen in the products all originates from feed NO_2. No sufficiently detailed TPO results were available for NO_2, so the parameters were fitted using the TPD and IO above. The parameters thus obtained, in Table 4.2, allowed for the simulation of the hypothetical NO_2-TPO in Fig. 4.5. It is known from literature that NO is produced immediately upon exposure to NO_2 and that CO_2 is much more abundant than CO, and these general features are reproduced by the model in Fig. 4.5. As may be seen in Figure 4.5c, simulations also allow for the observation of the "lumped" surface species proposed in the mechanism (Table 5.1).

A balance for the NO_2-TPD in Fig. 4.3 showed that $2\Delta x_N < \Delta x_O$; therefore all surface species cannot be of the C*(NO_2) form and some other surface complexes must be present. This is not surprising, the existence of several functionalities has been proven [101]. Muckenhuber and Grothe showed that NO_2 is initially bound to the surface in a step such as R9f [101]. In the model, it represents the order of surface groups stable under NO at progressively higher temperatures. C*(NO_2) is seen not to be stable at temperatures below 200 °C. Thus, it is instantly converted to C*(NO) upon adsorption of NO_2 at low T (Fig. 4.5). The value of the sticking coefficient

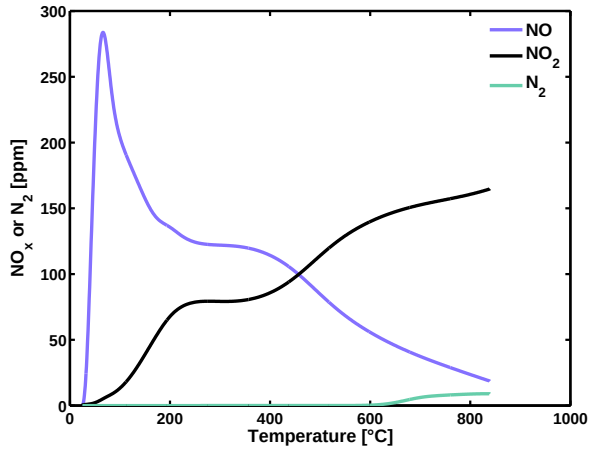

(a)

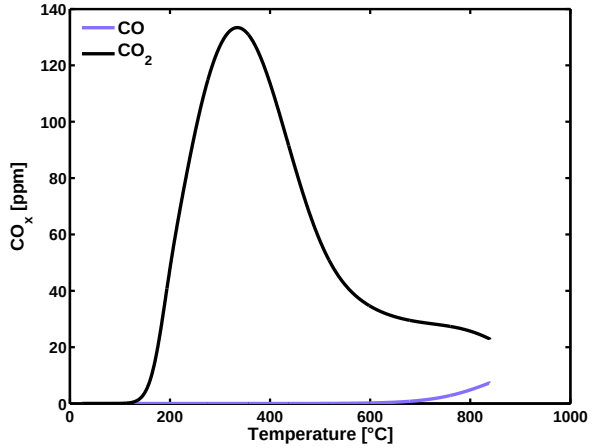

(b)

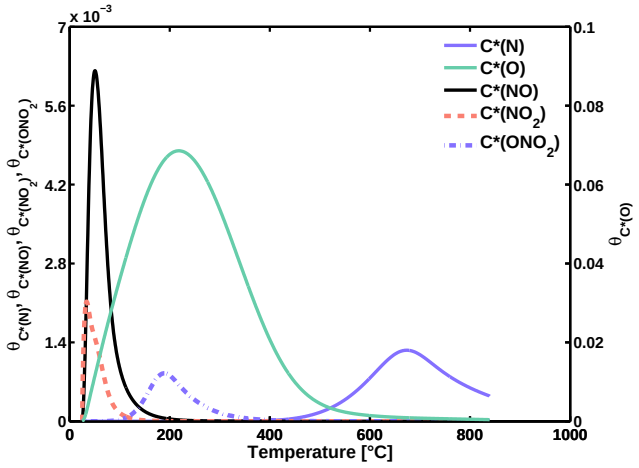

(c)

Figure 4.5: Simulated species concentrations during TPO of soot with 200 ppm NO_2.

of NO_2 on soot, found in this study to be 10^{-7} (Table 4.2) fits well into the range of values from literature (10^{-4}-10^{-8}, [167]). It was also shown that C*(NO_2) splits up at higher temperatures, forming a carbonyl group, C*(O), according to reaction R6f. The CO_2 profile is known to exhibit two peaks, one between 600 and 700 °C, which concurs with the CO peak and is found to originate from functionalities of the C*(O_x) type, for e.g. those formed earlier in R6f. The other is formed at ca. 140 °C and is likely due to formation and decomposition of an acidic group C*(ONO_2), resulting in $CO_{2\ (g)}$ and $NO_{(g)}$ [101, 89, 145]. Reactions R7 and R10 describe this process and R10 allows for the reproduction of the CO_2 peak at 140 °C. However the proposed mechanism currently includes no CO_2-desorption reaction involving C*(O_x) and the second CO_2 peak is therefore not reproduced in Figures 4.3 and 4.5. Similarly, low-temperature CO formation in Figures 4.3 and 4.5 is underestimated by the model and this could well be improved by letting a second type of oxygen functionality produce some CO too, as suggested in the literature. In Figure 4.5c, the simulation with the kinetic parameters of Table 4.2 shows how the functionalities succeed each other in the order C*(NO_2) → C*(NO), C*(O) → C*(ONO_2) proposed in literature.

Sensitivity coefficients were calculated for instantaneous soot mass and NO_x mole fractions with respect to all rate constants. For each case, rate determining and other important steps vary with T. Overall, one may distinguish a high and a low temperature regime, as there is either a significant change in rate determining step or a significant difference in activity below and above 600 °C. For instance, NO adsorption under NO mainly occurs above 600 °C, whereas under NO + O_2 it occurs below this temperature. Under NO_2, NO_2 adsorption is determined by R9b below 600 °C and above by R6b.

According to the sensitivity analysis, the steps which are determining for global reactivity of the reaction between soot and NO_2, are R7 in the low-temperature regime and R9f,b at higher temperatures (Fig. 4.6d). The sensitivities towards all other parameters are smaller. Major reaction paths in the model are shown in a schematic way in Figure 4.7a. Below 600 °C, the formation of C*(ONO_2) via R7 controls soot consumption, NO_2 on the surface is abundant. At higher temperatures however, des-

orption of NO_2 starts to become significant and soon the number of C*(NO_2) surface functionalities limits CO_2 production; the adsorption/desorption steps R9 are rate limiting. At this point C*(O) prevails on the surface as compared to C*(NO_2) (Fig. 4.5), and instead of forming C*(ONO_2), it starts to be channelled into CO via R2. To form CO at lower temperatures, another CO-producing surface species would have to be introduced, as has already been suggested.

Although both are dynamic (i.e., temperature programmed) experiments, there are some differences between the TPD and the TPO of soot with NO_2. In essence, as seen by the model, these dissimilarities come down to two causes: the differing duration and temperature of adsorption. Around 150 °C, CO_2 production starts for both TPO and TPD. The latter experiment however, causes the coverage of C*(O), C*(NO_2) and C*(ONO_2) to be two orders of magnitude greater than in the TPO. Despite this, the CO_2 peak is larger for the TPO, because NO_2 adsorption continues and therefore feeds the CO_2 formation process. But in the TPD, sufficient C*(O) is still on the surface when C*(NO_2) and C*(ONO_2) have been consumed, and it can go on to form CO at a somewhat lower temperature than is possible in the TPO. This particular behaviour remains to be validated experimentally.

4.5 The Mechanism of Soot Oxidation by NO

Figures 4.8a and b show the results from TPO of soot under 200 ppm NO. At first, NO remains constant at the inlet value, but is consumed from ca. 300 °C onwards. From a nitrogen balance at every instant of time, the amount of N atoms not accounted for by either NO or NO_2 can be calculated as: $\Delta x_N = x_{NO,in} - x_{NO_x}$. Since no NO_2 is observed, $\Delta x_N > 0$; therefore some other N-containing species is being formed. Because no N_2O was detected, this is presumably $N_2 = \Delta x_N/2$, which is shown in Figure 4.8a.

An oxygen balance over soot shows that there is more O in the products than in the feed (NO_{in} - NO - CO - $2CO_2 > 0$); this discrepancy, likely due to previously adsorbed oxygen, is found to constitute approximately 63% of O in the final prod-

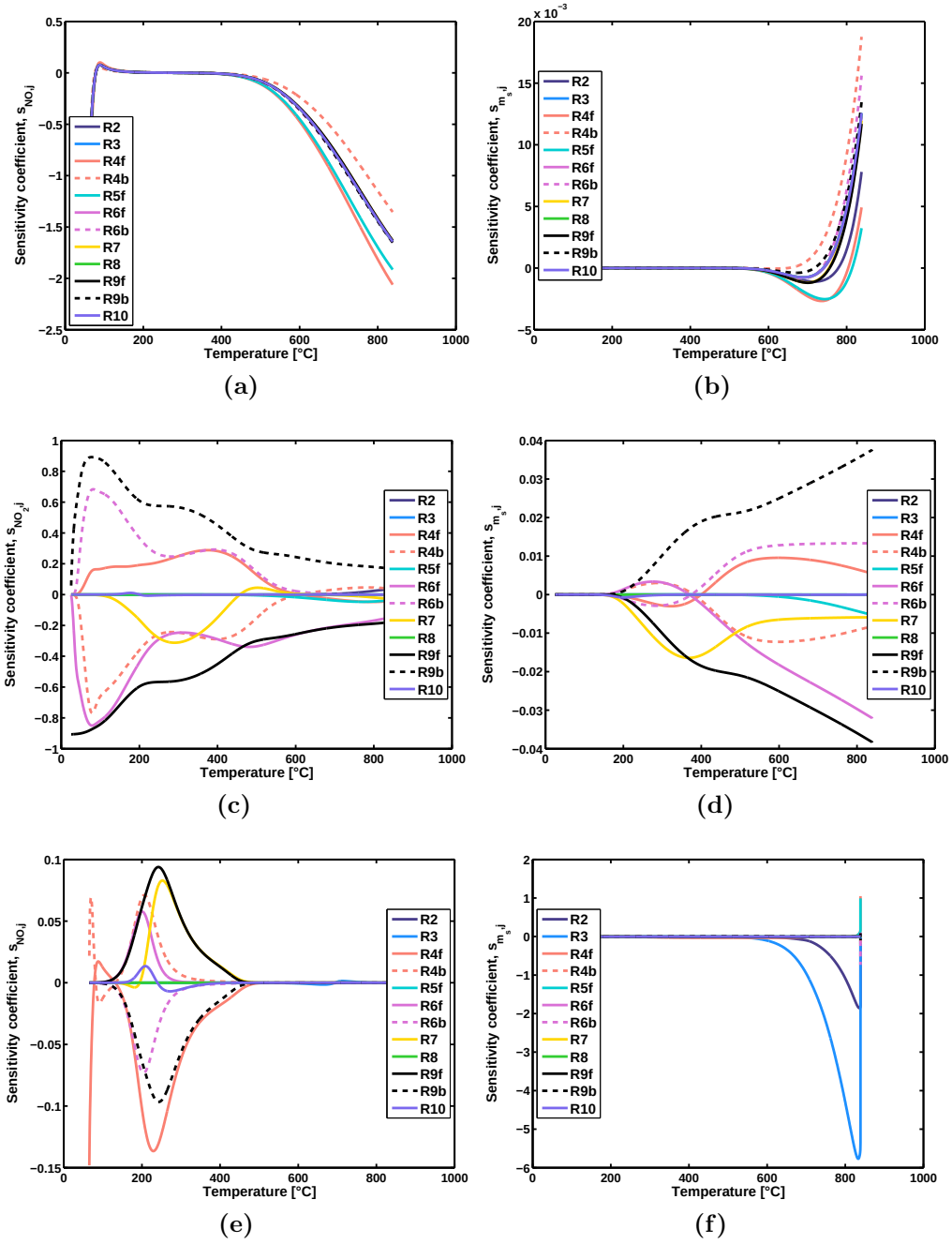

Figure 4.6: Sensitivity coefficients of NO or NO_2 mole fraction and remaining soot mass m_s with respect to the rate constants, calculated for TPO of soot with 200 ppm NO (a,b), 200 ppm NO_2 (c,d) and 200 ppm NO+10% O_2 (e,f).

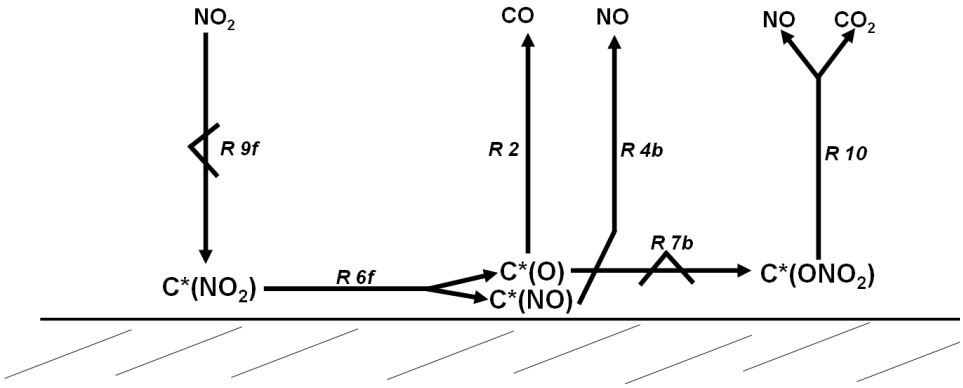

(a) NO_2

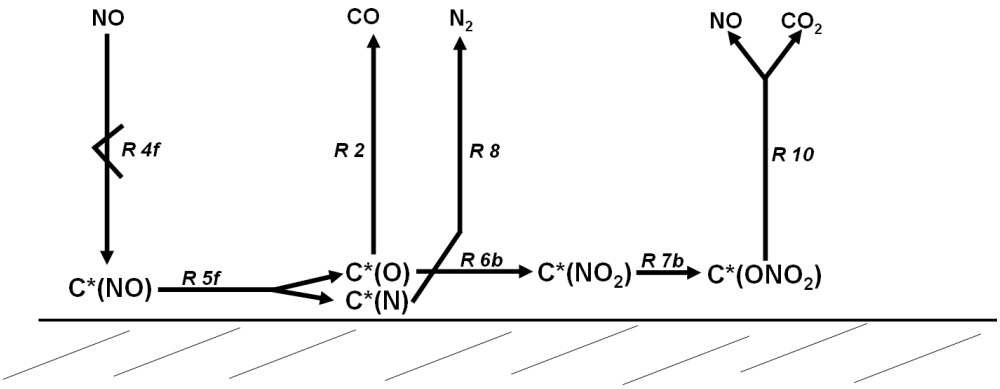

(b) NO

Figure 4.7: Schematic depiction of the main steps of the soot-NO_x reactions according to the mechanism in Table 5.1, the rate determining steps are designated with the appropriate symbol.

ucts CO and CO_2 below 350 °C. Above this temperature, the percentage drops to 42 %. It is then not necessarily surprising that the model does not reproduce low temperature CO_x and N_2. Note also that SOF, which is often cited as the cause of erratic low-temperature reactivity [168, 169], was not removed from the soot after collection. The CO_2 profile can be improved by specifying an initial surface concentration of $\theta_{C*(O)}$=0.01, but CO is not affected by this measure.

There is considerable evidence of a break in the Arrhenius plot of the global rate constant for carbon oxidation by NO [138]. The breaking point is located anywhere between 600 and 800 °C. It separates a low- and a high-temperature regime, the latter of which has been found to have a larger activation energy. Values identified in the literature are comprised between 120 and 240 kJ/mol. For the low-temperature regime, the review by Aarna and Suuberg finds activation energies of 40 - 88 kJ/mol [138]. Here the global activation energy calculated on the basis of the mechanism in Table 4.2 is found to be 134 kJ/mol between 600 and 850 °C. The value was determined from the simulated reaction rate in a series of IOs. Below 600 °C the model is not capable of describing oxidation by NO. Hence, the proposed combination of mechanistic parameters suitably characterizes the soot-NO reaction only in the high-temperature regime (600 - 850 °C). For the purpose of simulating the reaction of soot with diesel exhaust in a DPF this is probably sufficient, since C-NO reactivity is insignificant below 600 °C (ref. Fig. 4.8), especially in comparison with the other reactions occurring at these temperatures. Moreover, since 42 - 63% of oxygen in reaction products stems from previously adsorbed O, an attempt was made to improve the fit by starting the simulation with $\theta_{C*(O)} = 0.02$. This measure enables CO_2 production at lower temperatures (dashed line, Figure 4.8b). However it does not affect CO. A second CO-producing reaction involving a different oxygen functionality might well be needed to reproduce low-T CO.

Very little information concerning the functionalities on the soot surface during reaction with NO is available in the literature. Zawadzki et al. find an almost unchanged FT-IR spectrum after adsorption, suggesting that very little NO is adsorbed at room temperature [144]. The measured NO mole fraction in Fig. 4.8a also indicates that the reaction with the soot surface only starts at 500 °C. In the model the reaction

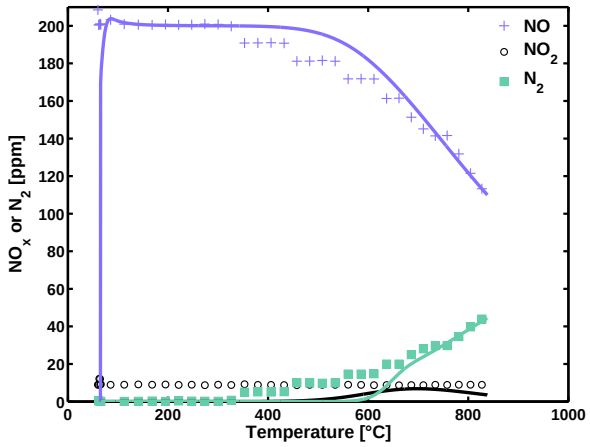

(a)

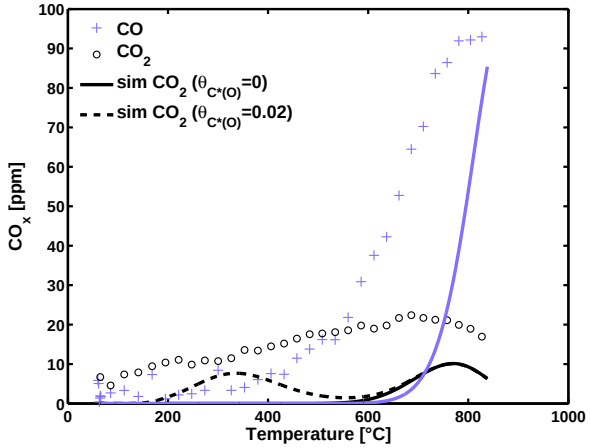

(b)

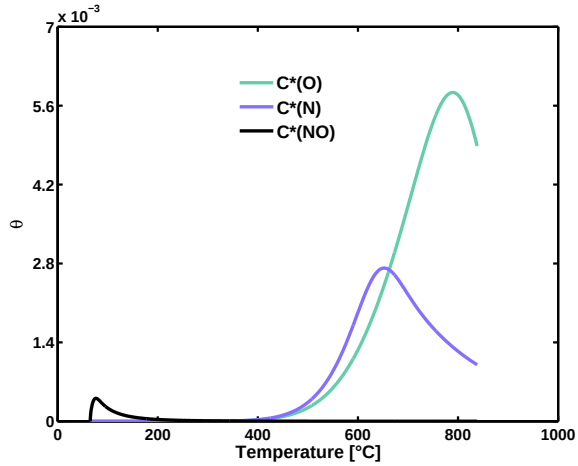

(c)

Figure 4.8: Experimental (symbols) and simulated (lines) species concentrations during TPO of soot with 200 ppm NO.

of NO has to proceed via R4f (Fig. 4.7b) and the coverage with adsorbed species is clearly much smaller than under NO_2. The low pre-exponential factor and non-zero activation energy of this reaction render the adsorption of NO much less effective than that of NO_2. Some C*(NO) accumulates on the surface below 200 °C, but above this temperature, surface reactions R5 and R6 (Fig. 4.11) become more significant. C*(NO) is split up into C*(N) and C*(O) (R5f, Fig. 4.7b) and consequently N_2 desorbs from C*(N). Reactions R6b, 7b, 8, 10 and to a smaller extent 9b, allow for regeneration of C* sites, on which more NO can be adsorbed. While under NO_2, all adsorbed N atoms are liberated again as gaseous NO, the same is not true under NO. Here C*(NO) is preferentially split up via R5f and the remaining C*(N) has no other option but to form N_2. The succession of the surface species in the order C*(NO) $\rightarrow$ C*(NO_2) $\rightarrow$ C*(ONO_2) $\rightarrow$ C*(N), C*(O) can be observed in Fig. 4.8c.

The oxidation of C by NO_2 is probably aided by the fact that twice as many O atoms are available, and once adsorbed, only two steps are necessary to form C*(ONO_2). In order to form one mole of CO_2, two moles of NO_2 are sufficient according to R10, but three moles of NO are needed. Thus it is not surprising that the C+NO_2 reaction is not as sensitive to the adsorption step as the C+NO reaction (compare the magnitude of the sensitivity coefficients in Figures 4.6a and e). The sensitivity analysis confirms that it is R4f which controls the adsorption of NO over the whole temperature range, although it is much more active above 600 °C. It also controls the global reaction (consumption of soot) to form CO_2 at 600 - 750 °C (Fig. 4.6a,b). Above 750 °C, the rate determining step for the global reaction is R4b, as NO desorption becomes more efficient. This change in rate determining step occurs at about the same temperature as the switch from CO_2 to CO as the chief reaction product. Furthermore, the second most important reaction also changes, it being R5f at first, and then R6b. Once on the surface, C*(NO) can follow two possible paths, as depicted in Fig. 4.11b, namely R5f or R6b. From the rates of production (ROPs), it can be seen that R5 contributes most to the consumption of C*(NO). But while R6 is also significant, its importance decreases starting at 750 °C. This causes progressively fewer C*(NO_2) and C*(ONO_2) to be formed, with the result that CO_2 production is limited. But CO is produced in ever greater quantities as C*(O) is continually produced via R5f.

4.6 The Mechanism of Soot Oxidation by NO + O_2

NO_x and CO_x profiles from soot oxidation with 200 ppm NO and 10% O_2 are shown in Figure 4.9. In contrast with the reactive feed containing NO only, here a certain quantity of NO is adsorbed and converted into NO_2 due to the presence of O_2, but only below 350 °C. NO_{in} and NO_x overlap, therefore no other N-containing species such as N_2 or N_2O are formed.

Δx_O, calculated as $x_{NO,in}$ - x_{NO_x} - $2x_{CO_x2}$ - x_{CO} exhibits a large negative peak between 500 and 700 °C. Since the CO_x profiles are nearly identical to those obtained under O_2 only (Fig. 4.1), most O atoms in CO_x are likely to originate from gaseous O_2. This is also supported by the fact that no NO is consumed at these temperatures. However the precise contribution of pre-adsorbed O cannot be determined, since no quantitative measures of O_2 concentration were made. The possible contribution to NO_2 of O atoms originating from adsorbed NO is calculated as ($x_{NO,in}$ - x_{NO})/$2x_{NO_2}$. It accounts for 50% as long as NO_2 production lasts (between 100 and 300 °C). If n is the number of moles of nitrogen atoms consumed from NO, n is also the number of moles of nitrogen atoms to be found in NO_2. 50% of moles of O in NO_2 amounts to $2n/2$ = n. If all of the 50% (n) comes from NO, then a further n moles of oxygen in NO_2 must come from gaseous O_2 or previously adsorbed O. To distinguish the exact contributions of these three sources of oxygen is not possible from the measurements, nor can one *a priori* assume that exactly n and no fewer moles of O in NO_2 originate from consumed NO.

Simulation of soot oxidation with 200 ppm NO and 10% O_2 in Figure 4.9 fits the experimental data quite well, with the exception of NO and NO_2 below 100 °C. It seems likely that this is due to pre-adsorbed O and the dashed lines in Fig. 4.9 show that a simulation with a non-zero amount of O on the surface leads to a better agreement with measured NO_2.

CO_x formation is very similar under 10% O_2 and 200 ppm NO + 10% O_2, although there is a slight increase in CO_2 mole fractions between 450 and 650 °C when NO is added. In the calculated profiles, this small gain in CO_2 is seen at a slightly lower temperature. Results from simulated TPOs with 200 ppm NO and 0.02 - 5% O_2 are shown in Fig. 4.10. It can be seen that there is a gradual transition between the case with no O_2 and that with 10% O_2. As the fraction of oxygen increases, NO_2 production increases too and is shifted to slightly lower temperatures. Also, NO adsorption becomes less marked at high temperature and N_2 becomes progressively less abundant. Overall CO_x formation increases and so does the CO_2/CO ratio.

It is generally acknowledged that the addition of O_2 improves the global rate of the C+NO reaction (i.e. CO and CO_2 formation) [30]. The experimental results in Figure 4.9b support this, as CO_2 production starts ca. 50 °C earlier and the peak is about 300 ppm greater than under O_2. The CO peaks are almost indistinguishable. In the model, the production of C*(ONO_2) under NO + O_2 causes a small augmentation in CO_2 mole fraction, although it occurs earlier than in the experimental profile.

It is also accepted that chemisorption of NO on carbon is enhanced by the presence of O_2 [150, 142]. At typical chemisorption temperatures of 60 - 200 °C [109], our results in Fig. 4.9a do indeed show an improved consumption of NO. As under NO only, NO consumption is most sensitive to R4f (Fig. 4.6e). However, according to the N balance (Section 4.5), all of this NO adsorbed at low T is transformed into NO_2. At higher temperatures on the other hand, the trend is reversed and no significant quantity of NO is adsorbed, in contrast with the findings for soot+NO only (Fig. 4.8). Consequently, no N_2 is observed in presence of O_2. It can be expected that there is more C*(O) on the surface when O_2 is present (compare calculated C*(O) coverages in Figures 4.9c and 4.8c) and that C*(NO) preferentially reacts with this C*(O). The calculated rates of production in Figure 4.11 support this idea: under NO+O_2, 100% of NO adsorbed by R4 goes on to create C*(NO_2) via R6 and ultimately C*(ONO_2) or NO_2. But under NO alone, a very large fraction of adsorbed NO splits up via R5f. Most nitrogen atoms therefore end up as C*(N) and this is the reason why N_2 is produced under NO.

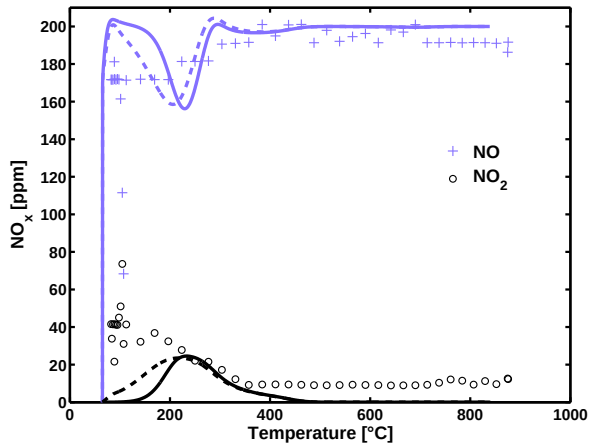

(a)

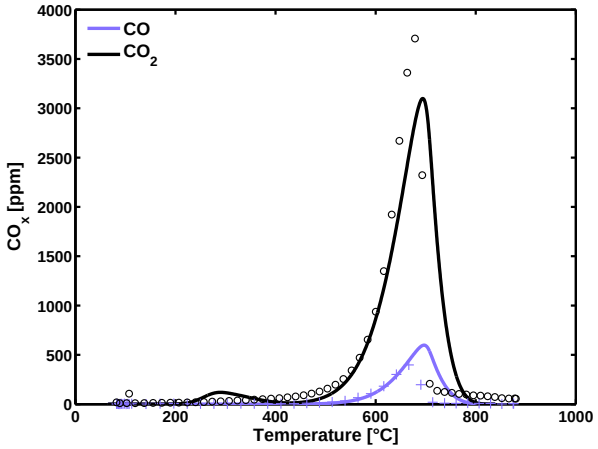

(b)

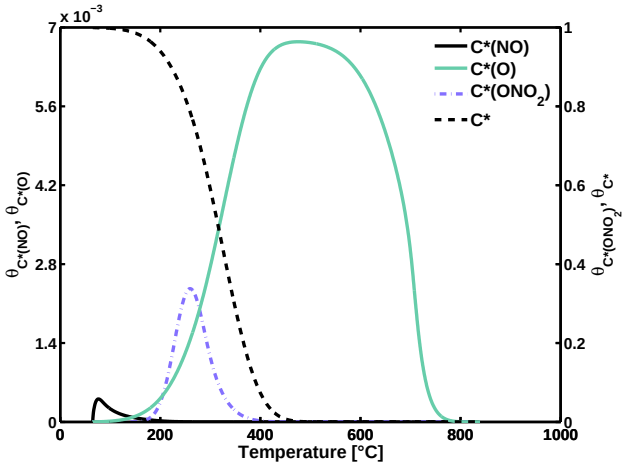

(c)

Figure 4.9: Experimental (symbols) and simulated (lines) species concentrations during TPO of soot with 200 ppm NO and 10% O_2. Dashed lines represent simulation with $\theta_{C*(O)} = 0.1$

.

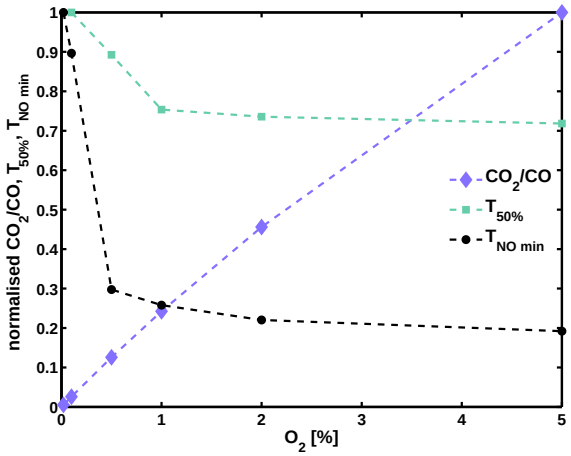

Figure 4.10: Maximum CO_2/CO ratio, temperature at 50% conversion and temperature at minimum x_{NO}, all normalized with the respective maximum values and calculated for a TPO of soot with 200 ppm NO and varying amounts of O_2.

Another difference between the two cases is that NO adsorption takes place at much lower temperatures when O_2 is present, the peak of C*(NO) production by R4f is centred at 300 °C as opposed to 800 °C under NO. In the literature it is not clear whether the enhancing effect of oxygen is due to formation of gaseous NO_2 which then goes on to react with soot, or rather due to the reaction between NO and oxygen functionalities. As under NO only, the rate determining step for NO chemisorption is R4 below 400 °C. However, the sensitivity analysis indicates that, as the oxygen mole fraction increases, R5f becomes gradually less important. Instead, R6, R7 and R9 are important for NO adsorption in presence of oxygen: adsorbed NO rapidly reacts with the readily available C*(O). This leads to more NO being adsorbed. When no oxygen is available, the only path of NO consumption is R5f. Since this reaction has a much higher activation energy than R6, it only becomes important at higher temperatures; only around 400 °C does it cause more NO to be adsorbed. In the model, the improved reaction rate in presence of O_2 is therefore caused by a shift in the equilibrium of the couple R4f-R4b. This shift is a consequence of the differing importance of reactions R5f and R6b competing for C*(NO).

A comparison of the ROPs of O_2 and (net) NO adsorption (R1 and R4) shows that

the majority of oxygen atoms on the surface originate from O_2. Of those coming from adsorbed NO, only a small percentage go on to form CO_2 between 200 and 400 °C via R10, thus slightly increasing total CO_2 production (mainly by R3) at these temperatures. At lower oxygen concentrations, the proportion of O originating from NO increases as does the proportion of CO_2 produced by R10. The effect of pre-adsorbed oxygen can be simulated by initializing with a non-zero coverage, $\theta_{C*(O)}$=0.1. As may be seen from the dashed lines in Fig. 4.9a, the main effect of this is to improve early production of NO_2.

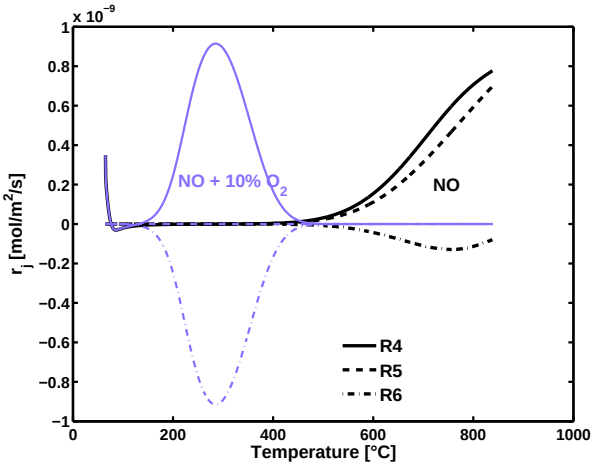

(a)

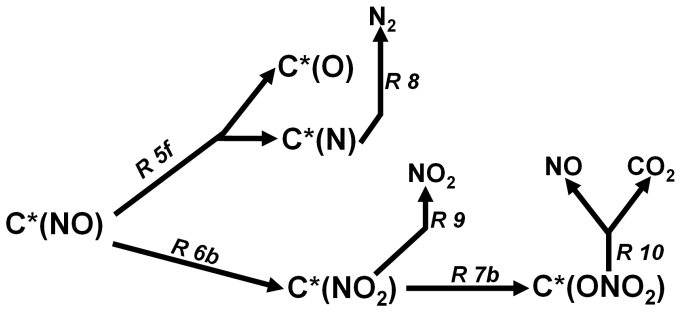

(b)

Figure 4.11: The competition for C*(NO): Rates of production according to Eq.3.10, calculated for TPO of soot with 200 ppm NO and 200 ppm NO + 10% O_2.

Note that using the parameters found in this study to simulate TPOs for different reactive feeds allowed us to verify the global accuracy of the model. Although mass consumption was not measured for all the cases, simulated remaining mass shows that the well known order of reactivity of the feed gases is respected (Fig. 4.12). NO alone is the least active oxidant, and NO+O_2 (in equal concentrations) just a little more reactive. At concentrations of 200 ppm, NO_2 is the most reactive soot oxidant. However, in conditions likely to occur in diesel exhaust gas (several % of O_2 and a few 100 ppm of NO_x), the effect of O_2 on soot oxidation in a (uncatalysed) DPF is the most significant above 600 °C. Below this temperature, NO_2 remains more active.

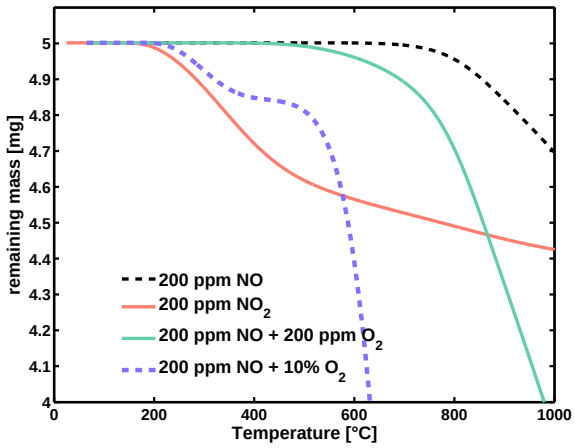

Figure 4.12: Predictions of global reactivity of soot with different reactive gases.

4.7 The Role of Soot Structure and Surface Area

Kinetic models commonly describe the rate of carbon oxidation as $r_j = k_j \cdot S_a$. Interpretation of the two factors may vary, but on the basis of considerations in Chapter 3, the common reactive surface area RSA approach is not used in this study. Instead, the value of S_a is calculated from a material balance on the reaction products CO and CO_2. This means that the total quantity of active sites taking part in the reaction is given by the product $S_a \cdot \Gamma$. Thus it does not correspond to BET surface area (Table 4.4), also known as total surface area (TSA), but it is also not the actual RSA [170, 160, 114]. RSA is in fact constituted by only those sites covered by surface

complexes reactive enough to decompose and give CO or CO_2. It is therefore only a fraction of the TSA or BET area [171, 69] or of the S_a used here and is a measure of chemical structure (arrangement of active carbon sites or degree of graphitisation) of the carbon. In some of the simulations in this chapter, S_a is seen as evolving with pore structure (Bhatia-Perlmutter random pore model). In other words, S_a here describes the physics of the carbon surface, whereas the contribution of chemical structure to oxidation rate is contained in the rate constant k_j. This interpretation is a modelling choice, and differs from the RSA-approach.

Very few studies provide an adequate evaluation of ψ, since it is difficult to separate effects of the two factors in $r_j = k_j \cdot S_a(\psi)$. A fit of ψ as a function of temperature during oxidation of char is presented by Li et al. [114], but as pointed out by the authors, the theoretical significance of these variations needs further examination. Here the default choice for all simulated cases was to set $\psi = 0$, i.e., to assume that active surface area is constant with respect to reaction progress. We chose $\psi \neq 0$ only in those cases where it was impossible to otherwise achieve a good fit, or when more information was available. For the data on char, $\psi = 2$ was evaluated in the original paper [42]. A tentative value of the reactive surface area S_a is used at first, based on the value of active site concentration, Γ, typical for the material in question Table 4.4. Initial S_a is then derived from the conservation of mass (i.e. $m = \int_0^1 S_a(x)\ M_C\ \Gamma\ dx$). Overall, $\psi \neq 0$ resulted for those carbons with particularly high BET surface areas (Table 4.4). Although it can be presumed that these materials are sufficiently porous in order for pore evolution to have an impact on reactivity (i.e. $\psi \neq 0$), the procedure evidently entails some uncertainty which is implicitly enclosed by the pre-exponential factors.

Choosing to enclose chemical structure of carbons in the rate constant k means that different kinetic parameters may be estimated for differently structured carbons. In this section, k_2, k_3 and k_{10} are estimated for a range of different carbon materials. Firstly, a comparison of the results from TPO of soot and graphite under 200 ppm NO (Figures 4.13a, b and 4.14a, b respectively) justifies the above-mentioned choice show . NO consumption over graphite, also in Fig. 4.14a, is almost indistinguishable from that over soot, although graphite is clearly much less reactive in terms of CO_x

production (Fig. 4.14b). The nitrogen balance for Fig. 4.14 indicates that a similar amount of N_2 is produced over graphite and soot (Fig. 4.14a). In order to simulate oxidation of graphite, the parameters of R2 were changed. An oxygen balance for graphite shows that more O atoms are consumed from NO than are subsequently liberated in CO_x; a certain amount of oxygen thus stays on the graphite surface.

Although NO mole fractions are very similar in the two cases, CO and CO_2 formation is much less significant for graphite. We exclude transfer limitation effects by calculating the Thiele Modulus as in Chapter 3. It is of course a well-known fact that more graphitized materials such as graphite are less reactive than, say, soot. This means that graphite only starts being consumed at much higher temperatures than soot, as is indeed confirmed in Figures 4.8 and 4.14. But since the only source of oxygen, NO, is being consumed at the same rate approximately, more O is clearly stored on the graphite surface. Some parameter inherent to CO_x production but not to NO chemisorption must therefore be responsible for the observed behaviours.

According to the literature, CO_x formation (soot consumption) is proportional to the TSA, i.e. BET, or more commonly, RSA, which is measured as that area covered by oxygen complexes reactive enough to decompose into CO and CO_2 at a given temperature [171, 69, 114]. Whether NO chemisorption activity can be correlated with BET area of carbons is disputed. Some, like Illán-Gómez et al. [137] find that the onset of NO consumption is proportional to BET area, but many others see no relation [172]. Our experimental findings for soot and graphite do not follow the pattern found by Illán-Gómez et al., despite the fact that BET area of graphite (4 m^2/g in our case) is much lower than that of soot (414 m^2/g). Considering these incongruities in the literature, it seems probable that the explanation for this behaviour should be sought at a more detailed level of representation. It might, for instance, be due to the presence of different reactive sites with different geometries; some of which are responsible for the attachment of NO to the carbon surface and others for the release of CO_x from the carbon surface. Graphite would then contain fewer of the latter type of site than soot.

In a model of our type, where surface area is used only to quantify the amount of

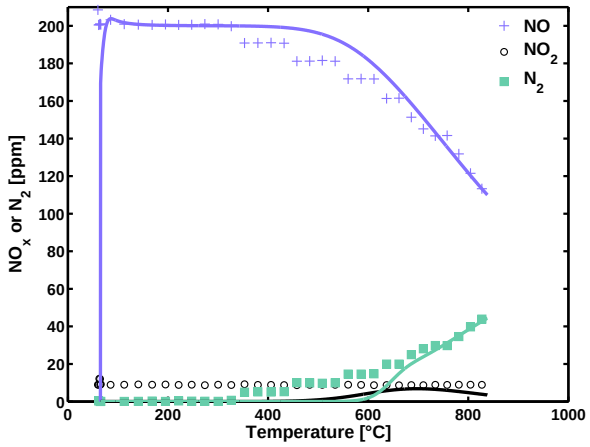

(a)

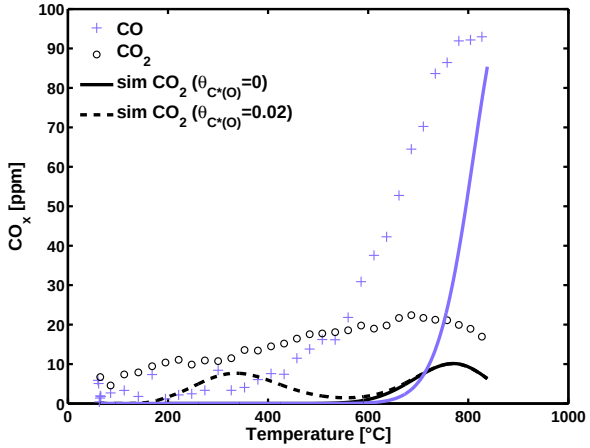

(b)

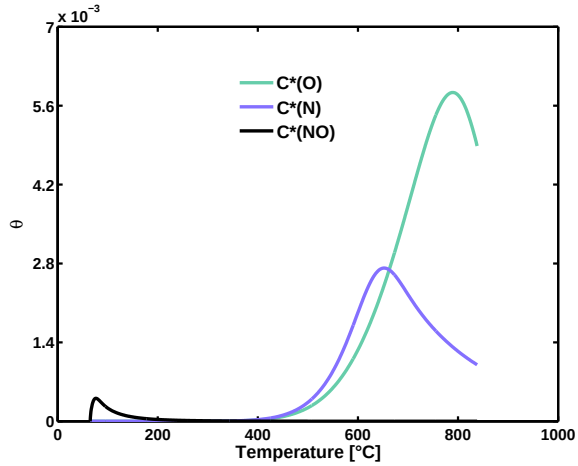

(c)

Figure 4.13: Experimental (symbols) and simulated (lines) species concentrations during TPO of soot with 200 ppm NO.

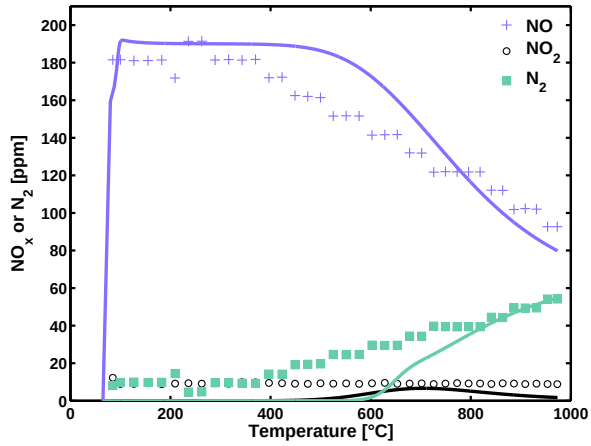

(a)

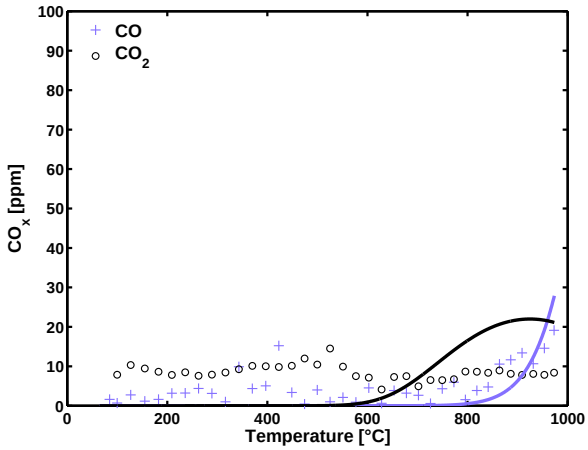

(b)

Figure 4.14: Experimental (symbols) and simulated (lines) species concentrations during TPO of graphite with 200 ppm NO.

Table 4.4: Sources of data on oxidation of carbons

Material	H/C[a]	O/C[a]	%C[ab]	ash[g]	BET[f]	Γ[h]	Reactor	Type	Ref
FCC coke	0.75	0.047	53	1.07	6	$2.7{\cdot}10^{-5}$	FB	TPO	[97][c]
char	0.47	0.067	65	9.00	425	$3.3{\cdot}10^{-4}$		TGA	[42][d]
ethylene soot	0.13	0.0019	88	0.00	105	$7.1{\cdot}10^{-3}$		TGA	[173]
diesel soot	0.069	0.059	89	0.32	414	$2.7{\cdot}10^{-5}$	FB	IO	
carbon black	0.050	0.0087	95	0.30	30	$3.3{\cdot}10^{-4}$	FB	IO	[133][e]
graphite	0.00	0.00	100	0.00	4	$3.2{\cdot}10^{-5}$	FB	IO	
graphite	0.00	0.00	100	0.00	10	$3.2{\cdot}10^{-5}$	FB	TPO	[174]

[a] molar values
[b] Most values calculated assuming the carbon to be composed of only C, H and O
[c] Typical composition from [175, 176]
[d] carbon composition from [177]
[e] carbon composition partly from personal communication with author
[f] [m^2/g]
[g] [wt.%]
[h] [$mol/m^2/s$]

carbon present, the observed differences between the behaviours of soot and graphite could not be modelled by changing the surface area. This would affect all reactions, and a smaller area would make both NO consumption and CO_x production less efficient. However, using different CO and/or CO_2 production parameters (E_2 = 190 kJ/mol , $A_2 = 4.00{\times}10^4$ s^{-1}) as done in a previous study [88] allows us to reproduce the lower reactivity of graphite whilst not altering NO consumption significantly (lines in Figure 4.14). At the scale of modelling which we use here, it thus makes sense to include chemical structure (i.e. arrangement of C atoms) in the intrinsic reactivity (i.e. the kinetic parameters) of the examined carbon material.

The scope thus is to distinguish the oxidative parameters of carbons displaying differing crystallinities and surface chemistry. The idea is to characterise each carbon in terms of a simple bulk parameter, such as routinely available elemental carbon content. Considering the complex surface chemistry of this reaction, it is likely that more than one reaction step will have to depend on carbon structure to be able to predict rate and CO/CO_2 product ratio over a large range of conditions. With this in mind, E_2 and E_3 were estimated by comparing calculated and experimental CO and CO_2 profiles as well as mass consumption profiles for a number of carbon materials (Table 4.4). Many of the experimental data were taken from literature, but compar-

isons of the isothermal reactivity experiments of graphite and diesel soot performed in this study, with the results of the numerical model are shown in Figures 4.15 and 4.16. The kinetic parameters with which the profiles in Figures 4.15-4.21 were simulated are summarised in Figure 4.22. Adsorption parameters were not adjusted and kept equal for all cases (E_1=5 m^3/mol/s, A_1=45 kJ/mol). Note that the values of the kinetic parameters for steps R2 and R3 of diesel soot oxidation by O_2 used in this section have slightly different values from those used in the rest of the manuscript (E_2 and E_3 differ by less than 4% from the usual values). This is due to the use of the pore evolution model in this section. This model has not been used in the rest of the manuscript. Overall agreement is deemed to be quite good, especially for the oxidation of graphite. This comes as no surprise, as graphite is a high-purity carbon. The mechanism, which does not take into account interference by content such as hydrogen, oxygen and mineral matter, is predictably most suited for the simulation of high-purity carbons.

Another experiment with graphite from the literature is reproduced in Figure 4.17 and oxidation data of carbon black, which is also a very pure carbon material, is shown in Figure 4.18. In Figure 4.19, the model is shown to be capable of predicting TPO experiments of coke. Although CO_2 concentration is overestimated somewhat at 10 °C/min; this could most likely be dampened by adjusting reaction orders. Fits for char and flame soot oxidation are shown in Figures 4.20 and 4.21.

The model accurately predicts CO/CO_2 ratios for the examined materials. This required an extensive screening of literature to find carbon oxidation data containing both CO and CO_2 concentrations. Following the study of the oxidation of miscellaneous carbons, semiglobal activation energies E_2 and E_3 and the corresponding pre-exponential factors A_2 and A_3, obtained by optimisation, are plotted in Figure 4.22. Activation energies for both CO and CO_2 production steps increase with the carbon's C content (Figure 4.22a), which is to be expected, if C content is taken to be a measure of the degree of crystallinity of the carbon. For all studied carbons, $E_2 > E_3$, as found by Hurt and Calo [38] for a similar kinetic mechanism. The "effective activation energy" for the CO/CO_2 ratio, $E = E_{CO}$-$E_{CO_2} = E_2$-E_3, is compatible with the material-specific ranges found by Li and Brown [174]. Some

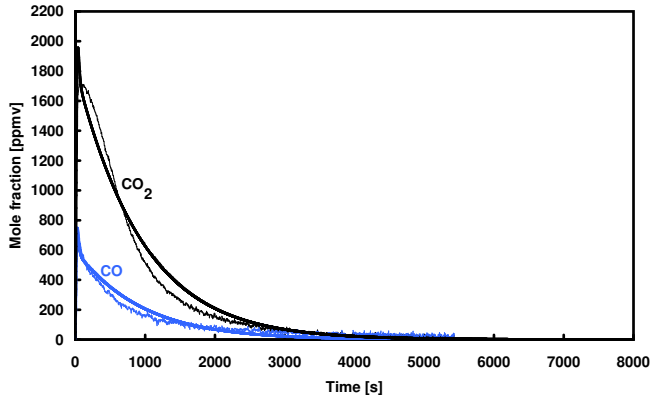

(a) IO of graphite at 813 °C, $\psi = 0$

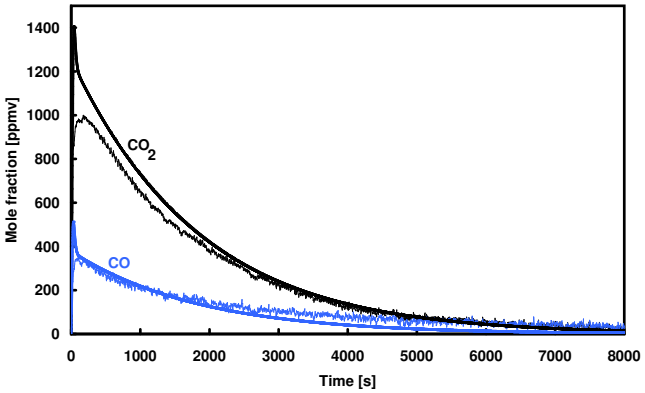

(b) IO of graphite at 773 °C, $\psi = 0$

Figure 4.15: Comparison of measured and calculated CO and CO_2 mole fraction profiles during IO of graphite with 10 % O_2. Thick lines represent simulations and thin lines experiments.

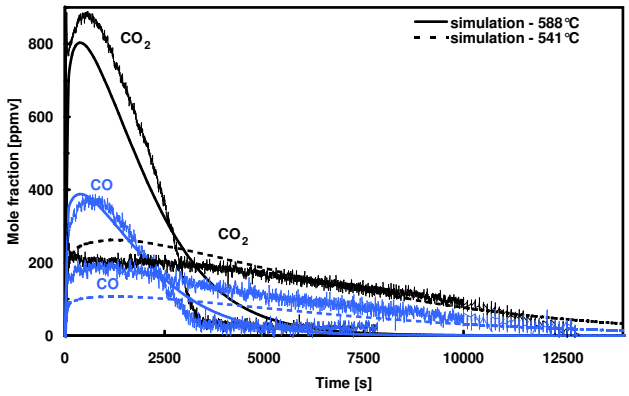

(a) IOs of diesel soot, $\psi = 5$

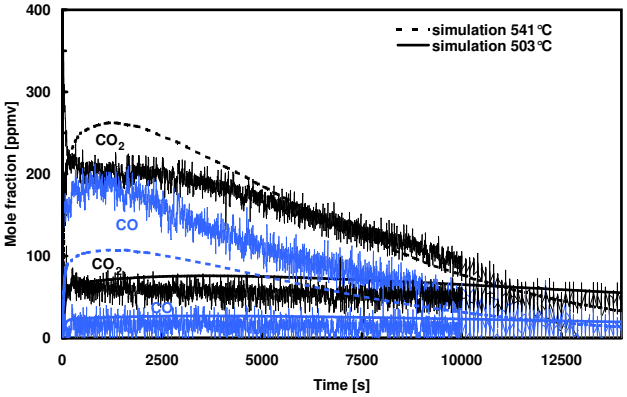

(b) IOs of diesel soot, $\psi = 5$

Figure 4.16: Comparison of measured and calculated CO and CO_2 mole fraction profiles during IO of diesel soot with 10 % O_2 at 588, 541 and 503 °C. Thick lines represent simulations and thin lines experiments.

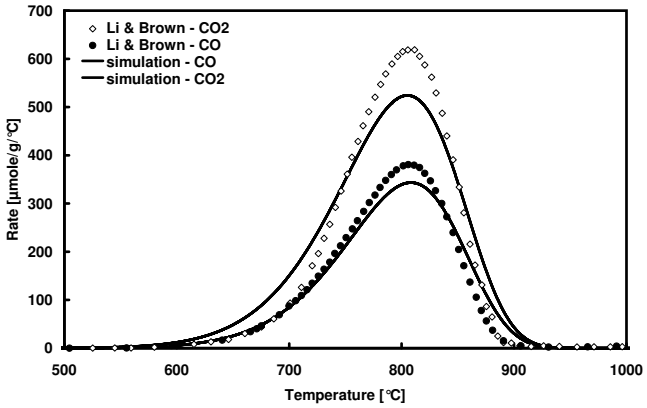

Figure 4.17: Measured [174] and calculated ($\psi = 0$) CO and CO_2 production rates during TPO of graphite with 0.939% O_2

scattering is found in the absolute values of A and E when reviewing different cases of carbon oxidation in literature, which can probably be attributed to the nature of the carbon [164, 170, 178, 179]. As can be seen in Figure 4.22a, E increases with C content in a roughly linear fashion, predicting an increasing overlap between CO and CO_2 peaks for more graphitised materials, which is confirmed by inspection of TPO profiles [174].

The behaviour of the natural logarithm of A, obtained by calibrating our semi-global model with different carbons, is shown in Figure 4.22b. In some studies [156, 55, 56], a negative slope was found for the correlation with parent coal C content in oxidation [55] and a positive slope for steam gasification [56]. However, swelling and devolatilisation effects would have to be taken into account before extrapolating these results to the derived char; it is therefore not necessarily surprising that the slope found in the present study is positive in the greater part of the range. It is to be expected that a correlation based on activation energies results in a clearer fit, as effects of many factors, such as choice of the pore structure parameter ψ, of the reaction order n, and of the different experimental conditions, are included in the pre-exponential factors. Obviously, the uncertainty in the determination of C content is also reflected in both these correlations. Overall, an increase of A_2 and A_3 is observed for more graphitised carbons. The curvature observed for both $ln(A_2)$ and $ln(A_3)$ however, makes a quadratic fit a better choice than a linear fit.

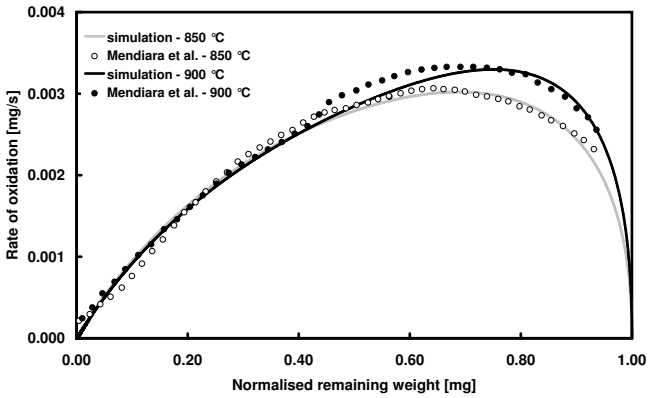

(a) Comparison of measured [133] and calculated ($\psi = 0$) oxidation rate

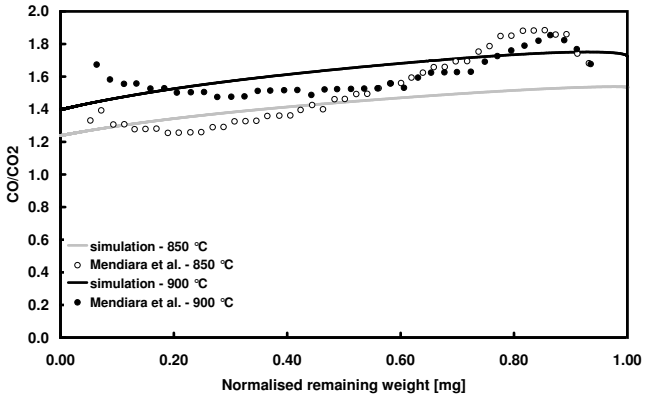

(b) Comparison of measured [133] and calculated ($\psi = 0$) CO/CO_2 ratio

Figure 4.18: IOs of carbon black with 500 ppm O_2 at 850 and 900 °C.

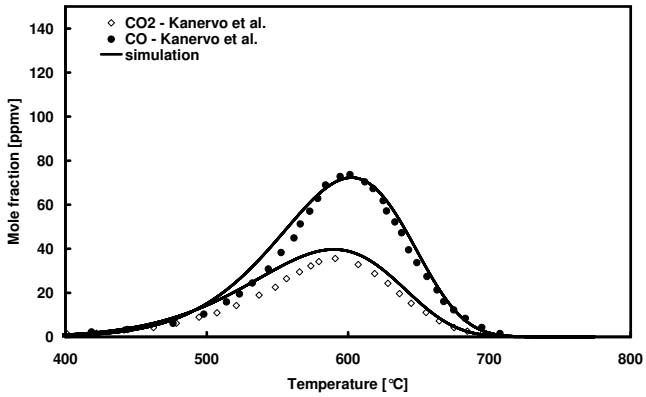

(a) TPO of coke with 2% O_2 at 5 K/min

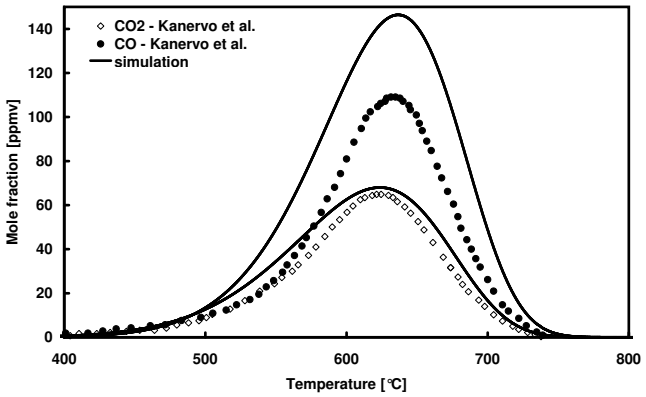

(b) TPO of coke with 2% O_2 at 10 K/min

Figure 4.19: Comparison of measured [97] and calculated ($\psi = 0$) CO and CO_2 mole fraction profiles

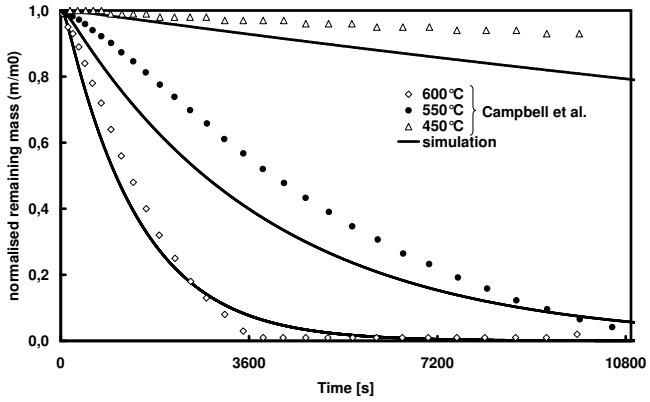

(a) Normalised remaining carbon mass

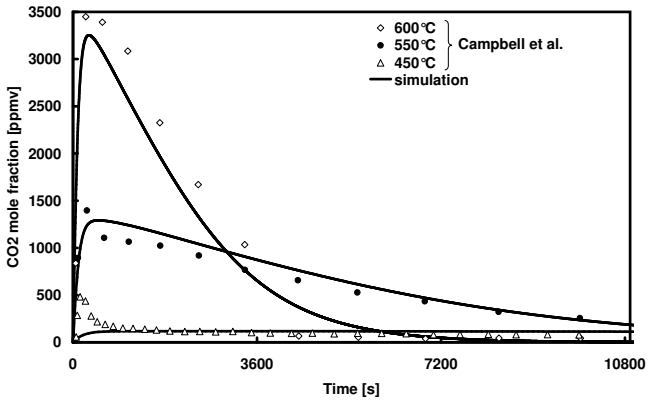

(b) CO_2 mole fraction

Figure 4.20: Comparison of measured [42] and calculated ($\psi = 2$) profiles during IO of char with 6% O_2

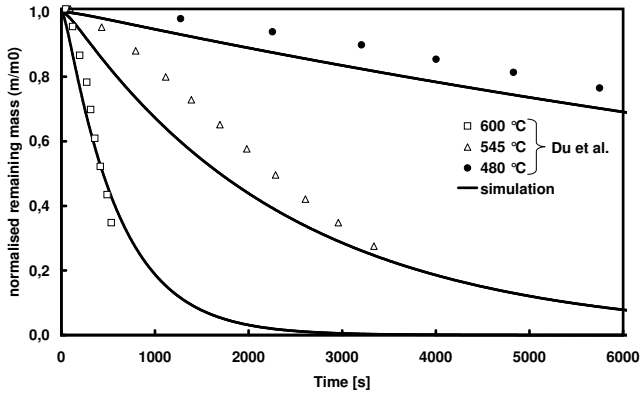

(a) Normalised remaining carbon mass

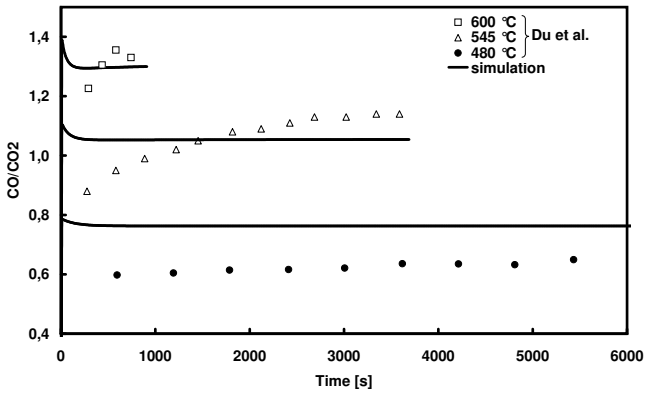

(b) CO/CO_2 ratio

Figure 4.21: Comparison of measured [173] and calculated ($\psi = 0$) profiles during IOs of ethylene soot with 21% O_2

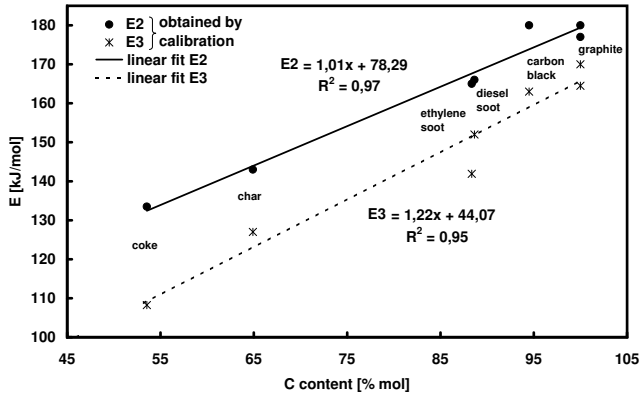

(a) Activation energies of different carbons

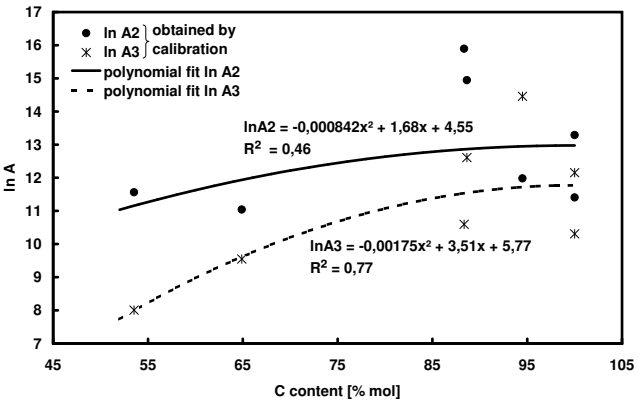

(b) Pre-exponential factors of different carbons

Figure 4.22: Kinetic parameters for a range of carbons. In both figures, points represent optimised values of the parameters for data from literature [174, 42, 97, 173] and the experiments performed in this study. The lines are fits.

Sensitivity analyses were performed for a range of carbons under various operating conditions. An example is shown in Figure 4.23. The normalised sensitivity coefficients of peak concentrations as well as concentrations at 30 and 60% of carbon conversion are not surprising. As expected, the adsorption step R1 has not much influence, with a maximum of 0.4 in Figure 4.23d. Further, CO concentrations are sensitive to the CO formation step, R2, and CO_2 concentrations to the CO_2 formation step, R3. Only in the final stages of the reaction (conversion=90%) do the concentrations become more sensitive to the competing reactions, i.e., CO to R3

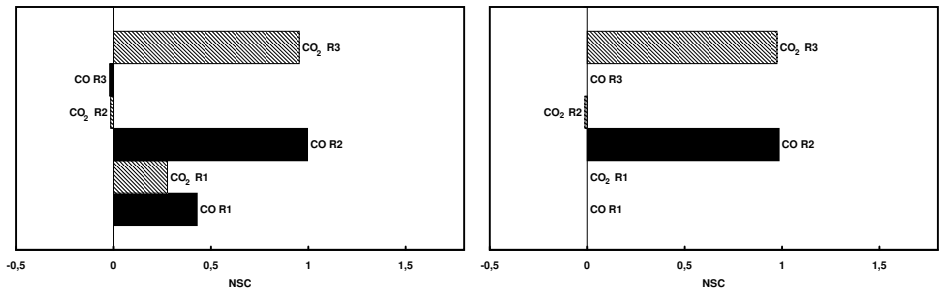

(a) Sensitivity coefficients of peak mole fractions

(b) Sensitivity coefficients of mole fractions at 30% conversion

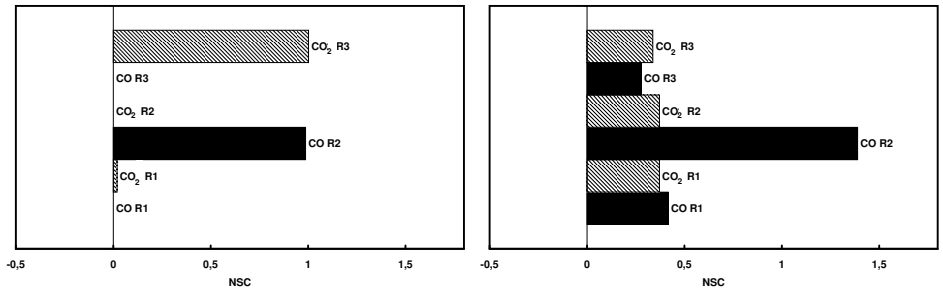

(c) Sensitivity coefficients of mole fractions at 60% conversion

(d) Sensitivity coefficients of mole fractions at 90% conversion

Figure 4.23: Normalised sensitivity coefficients ($s_{j,i}$) of CO and CO_2 mole fractions during IO of graphite (773 K, 10% O_2)

and CO_2 to R2. This presumably reflects the intensified competition for C* sites as progressively fewer of these sites are available. In fact, at an advanced stage of reaction, the rates r_2 and r_3 can be shown analytically to be dependent on k_3 and k_2 respectively, whereas the same is not true at low reaction progress ($t \approx 0$ s). In a similar manner, R1, or adsorption, also becomes more important as availability of C* decreases. CO and CO_2 peak concentrations (Figure 4.23a) are also fairly sensitive to the adsorption step R1 in this isothermal case, with $s_{CO,R1}$=0.43. However, although for profiles in TPO (e.g. Figure 4.19), peak concentrations are not strongly affected ($s_{CO,R1}$=-0.07), the location of CO and CO_2 peaks was shown to be quite sensitive to adsorption.

Using the relationships in Figure 4.22 to calculate material-specific kinetic parameters, the proposed model takes into account the nature of the carbon. Resulting

simulations are shown in Figure 4.24. As can be seen in Figure 4.24a, the quadratic dependency of the lnA has an interesting effect on the predicted CO/CO_2 ratio. Product concentrations exhibit non monotonic behaviour with a maximum or minimum at a certain degree of structural order of the carbon (ca. 80% C). The model also anticipates a shift in temperature of highest CO and CO_2 production, due to the increasing activation energies. With the proposed model, some insight into the state of the reactive carbon surface during oxidation can be gained (Figure 4.24b). Formation of C(O) does not vary, as adsorption of O_2 onto the C surface was chosen to be described independently of carbon nature. In the zone of product formation (400-800°C), all carbon sites have already reacted and nearly the whole surface is therefore covered by the intermediate complex C(O). Reaction of C(O) to form gaseous products starts earlier with less graphitised carbons. Difference in global reactivity is therefore seen as a difference in reactivity of the C(O) complex in this semi-global model, a view which has some physical significance. In fact, the type of surface complex formed, differs according to the carbon concerned, an occurrence which is sometimes described by one single complex C(O) possessing a distribution of activation energies [41, 4, 42].

It is well established that reactivity depends on carbon structure. For example, Radovic et al. [160] and Laine et al. [170] correlate severity of heat treatment and carbon nature with ASA and with a global rate constant. Elemental composition is also correlated with reactivity. For instance, Niksa et al. and Hurt [55, 56, 180, 156] correlate semi-global pre-exponential factors of char combustion and gasification with carbon content of the parent fuel. Hurt [180, 156] proposes the idea of using H/C or O/C ratios to model differing char reactivities. Some studies correlate carbon content and reactivity [181, 182]. Similarly, it is known that chars exhibit increasing reactivity with CO_2 with decreasing rank of parent coal [183]. The present study considers carbon reactivity to be constant throughout the course of the oxidation, but it is known that thermal annealing (densification of the carbon structure and loss of H atoms) leads to a decrease in reactivity [184]. Predictive tools of this process already exist. For instance, Senneca et al. [185, 186] present a kinetic submodel in which active sites become annealed sites according to the Arrhenius law. The concept developed in this study could be further developed by representing thermal

annealing with carbon hydrogen or carbon content as an indicator. Other authors define reactivity indices such as critical temperature value or the char burning rate at a standard reference temperature and find an empirical correlation between these and the parent fuel's C content [187, 180, 188, 189, 190]. Chan et al. [181] find that intrinsic reactivity of coal chars overall decreases with parent fuel carbon content, but no attempt was made to establish an analytical correlation. Specific surface area and porosity have also been found to correlate negatively with parent fuel carbon content [188, 191, 180]. Global activation energies are known to depend on structural order [147, 192]. The increasing activation energies in Figure 4.22a are representative of progressively more graphitised materials. High C content is used here to distinguish more crystalline materials. This somewhat simplified representation may be justified in the context of lumped, semi-global descriptions. Carbon content has certainly been shown to be an easily obtainable input parameter for a model capable of predicting oxidative behaviour of a wide range of carbons.

4.8 Conclusions

Mechanistic parameters for the oxidation of soot by O_2, NO, NO_2 and NO + O_2 were estimated by fitting calculated to measured NO, NO_2, N_2, CO and CO_2 concentrations. The mechanism contains five lumped surface species and thirteen reaction steps. It allows major trends of soot oxidation, such as NO, NO_2, N_2, CO and CO_2 selectivity and global reaction rates to be predicted. The principal shortcoming is its underestimation of low temperature CO formation under NO and NO_2; it shows that even in a lumped-species model, at least two CO-forming surface species are required. On exposure of soot to NO_2, NO is produced immediately because the lumped surface species C*(NO_2) is not stable. Below 600 °C, the reaction with NO_2 is controlled by the formation of the C*(ONO_2) complex, and above 600 °C NO_2 adsorption/desorption becomes rate determining. Under NO however, the oxidation of soot is limited by the NO adsorption/desorption steps at all temperatures; it is for this reason that it is less reactive than NO_2. The oxidation of soot by NO is enhanced by the addition of O_2 because the increased number of C*(O) on the surface affects the competition for C*(NO): it preferentially reacts with C*(O), eventually forming

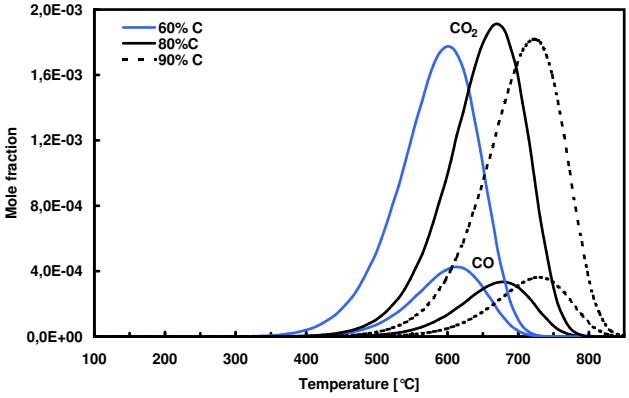

(a) CO and CO_2 mole fractions

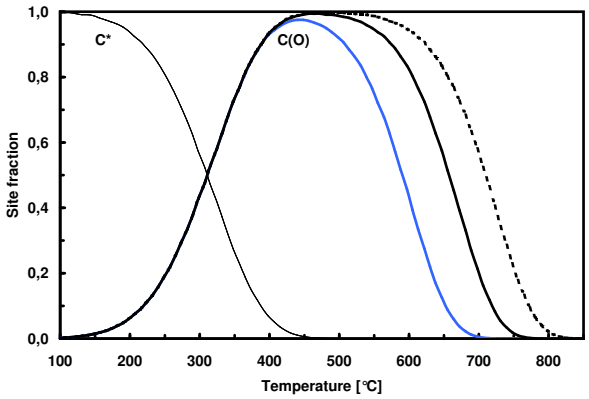

(b) Evolution of active carbon sites and surface oxygen complexes

Figure 4.24: Model predictions for TPO of different materials using C content as input. TPO at 10 K/min, 10% O_2, flow rate=250 sccarbon material, p_{atm}.

$C^*(ONO_2)$, but in lack of $C^*(O)$ the prevailing step is the splitting of $C^*(NO)$ into $C^*(O)$ and $C^*(N)$. Consequently the latter goes on to form N_2 in significant quantities only under NO, but not when O_2 or NO_2 are present. Experiments with soot and graphite show that BET surface area impacts on CO and CO_2 formation, but not on NO chemisorption. These unalike effects can be modelled by applying different CO and CO_2 formation parameters, but, with the current model formulation, not by using different reactive surface areas.

Different kinetic parameters for the oxidation of different types of carbons by O_2 were also estimated. The model is capable of describing traits of oxidation, such as CO-CO_2 selectivity and global reactivity (temperature shift in TPO), depending on the nature of the carbon, despite the widely differing crystallinities and surface chemistry of the materials. This material-specific behaviour is reproduced by characterising each carbon in terms of routinely available elemental carbon content. The values of k_j for each material enclose intrinsic reactivity effects due to the degree of crystallinity, as well as information on the surface chemistry (RSA/TSA ratio). Despite its simplicity, it is able to predict the differing reactivities and CO/CO_2 ratios of diverse carbon materials over a range of different temperatures and temperature ramps due to the behaviour of the surface complex C(O). The results suggest that increasing activation energies can be used to model carbons with an increasing carbon content.

Chapter 5

Interaction of Platinum/Ceria-Zirconia Catalysts With O_2, NO and NO_2

Abstract

Dans ce chapitre on analyse la cinétique de l'oxydation et du stockage des NO_x sur Pt/Al_2O_3, $Ce_xZr_{1-x}O_2$ et Pt/CeO_2. Un schéma detaillé impliquant des intermédiaires de surface tels les nitrites et nitrates a été proposé pour décrire l'interaction entre NO, O_2 et la cérine zircone. Les paramètres correspondants ont été évalués par comparaison avec des expériences d'oxydation, adsorption et desorption issues de la littérature récente. Des tendances importantes du comportement des cérine zircones ($x = 0 - 0.84$), du platine et de Pt/CeO_2 ont été reproduites avec succès dans une large gamme de températures. Il est confirmé que la teneur en zirconium réduit la capacité d'oxydation de NO. Le stockage des NO_x est décrit par l'accumulation de nitrates sur la surface de l'oxyde ($Ce_xZr_{1-x}O_2$). Les processus d'oxydation et de stockage sur Pt/CeO_2 peuvent dans certains cas être simulés en utilisant les paramètres evalués séparément pour Pt et Ce. Bien que l'oxydation soit surtout affectée par Pt, des nitrates sont stockés sur CeO_2, et ce stockage est plus efficace dans le cas de mélanges $NO+O_2$ que sous NO_2. À nombre de sites actifs identique, le stockage de NO_x sur Pt/CeO_2 est moins efficace que sur $Pt/BaO/Al_2O_3$.

⋆

The kinetics of NO_x oxidation and storage were studied over Pt/Al_2O_3, $Ce_xZr_{1-x}O_2$ and Pt/CeO_2. A detailed kinetic mechanism involving lumped nitrate and nitrite species was proposed for the interaction of NO_x and O_2 with ceria(-zirconia) and its parameters estimated using oxidation and adsorption/desorption experiments. Important trends in the behaviour of ceria-zirconia catalysts ($x = 0 - 0.84$), platinum and Pt/CeO_2 were reproduced over a wide range of temperatures. Thus zirconium affects redox behaviour of the oxide, ultimately decreasing its ability to oxidise NO to NO_2. NO_x storage is described via the accumulation of nitrates on the oxide surface. In some cases oxidation and storage over Pt/CeO_2 can be reproduced by fitting ceria and platinum-related parameters separately. While oxidation behaviour is mainly dictated by Pt, nitrate storage occurs on CeO_2 and is shown to be more efficient under a $NO+O_2$ flow than NO_2. However when considering an equal number of active sites, Pt/CeO_2 stores NO_x less efficiently than $Pt/BaO/Al_2O_3$.

5.1 Background

The oxidation of NO to NO_2 is crucial in a number of exhaust gas treatment processes. These include NO_x removal with LNTs [193] and the oxidation of soot in catalysed diesel particulate filters (DPFs) [1, 43]. The NO_x storage-reduction (NSR) catalysts used in LNTs typically contain noble metals for NO_x oxidation and reduction and alkali/alkali earth metal compounds for NO_x storage [193]. The use of CeO_2 and CeO_2-ZrO_2 mixed oxides as either storage component or support is common in DPFs [43, 194, 195, 196], LNTs [197, 195, 196] and in three-way catalysts because of the oxides' oxygen storage capacity [71]. These applications mostly see ceria(-zirconia) as a part of composite catalyst formulations and few articles investigate the NSR behaviour of these oxides on their own. The NO_x trapping performance of the storage component is generally assumed to occur in the form of sorbed ni-

trites or nitrates on its basic adsorption sites [193]. The common NSR catalyst $Pt/BaO/Al_2O_3$ is known to adsorb NO_2 more efficiently than NO [87, 198] and in this case the oxidation of NO to NO_2 prior to the storage phase is a definite advantage. While with $Pt/BaO/Al_2O_3$, NO oxidation takes place mainly over Pt, CeO_2 has been shown to be an "active" support, capable of acting as an oxidation catalyst itself [199]. Dispersed Pt particles on ceria-zirconia are known to resist ageing better than the common $Pt/BaO/Al_2O_3$ [200]. Most studies employ complex gas flows; few investigate the role and especially the kinetics of NO_x oxidation/storage in simpler systems such as Pt/CeO_2 and Pt/CeO_2-ZrO_2 under $O_2/NO/NO_2$ streams [201, 199]. Although many data obtained by first principles calculations [202, 203, 204] help understand the reaction mechanism, most of these cannot be directly employed in mean-field kinetic models because they are sensitive to the structure of the crystal lattice and site heterogeneity in general, and these aspects are not taken into account in our kinetic approach. Overall, the role of ceria in NSR remains controversial [193]. While some studies [205, 206] demonstrate that NO_x storage benefits from the addition of ceria to Ba-based NSR catalysts, others [207] observe no noticeable effect. In order to fully understand the complex mechanism of exhaust gas catalysis, it is appropriate to study all the involved phenomena separately. Therefore the present paper deals with NO/O_2 and NO_2 gas feeds only. Parameters pertaining to these different experimental gas feeds are determined separately. These values are determined by fitting model equations to data of temperature-programmed experiments, a technique which is well known [62, 208]. Based on data from literature, this study aims to elucidate the kinetics of NO oxidation in a simple gas flow over CeO_2 and CeO_2-ZrO_2, and model the main NO_x-oxidation-storage trends over a Pt/CeO_2-ZrO_2 NSR catalyst.

5.2 Surface Chemistry Model

Minor species such as N_2 and N_2O were not included in the mechanism. Apart from the two Ce-O surface species, the mechanism involves two kinds of Ce-N and Pt-N as well as one Pt-O surface species, all of which are lumped representations of intermediates which may be observed experimentally.

Table 5.1: Surface reaction mechanism of the interaction of NO_x and O_2 with ceria and platinum

Reactions on support
R11: 2 Ce + O_2 → 2 Ce-O
R12: 2 Ce-O → 2 Ce + O_2
R13: Ce + NO_2 → Ce-NO_2
R14: Ce-NO_2 → Ce + NO_2
R15: Ce-NO_2 → Ce-O + NO
R16: Ce-O + NO → Ce-NO_2
R17: Ce-NO_2 + Ce-O → Ce-NO_3 + Ce
R18: Ce + Ce-NO_3 → Ce-NO_2 + Ce-O
Reactions on platinum
R19: 2 Pt + O_2 → 2 Pt-O
R20: 2 Pt-O → 2 Pt + O_2
R21: Pt + NO → Pt-NO
R22: Pt-NO → Pt + NO
R23: Pt-NO + Pt-O → Pt-NO_2 + Pt
R24: Pt-NO_2 + Pt → Pt-NO + Pt-O
R25: Pt + NO_2 → Pt-NO_2
R26: Pt-NO_2 → Pt + NO_2

Reactions R11 - R18 are elementary steps proposed to describe the global reaction $2NO + O_2 \rightleftharpoons 2\,NO_2$. Pre-exponential factors are given in the compatible units (using cm, mol and s), making it possible to readily implement the scheme in the Chemkin code [111] too. The mechanism for CeO_2 (Reactions R11 - R18) was proposed and optimised as explained in Section 5.3. A choice was made to employ the same surface mechanism to describe the behaviour of both CeO_2 and a range of CeO_2-ZrO_2 mixed oxides ($Ce_xZr_{1-x}O_2$). Since the reducibility of $Ce_xZr_{1-x}O_2$ is strongly dependent on the Zr content of the material [209, 210], the kinetic parameters of R12 were adjusted to reproduce differing NO oxidation activity of $Ce_xZr_{1-x}O_2$. The mechanism involving Pt (Reactions R19-R26) was proposed in a previous study [87]. Kinetic parameters have however been optimised during the course of the present study. The current approach also differs from the previous study in that kinetic backward constants are fitted to experimental data at high temperature to ensure the reaction reaches equilibrium consistently with thermodynamics.

5.3 Kinetics of NO Oxidation and Storage over CeO_2

Experiments simulated in Sections 5.3, 5.4 and 5.5 are listed in Table 5.2. The parameters obtained by calibration of the model or taken from literature are given in Table 5.3. Generally speaking, models in automotive catalysis are only reliable for the exact catalyst on which they have been tested [211]. Therefore our aim was to identify lumped reaction intermediates and reaction steps which are characteristic of the class of $Ce_xZr_{1-x}O_2$ catalysts as a whole. These features should not be dependent on the precise conditions of synthesis and storage of the catalyst before the experiment. For instance, the lumped species Ce-NO_2, Ce-NO_3, Ce and Ce-O were proposed because an extensive survey of the relevant literature showed that surface nitrates and nitrites, Ce^{4+} and Ce^{3+} and their interactions have been identified in measurements from several different sources. Since ceria catalysts are very complex, these species do not represent actual physically measurable species, but rather enclose a number of such measurable species. We tried to minimise the possibility of non-unique sets of values by fitting the same parameters with several

Table 5.2: Experiments used for model validation

Catalyst	x_{NO}	x_{O2}	Temperature	Figure	Type	Ref
$Ce_{1.0}Zr_{0.0}O_2$	0	10^{-3}; 10^{-5}	1200 °C; 1725 °C	n/a[d]	n/a	[212][a]
$Ce_xZr_{1-x}O_2$[b]	0.0005	0.05	10°C/min	5.1,5.4	TPO	[82]
$Ce_xZr_{1-x}O_2$[c]	0	0	10°C/min	5.2,5.6	TPD[e]	[82]
7.7 wt % Pt/Al_2O_3	0	0	40°C/min	5.7	TPD[f]	[86]
2.3 wt % Pt/Al_2O_3	0.0006	0.08	5°C/min	5.8	TPO	[86]

[a] The model was compatible with the phase diagram in [212]
[b] Values of x were 1, 0.76, 0.56, 0.36 and 0.16
[c] Values of x were 1 and 0.76
[d] Not applicable
[e] After adsorption of 200 ppm NO + 5% O_2 at 350 °C
[f] After adsorption of 2% O_2 at 400 °C

experimental profiles. For ceria, thirteen parameters were estimated by fitting to three experimental curves and the overall thermodynamic NO-O_2 equilibrium had to be respected. In addition, a qualitative criterion was for the appearance of surface species to correspond to temperature ranges known from literature. Once the parameters had been estimated, the parameter correlation matrix was evaluated, and the majority of correlation coefficients are smaller than 0.7. Notably, A and E_a for a given reaction are not highly correlated, whereas all the α_θ (dependence of E_a on coverage)) are more than 70% correlated with other parameters. A7-E7 and A8-E8 correlation coefficients are however significant, which comes as no surprise because these are surface reactions, with no measured concentration directly used in fitting.

In this section, the values obtained during calibration of the mechanism R11-R18 for the catalytic behaviour of CeO_2 are presented and discussed with reference to the current literature. When treated in a reducing atmosphere at high temperatures, CeO_2 is known to form a continuum of oxygen deficient, non-stoichiometric CeO_{2-x} oxides ($0 < x \leq 0.5$) [209]. The couple Ce^{3+}-Ce^{4+} exhibits redox behaviour [71], but at room temperature and high partial pressures of oxygen ($> 10^{-5}$ bar) the affinity of ceria for oxygen is considerable [212]. Oxygen vacancies are thus filled by oxygen from the gas-phase [71, 213] and ceria is quasi exclusively present as fully oxidised CeO_2. This ready oxidation behaviour has been represented through reactions R11 and R12 by calibrating A_{12}. It is here seen as the only interaction of ceria with O_2

Table 5.3: Parameters for the surface reaction mechanism

CeO_2	A_j **[cm,s,mol] or** $S_{0,j}$	E_j **[kJ/mol]**	**Ref**
R11	0.75	0.00	[214]
R12	5.00× 10^{12}	100	[214, 212]
R13	1.00× 10^{-4}	0	ts[a]
R14	2.00× 10^{12}	175	ts
R15	5.00× 10^{16}	158-190 θ_{Ce-NO_2}+80 $\theta_{Ce^{4+}-O}$	ts
R16	1.00× 10^{-8}	0	ts
R17	1.00× 10^{14}	87	ts
R18	1.00× 10^{15}	50	ts
Pt	A_j **[cm,s,mol] or** $S_{0,j}$	E_j **[kJ/mol]**	**Ref**
R19	0.03	0	[86]
R20	4.00× 10^{27}	232-35 θ_{Pt-O}	ts
R21	0.85	0	[86]
R22	5.00× 10^{15}	130	ts
R23	1.00× 10^{21}	115	ts
R24	7.00× 10^{17}	70	ts
R25	0.97	0	[86]
R26	7.00× 10^{11}	88	ts

[a] this study

and therefore encloses the effects of adsorbed surface species such as peroxides and superoxides [71]. $S_{0,11}$ and E_{12} were kept constant at the values given in [214] and E_{12} was compatible with the enthalpy values given in [215, 216] (see Section 5.4). The resulting value of A_{12} was used for all operating conditions, extrapolating its validity to partial pressures of O_2 higher than 10^{-3} bar. Note that atomic O/Ce ratios were within 3% of the experimental values [212] at 1200 and 1725 °C at pressures of 10^{-3} and 10^{-5} bar.

Atribak et al. [82] published results from a 10°C/min temperature-programmed oxidation (TPO) experiment of ceria in presence of 500 ppm NO + 5% O_2 and a gas flow rate of 500 N cm^3/min. The same publication also contains data from a temperature-programmed desorption (TPD) experiment under an inert gas at 10°C/min, starting from 350°C. The TPDs were preceded by an adsorption phase under 200 ppm NO + 5% O_2 at 350 °C. Both experiments were simulated using the surface area of 64

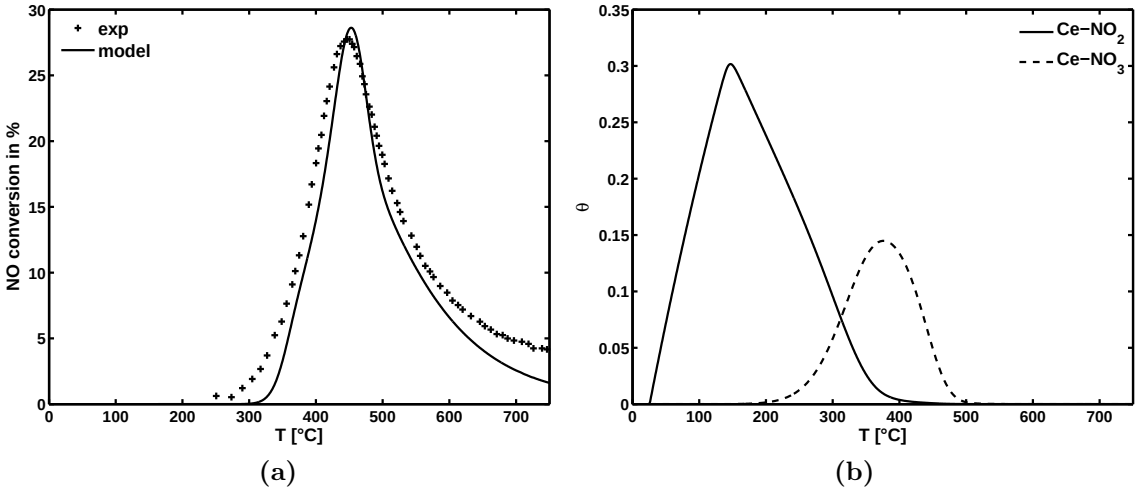

Figure 5.1: Predictions of NO_x content, NRMSD=8.80% (a) and surface intermediates (b) during TPO of CeO_2 in presence of NO and O_2. Experimental data from [82]

m^2 measured by Atribak et al. Maintaining the parameters already derived for R11 and R12, rate parameters for R13-R18 were calibrated by simulating these two experiments. Simulation results are shown in Figures 5.1 and 5.2 and the normalised root mean square deviation (NRMSD) for the fit is 8.80%. It is known that surface nitrites result from the interaction of NO and NO_2 with ceria [209, 82], as described by R13 and R16. These reactions are in agreement with DFT studies [203, 204]. In accordance with the finding from DRIFTS data that the main pathway leading to surface nitrates is the surface oxidation of nitrites [82], the couple R17-R18 was proposed. Nitrites are readily converted into nitrates [82], resulting in the low value of E_{17}. Since ceria has been shown to adsorb little NO at room temperature [71], the very low value employed for the sticking coefficient $S_{0,16}$ seems reasonable. The dependence of NO oxidation on surface coverage by various ad-NO_x species [82] is here represented by the θ-dependent value of E_{15}.

Given the larger rate constant of nitrite production ($k_{13} > k_{17}$) at $T < 200$ °C, nitrites are initially formed, and transformed into nitrates starting from 200°C (Figure 5.1b). This is consistent with the fact, pointed out by Atribak et al., that nitrates are in general more stable than nitrites. The transformation is however reversed later

on, as nitrates are changed back into nitrites to subsequently form NO and NO_2. As can be seen later on (in Section 5.4, Figure 5.5), the typical twin-peaked NO profile of ceria [201] can be produced with the proposed model; this is also further discussed in Section 5.6 (Figure 5.9b).

Like during TPO, a nitrite peak is also formed during desorption at 350 °C (Figure 5.2b). The tendencies of NO and NO_2 desorption are fairly well reproduced in Figure 5.2a. Measured curves indicate an immediate production of NO_2 upon exposure, whereas NO formation becomes significant only a little later, at around 370 °C. This trend is reproduced by the mechanistic parameters in Table 5.3. An analysis of the simulated rates of production shows that this characteristic of TPD is achieved by an increased activity of R12 due to the absence of O_2. Simulations show significant production of O_2 by R12 during TPD, a behaviour which is confirmed by experimental observations [82]. Consequently, more Ce is formed, which in turn causes an immediate transformation of nitrates into nitrites (R18) and therefore NO_2 production (R14). The model overestimates NO_2 desorption somewhat between 360 and 400 °C, with the effect that NO formation is underestimated above 400 °C. DRIFTS spectra show that several ad-NO species, for e.g. hyponitrites, nitrites and bidentate nitrates, contribute to NO_x formation below 350 °C [217, 218]. In our mechanism, these are all represented by Ce-NO_2, the only NO_x-forming species. The parameters were fitted to optimise NO_2 formation in TPOs, but this meant compromising on the quality of the TPD fit. We presume that another intermediate species, reactive below 350 °C, would allow for a better fit of TPDs. For the simulations in Figure 5.2a, ad-NO_x species at the start of TPD are presumed to be those stable at 350 °C, which according to a simulation of the adsorption process correspond to θ_{Ce-NO_2}= 0.0005 and θ_{Ce-NO_3}= 0.0160. The desorption of these species yields NO_2 first and then NO at higher temperatures as $k_{14} > k_{15}$.

The surface nitrite, Ce-NO_2, is clearly an important intermediate species. It is involved directly in all reactions other than R11 and R12. The two products, NO and NO_2, are only produced directly from Ce-NO_2. There is thus a competition between R14, R15 and R17, who in parallel convert Ce-NO_2 into NO_2, NO and Ce-NO_3, respectively. An analysis of the normalised rates of Ce-NO_2 production/consumption

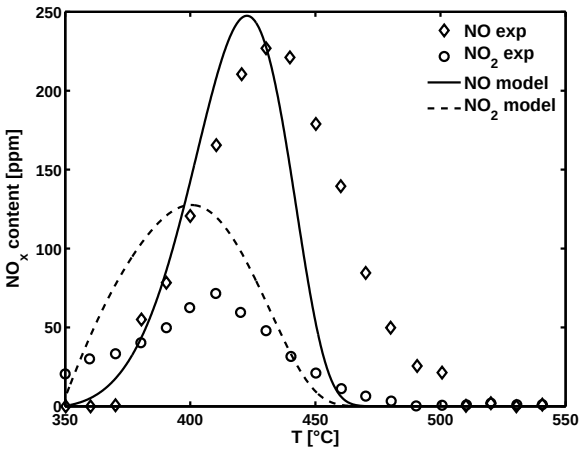

(a)

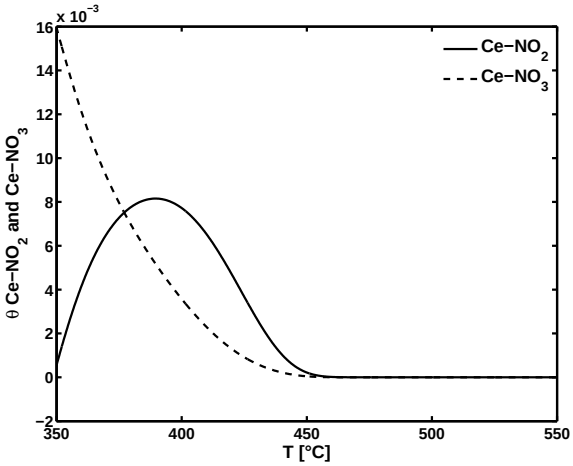

(b)

Figure 5.2: Predictions of NO_x content, $NRMSD_{NO}$=23.44%, $NRMSD_{NO_2}$=32.62% (a) and surface intermediates (b) during TPD of CeO_2 under an inert flow of gas. Experimental data from [82]

was performed in Atribak's TPO conditions under 500 ppm NO + 5% O_2; the results are shown in Figure 5.3a. This allows us to explain how the mechanism is able to reproduce certain particularities of CeO_2. Up to 110 °C, it is loaded with both nitrites and nitrates via R17 and R16. At 200 °C, a second nitrate storage phase (R17) begins, until R18 becomes more important due to a higher temperature (300 °C). Nitrates are then transformed back into nitrites. Above 300 °C then, the nitrites are left with only two parallel paths (R14 and R15). The importance of R14 reaches a peak at around 500 °C; up to this temperature R14 produces NO_2, but here thermodynamics takes over and R15 becomes dominant once again, in equilibrium with its reverse reaction R16. During the course of the experiment, R17 (nitrate formation) and then R14 (formation of NO_2) momentarily outcompete R15, this results in the two peaks of NO production often observed experimentally (see also Fig. 5.5). In Figure 5.3b, the analysis was extended to a hypothetical case with the same conditions as in Figure 5.3a, but using 500 ppm of NO_2 as reactive gas instead. In this case there is a single extended phase of nitrate storage (R17) until 300 °C and no formation of NO via R15 below 300 °C. As under NO + O_2, Ce-NO_2 is successively transformed, first into nitrates (R17) until 400 °C, then into NO_2 (R14) until 450 °C and finally into NO (R15). In conclusion, the major difference between the two cases can be seen firstly at low temperatures, under 300 °C, where an analysis of R11 and R12 indicates that their net rate produces Ce-O in the first case, but Ce in the second case. The absolute value of nitrate storage rate by R17 (r_{17}) then is significantly smaller than in the first case. Secondly, the shape of the rate of R17 is different in the two cases, and in particular the monotonically increasing rate in Fig. 5.3b prevents the formation of a second peak of NO. Overall, the model predicts better NO_x storage on ceria under NO + O_2, which is confirmed later on (Section 5.6). Furthermore, in this kinetic model the typical double-peak profile of NO over ceria results from a competition between R14, R15 and R17, all of which are fuelled by nitrites.

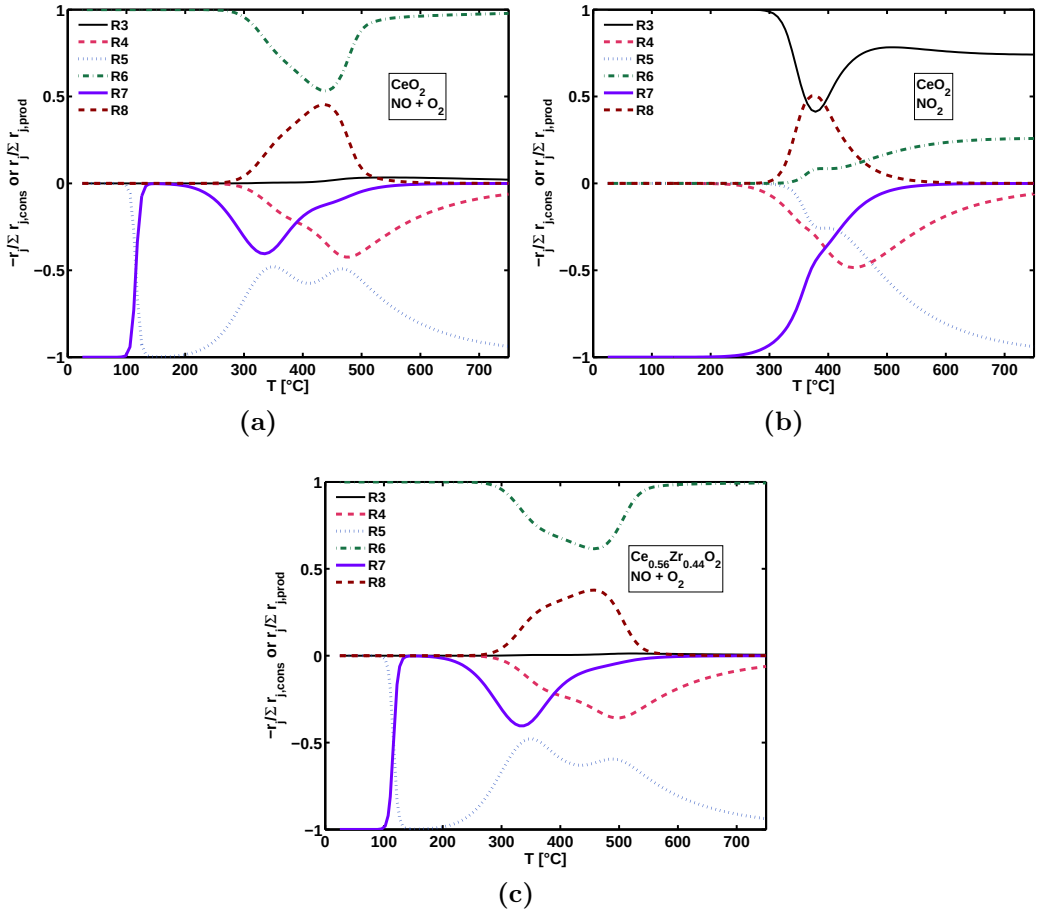

Figure 5.3: Normalised rates of production/consumption of Ce-NO_2 by R13-R18 during simulation of the TPO of a) CeO_2 with NO+O_2, b) CeO_2 with NO_2 and c) $Ce_{0.56}Zr_{0.44}O_2$ with NO+O_2.

Table 5.4: Kinetic Parameters for $Ce_xZr_{1-x}O_2$

% Zr	x	A_{12} [cm,s,mol]	E_{12} [kJ/mol]
0	1.00	5.00×10^{12}	100
24	0.76	4.00×10^{9}	62.5
44	0.56	2.00×10^{9}	62.5
64	0.36	5.00×10^{8}	62.5
84	0.16	2.00×10^{7}	62.5

5.4 Kinetics of NO Oxidation and Storage over $Ce_xZr_{1-x}O_2$

In this section, the results of a generalisation of the mechanism R11-R18, in order to employ it for the simulation of a series of ceria-zirconia mixed oxides, are presented. In accordance with the fact that the redox behaviour of $Ce_xZr_{1-x}O_2$ is dependent on Zr content, the kinetic parameters A_{12} and E_{12} were adjusted to reproduce differing behaviours in $Ce_xZr_{1-x}O_2$ (Figure 5.4). Whereas oxidation enthalpy does not seem to vary much amongst different ceria-zirconia oxides (on average $-\Delta H = 500$ kJ/mol O_2 for $0.14 < x < 0.81$), reduction of pure CeO_2 is comparatively difficult with approximately $-\Delta H$=800 kJ/mol O_2 [215, 216]. Since these values apply to the fluorite-structured crystalline oxides, they are divided by eight to obtain activation energies for the single site represented in reaction R12: E_{12}=100 kJ/mol O_2 for pure CeO_2, as already proposed in the literature [214] and E_{12}=62.5 kJ/mol O_2 for mixed oxides. In agreement with average oxidation entropies of the mixed oxides taken from Zhou et al. [215], the proposed values of A_{12} decrease exponentially with Zr content. These values are summarised in Table 5.4.

Since the present mechanism was shown to perform well over a wide range of operating conditions, we saw it fit to perform a parametric study of Zr content. Like pure ceria, mixed oxides are expected to adsorb NO and form Ce-NO_2 to then oxidise it to Ce-NO_3 with increasing temperature [219]. As already mentioned in Chapter 3, this study focuses on kinetics, while structural aspects are described in a global manner, by an active surface. All $Ce_xZr_{1-x}O_2$ were presumed to have the same surface area

and site density, a choice made on the consideration that BET surface area played a minor role in the NO oxidation experiments [82]. With progressively higher Zr content, A_{12} decreases and R13 becomes less efficient, ultimately leading to the loss in catalytic activity experimentally observed by Atribak et al. NO conversion peaks are adequately reproduced in Figure 5.4a with NRMSDs of 8.80%, 10.09%, 11.16% and 8.25% for 0, 24, 44 and 64 % Zr, respectively. At higher Zr contents, low temperature behaviour is predicted less accurately ($NRMSD_{84\%Zr}$=42.84 %), presumably because the type of nitrate formed on the $Ce_xZr_{1-x}O_2$ surface is also affected by Zr-doping. Azambre et al. [217] find that nitrates are more stable on Zr-rich oxides ($x \leq 0.5$). Implementation of such a less reactive nitrate (either by rendering R18 less efficient, or by actually adding another nitrate species), would allow us to shift the peak in Figure 5.4(a) to 500 °C as observed experimentally for $Ce_{0.16}Zr_{0.84}O_2$. It can be seen in Figure 5.4b, that although a change in Zr content has practically no effect on the evolution of surface nitrites, the nitrate storage phase is prolonged.

The impact of Zr content is further investigated by an analysis of normalised rates of production of Ce-NO_2. From Figure 5.3c it can be seen that the major difference between pure ceria (Fig. 5.3a) and a mixed oxide is the peak height/ shape of R18 and R14, which results in a higher second peak of NO production (R15); NO conversion is therefore less efficient as the experimental data in Figure 5.4 shows. The cause of this change in behaviour with addition of Zr is in fact the decrease of A_{12}, which leads to a diminished presence of Ce; this in turn affects R13 and R18. The latter's production of Ce-NO_2 consequently slows down as observed in Figure 5.3c. As a result, Ce-NO_3 is also consumed more slowly by R18, which explains the longer storage phase observed in Figure 5.4b. Atribak et al. also performed TPD for $Ce_{0.24}Zr_{0.76}O_2$. The directions of the changes are reproduced by the model (Figure 5.6), although the predicted extent of change is somewhat smaller. As for the TPD of pure CeO_2 (Figure 5.2, shown again for comparison in Figure 5.6), NO is overpredicted for 24% Zr (NRMSD=33.78%). NO_2 however is underpredicted (NRMSD=24.10%). This is even more marked for mixed oxides with more Zr, and as in the case of the NO-TPO over $Ce_{0.16}Zr_{0.84}O_2$, we can presume that Zr-doping affects nitrate stability and that this must necessarily be taken into account to correctly predict TPD behaviour for 84% Zr and above. In summary, simulations using the kinetic parameters derived

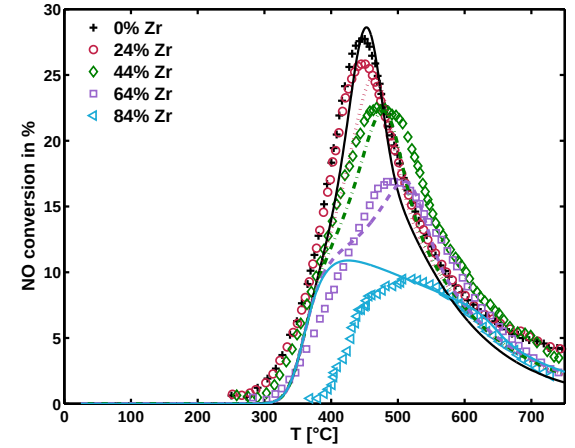

(a)

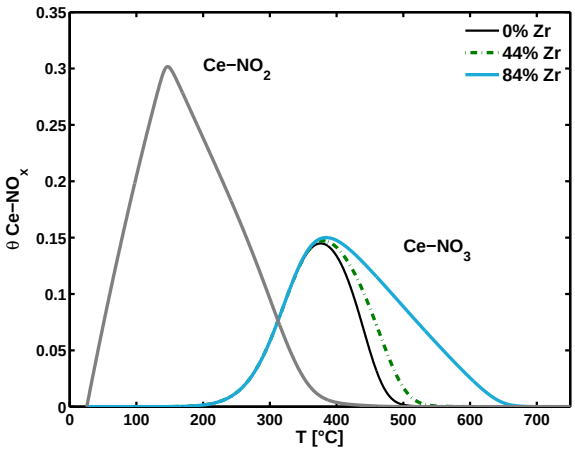

(b)

Figure 5.4: Simulated and experimental [82] values of NO conversion (a) and simulated evolution of surface intermediates (b) during TPO of $Ce_xZr_{1-x}O_2$ in presence of NO and O_2.

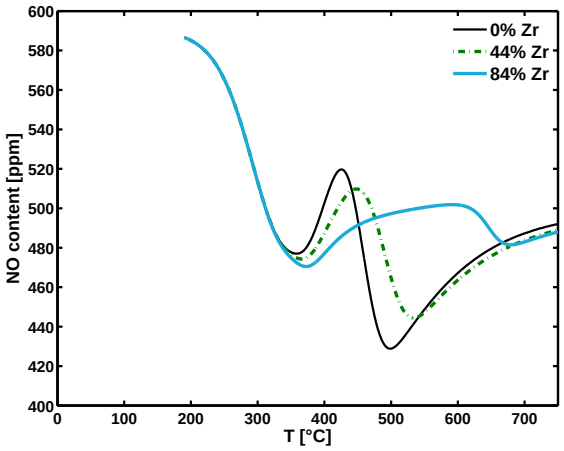

Figure 5.5: Predictions of NO content during TPO of $Ce_xZr_{1-x}O_2$ in presence of NO and O_2. Feed: 500 ppm NO + 5 % O_2.

during the course of this study are in agreement with catalytic experiments from disparate sources. The model is in particular capable of correctly predicting NO oxidation behaviour of various ceria-zirconia mixed oxides (%Zr $\leq$ 64%) over a range of temperatures and adsorption/TPD behaviour over CeO_2.

5.5 Kinetics of NO Oxidation over Pt/Al_2O_3

Details on the mechanism R19-R26 are provided in [87]. The updated parameters are shown in Table 5.3. The interaction of Pt with O_2 (R19-R20) was modelled on the TPD performed by Olsson et al. [86] and the resulting fit shown in Figure 5.7. O_2 evolution in the gaseous phase is adequately reproduced, as is the profile of surface oxygen modelled by the authors of the original article. R21-R26 were calibrated using the experimental NO and NO_2 values in Figure 5.8. Overall, the fit is reasonable, although the low-temperature reactivity is underestimated. Other studies also indicate that reactions R19-R26 allow for prediction of the overall trend, but are not sufficient to reproduce activity below 200 °C [220, 86]. Note that the Pt/Al_2O_3 surface displays a peak of Pt-NO between 150 and 250 °C, but NO_x storage on Pt remains negligible ($\theta_{Pt-NO_2} < 0.05$ between 0 and 500 °C) in comparison to ceria-zirconia.

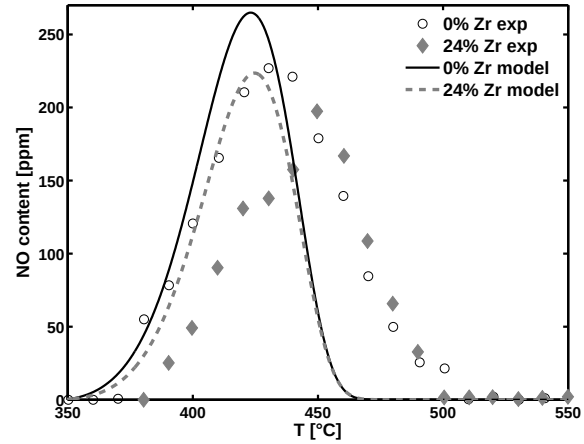

(a)

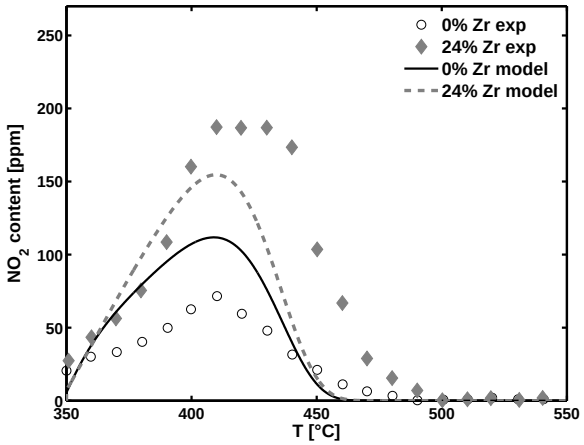

(b)

Figure 5.6: Predictions of NO_x content during TPD of $Ce_xZr_{1-x}O_2$ under an inert flow of gas. 24% Zr: $NRMSD_{NO}$=33.78%, $NRMSD_{NO_2}$=24.10%. Experimental data from [82].

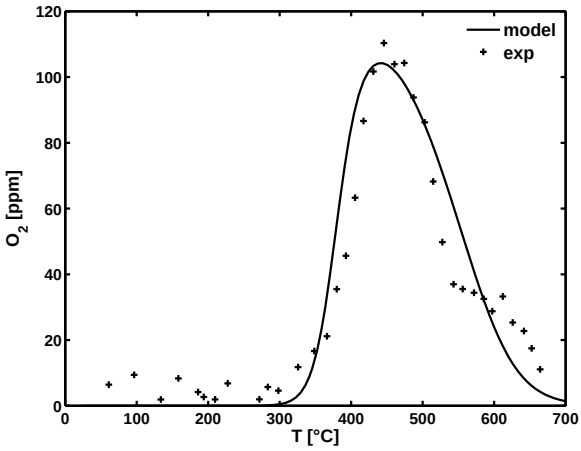

(a)

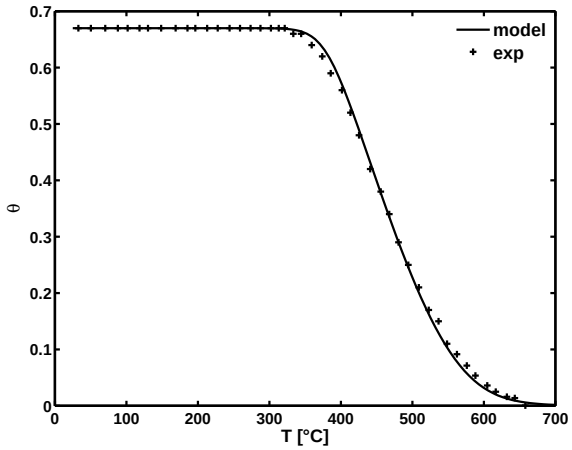

(b)

Figure 5.7: Predictions of O_2 content, NRMSD=10.88% (a) and surface intermediates (b) during TPD of platinum, NRMSD=1.20%. Experimental data from [86]

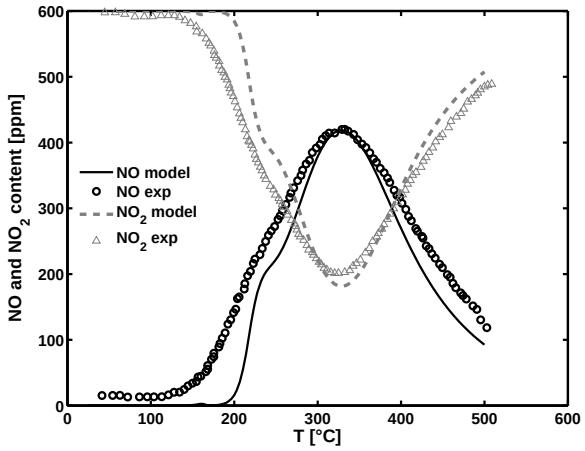

Figure 5.8: Predictions of NO_x evolution during TPO of platinum in presence of NO and O_2, $NRMSD_{NO}$=13.11%, $NRMSD_{NO_2}$=13.71%. Experimental data from [86].

5.6 NO Oxidation and Storage over Pt/CeO_2

The feasibility of coupling reaction mechanisms for CeO_2 (R11-R18) and Pt/Al_2O_3 (R19-R26) in order to simulate Pt/CeO_2 or $Pt/CeO_2/Al_2O_3$ was studied. To our knowledge, the only study which reports on the catalytic activity of Pt/CeO_2 for oxidation of NO in a gas flow containing NO and O_2 alone, is an article by Benard et al. [207]. The authors of the study carried out experiments in the same conditions for both Pt/CeO_2 (Cat1) and Pt/Al_2O_3 (Cat2). Both experiments were simulated and are shown in Figure 5.9a. The surface areas of CeO_2 and Pt resulting from the calculation are 3.5 m^2 and $1.72 \cdot 10^{-4}$ m^2 (Cat1 and Cat2) respectively. The latter corresponds to a dispersion of 0.03 % calculated using the area of one Pt site ($8.00 \cdot 10^{-20}$ m^2/atom from [86]) and a weight fraction of 1 % Pt as measured by Benard et al. Since a typical Pt dispersion on ceria is about 20% [221, 207], it must be presumed that all of the surface area of the 200 mg of catalyst used in the experiment was not accessible. The fits in Figure 5.9a are reasonable, considering that the kinetic parameters used for the simulation were derived from experiments in very different operating conditions and featuring differently synthesised catalysts. Position in temperature is not altogether correctly simulated, but peak shapes and heights are fairly well reproduced, as well as the fact that the major difference between Pt/Al_2O_3 and

Pt/CeO_2 in NO oxidation is a very slight temperature shift [222, 207]. Note that the slight double peak for Cat2 is not always seen to be a characteristic of NO oxidation over this catalyst (e.g. [86]). Clearly, reactivity between 100 and 200 °C is again underpredicted as it was for Pt/Al_2O_3 in this and other studies. In particular, the "wavy" shape of the ascending slope for Cat1 is captured. As found in Section 5.3, this profile (also observed in Figures 5.5 and 5.9b) arises because Ce-NO_2 is successively channelled into nitrates and NO_2, leaving fewer nitrites as an input for NO production at 350 and 450 °C circa. The shape of the "wavy" NO profile is attenuated by the presence of Pt. Overall, NO oxidation over Pt/CeO_2 differs very little from that over Pt/Al_2O_3 and the advantage of ceria appears to be mainly its storage capacity.

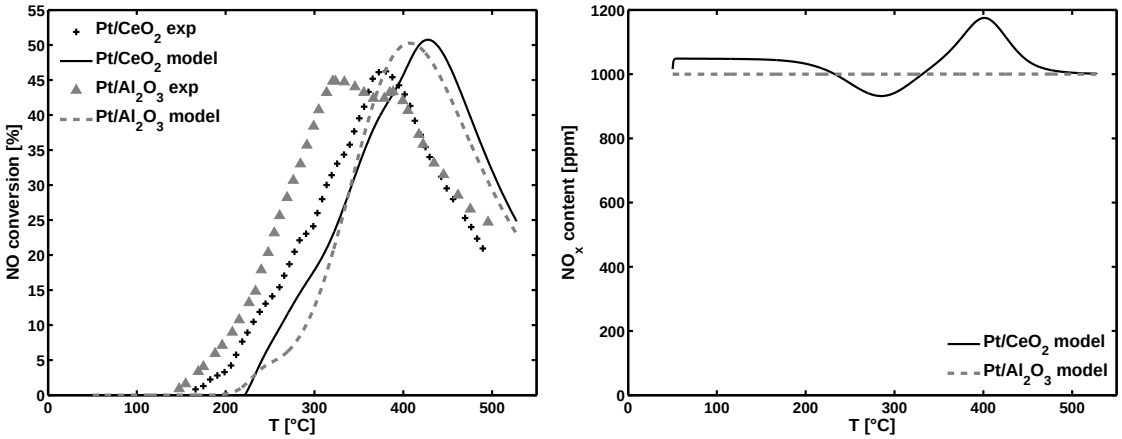

Figure 5.9: Predicted and experimental curves for the oxidation of 1000 ppm NO in 20% O_2 over Pt/CeO_2 (NRMSD=20.94%) and Pt/Al_2O_3 (NRMSD=34.40%). Experimental data from [207].

Results from an NO oxidation experiment over $Pt/Ce_{0.73}Zr_{0.27}O_2$ performed in this study are shown in Figure 5.10. NO conversion and NO_2 production commence immediately at room temperature. This is interesting considering that NO conversion over the Pt/CeO_2 catalyst in Figure 5.9 starts much later, around 160 °C. Similarly, pure ceria, ceria zirconia or Pt/Al_2O_3 cause NO conversion to start around 300 or 150 °C respectively, in the conditions of Figures 5.4a and 5.8. No further measure-

ments of NO conversion or NO_2 formation over Pt/CeO_2 or $Pt/CeZrO_2$ could be found in the literature for direct comparison. However, strong synergies are often known to exist between platinum and ceria-based supports, modifying chemisorption and catalytic properties of the metal, although this varies greatly according to the reaction conditions [223, 224]. Pure ceria improves dispersion of supported metals and forms intermetallic cation-CeO_2 compounds under oxidising conditions [209, 225, 226]. Some other studies do not find any synergies between noble metal and ceria-based supports [222, 207], but further experiments would be necessary to determine whether formation of Pt^{2+} species or the introduction of Zr lead to the improved NO adsorption in our conditions. The parameters estimated from the experiments in previous sections underestimate activity below 300 °C (Fig. 5.10), and one can surmise that this low-temperature reactivity might be improved by adding a further, more reactive, surface species to the mechanism. Alternatively, in some reaction systems, ceria has been proposed to enhance the catalytic activity of Pt by storing oxygen spilt-over from Pt onto CeO_2 [79]. It has also been shown that oxygen spills over from Pt to ceria during catalytic soot oxidation under $NO+O_2$ [78]. Another way to model the low temperature activity of $Pt/Ce_xZr_{1-x}O_2$ catalysts might therefore be the inclusion of such a spillover step in the mechanism.

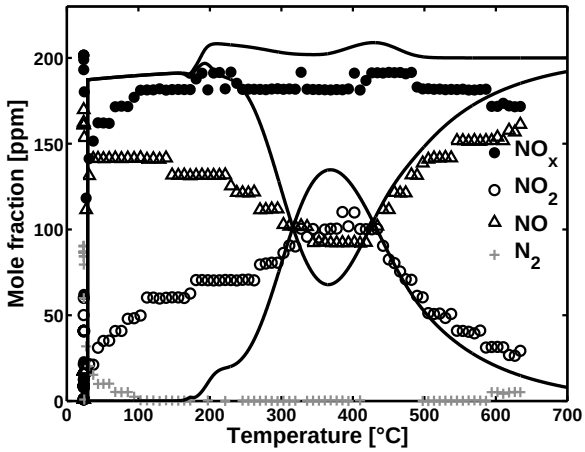

Figure 5.10: Predicted (solid lines) and experimental (symbols) curves for the oxidation of 200 ppm NO in 10% O_2 over $Pt/Ce_{0.73}Zr_{0.27}O_2$.

Storage behaviour of Pt/CeO_2 was further studied by comparing it to that of $Pt/BaO/Al_2O_3$,

which we have modelled previously [87, 198] and investigating the impact of NO+O_2 versus NO_2 feed. A steady state (constant T and feed composition) experiment performed by Scotti et al. [227] was chosen as appropriate for quantifying storage behaviour. As shown in Figure 5.11, when modelling NO_x storage and oxidation [198], BaO stored 1.17 and 1.48 mol NO_x/mol of storage sites for NO+O_2 and NO_2 feeds, respectively. In the same conditions, CeO_2 stored 0.22 and 0.12 mol NO_x/mol, in agreement with the finding for more complex gas feeds that Ba stores more efficiently than CeO_2 [228, 229, 230]. It is well known that more basic supports store more NO_x [231, 232] and our model reproduces this trend. Pt/CeO_2 stores NO_x better in presence of NO and O_2, although the difference is small, whereas Pt/BaO stores more efficiently in presence of NO_2. Note that the comparison was made using the same amount of active storage sites for both catalysts. These results also confirm the finding in Section 5.3 that NO/O_2 co-adsorption on ceria is more efficient. As pointed out earlier, the couple R11-R12 produces lattice oxygen (Ce-O) when exposed to the NO+O_2 feed, thereby facilitating the storage of nitrates (Ce-NO_3) via R17. Under an NO_2 feed, the only oxygen available is that of the lattice, which is consequently consumed by R11-R12, thereby deteriorating storage by R17.

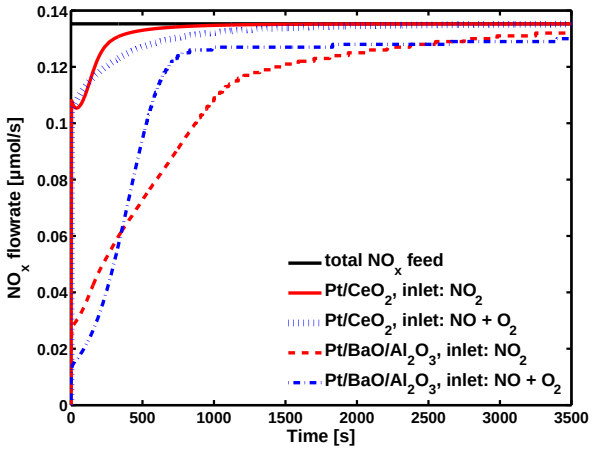

Figure 5.11: Predicted NO_x evolution over Pt/CeO_2 and Pt/BaO/Al_2O_3. Feed: 1000 ppm NO+ 3% O_2 (blue lines), 1000 ppm NO_2 (red lines). Operating conditions from [87, 227].

5.7 Conclusion

A detailed kinetic surface mechanism for the oxidation and storage of NO_x over platinum-, ceria- and ceria-zirconia-based catalysts was validated against experimental data from literature. The mechanism was coupled with a fixed-bed reactor model in order to extract the kinetic parameters. It was shown to perform well for data from different sources and operating conditions. The kinetic parameters obtained allow reproduction of the main trends of NO + O_2 desorption, NO oxidation and NO_x storage on the various catalysts. Storage on ceria and ceria-zirconia in the shape of nitrates stable until 350 °C is sufficient to reproduce NO+O_2 TPOs for %Zr≤64% and TPDs over pure CeO_2. However, a more detailed description involving at least one more N-surface species would probably improve TPD simulation. Efficiency of NO oxidation over ceria-based catalysts decreases with Zr content (0 - 64 mol %) and therefore depends on redox behaviour of the oxide, as demonstrated by the different values of kinetic parameters in the mechanism for ceria-zirconia catalysts. But above 64% Zr, it becomes necessary to take into account the effect of Zr-doping on the stability of nitrates. It was shown that in some cases it is possible to estimate detailed kinetic parameters for NO oxidation over platinum and ceria separately and obtain a reasonable prediction of the behaviour of Pt/CeO_2 by combining these parameters. In other cases however, significant synergies appear between noble metal and ceria-based support, and in this case the simple "block-merging"approach is not sufficient to model catalyst behaviour. Some experimental observations show however that modelling an additional, more active Pt species or an oxygen spillover step between Pt and CeO_2 may allow for reproduction of the low-temperature activity observed in some $Pt/Ce_xZr_{1-x}O_2$ catalysts. When coupling the present mechanisms for platinum and ceria, oxidation behaviour is dictated by Pt, but storage occurs over ceria. BaO remains a more efficient storage component than CeO_2, when considering an equal number of active sites, and unlike BaO, ceria stores NO (in presence of O_2) more efficiently than NO_2.

Chapter 6

$Pt/Ce_{0.73}Zr_{0.27}O_2$-Catalysed Soot Oxidation by O_2, NO and NO_2

Abstract

Certaines étapes réactionnelles d'intérêt pour le FaP n'ont pas été étudiées exhaustivement d'un point de vue cinétique et à notre connaissance aucun modèle capable de prédire réactivité globale et sélectivité entre produits de l'oxydation des suies par NO_x + O_2 en présence de $Pt/Ce_xZr_{1-x}O_2$ n'a été publié. Nous remarquons en revanche diverses études expérimentales importantes [82, 75, 233, 201] et des études visant à reproduire la formation de CO_2 pour des systèmes suies-CeO_2-O_2 [234]. Ces études nous ont permis d'établir des étapes réactionnelles probables, dont certaines ont été simulées dans les chapitres précédents. Dans ce chapitre, nous couplons ce schéma cinétique avec une étape de spillover d'oxygène entre cérine et suies dont nous ajustons les paramètres. Nous montrons qu'il est ainsi possible de bien prendre en compte l'impact de différentes valeurs du ratio catalyseur/suies sur les profils de CO_x.

⋆

The kinetics of some steps of interest for DPFs have not been studied extensively and

to our knowledge no model capable of predicting global reactivity and species selectivity of soot oxidation by $NO_x + O_2$ over $Pt/Ce_xZr_{1-x}O_2$ has been published. There are however several significant experimental studies of the latter subject [82, 75, 233, 201] and a modelling study which reproduces CO_2 formation of the CeO_2-catalysed soot-O_2 reaction [234]. These have yielded sufficient data on reaction products and intermediates to be able to conceive of a number of likely reaction steps. Some of these, such as the reaction of soot with NO_x and O_2 and NO and O_2 interaction with $Pt/Ce_xZr_{1-x}O_2$ have been modelled in the previous chapters [235, 90]. Here, we merge these set reaction steps with a description of oxygen spillover between ceria and soot to predict soot reactivity with $Pt/Ce_{0.73}Zr_{0.27}O_2$. The new parameters are estimated by fitting model equations to TPOs performed during the course of the study. It is shown that such a mechanism is able to describe some of the major trends of $Pt/Ce_{0.73}Zr_{0.27}O_2$-catalysed diesel soot oxidation with NO_x and O_2 in conditions of interest to normal DPF operation (25 - 850 °C, 70 - 1400 ppm NOx, 6 - 20 % vol. O_2), including the effect of a variation of catalyst/soot ratio.

6.1 Catalysed Soot Oxidation in Absence of Reactive Gases

Most experiments in this chapter refer to a loose contact mixture of 5 mg soot and 25 mg $Pt/Ce_{0.73}Zr_{0.27}O_2$, except for those performed to investigate the role of the soot/catalyst ratio or the type of contact. The designation $Pt/CeZrO_2$ is used in this chapter to refer to $Pt/Ce_{0.73}Zr_{0.27}O_2$. A TPO of the typical soot/catalyst mixture was performed under argon alone (Figure 6.1). While the amount of CO_2 produced is small, CO concentration is negligible. Production of CO_x in this case has to be ascribed to oxygen previously adsorbed on the soot and the catalyst and/or lattice oxygen from ceria. Temporal integration of the product mole fractions shows this amount of oxygen to be $6.47 \cdot 10^{-5}$ mol. Assuming that the amount of oxygen originating from the soot surface is equal to the $3.74 \cdot 10^{-5}$ mol found to be on soot in a soot-NO experiment (presented earlier, in Figure 4.8), the oxygen contribution of the catalyst can be calculated to be $2.73 \cdot 10^{-5}$mol O. These oxygen atoms presumably migrate from the catalyst to the soot surface.

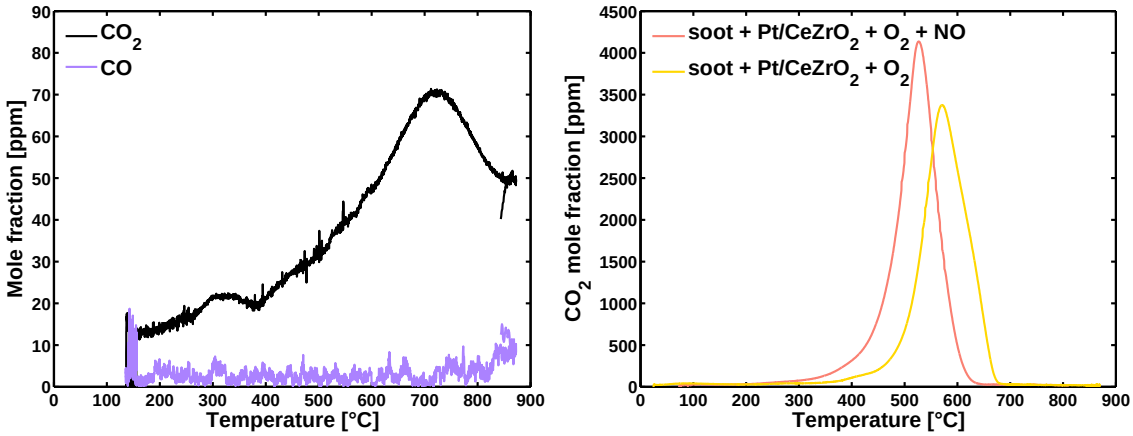

(a) Feed: 100 % Ar **(b)** Feed: 200 ppm NO and/or 10 % O_2 in Ar

Figure 6.1: Experimental CO and CO_2 production from soot oxidation in presence of $Pt/Ce_{0.73}Zr_{0.27}O_2$.

In support of this, TAP experiments by Bueno-López et al [78] show that O_2 is adsorbed on the active sites of Pt and CeO_2, and then transferred from Pt to CeO_2. Reactor experiments in a number of other studies back up these findings [236]. The resulting active oxygen species reacts with soot in a spillover reaction to produce CO and CO_2 [78, 234, 236, 43, 237]. On this basis, the experimental data in Figure 6.1a were used to propose a spillover step (R27), as shown in Table 6.1. Subsequent oxidation of the spiltover oxygen to yield CO_2 appears to occur by reaction between two spilt-over oxygenated surface species on soot, since no O_2 is present in the atmosphere. This kind of oxidation step is also proposed by [78, 234]. However experiments with gas phase O_2 (Figure 6.1b) show that much more CO_2 is produced and one cannot exclude that this increased reactivity may be due to reaction of spilt-over oxygen with gas phase O_2. An oxidation step of spilt-over oxygen is therefore proposed in analogy with the mechanism of the non catalytic soot-O_2 reaction: R28 in Table 6.1. Some of the more important steps of the mechanism are shown in Figure 6.2.

The descending slope of the CO_2 profile in Fig. 6.1a breaks between 800 and 900 °C and appears to make way for the start of a second peak. The same observation was

Table 6.1: Spillover and oxidation reactions

	Reaction
R27	C* + Ce-O → C*(O_{spill}) + Ce
R28	2 C*(O_{spill}) + O_2 → CO_2 + *

made by Bassou et al. [234], who attributed the second peak to ceria bulk oxygen as a second oxygen reservoir. The first oxygen reservoir is seen as being the surface oxygen on ceria. The comparison between the experiments with O_2 and under an inert gas shows that the surface oxygen reservoir is used preferentially. Bulk oxygen only reacts at T > 850 °C, when no surface or gas phase oxygen is available. The bulk species therefore have no bearing on a DPF application, and the reactions of ceria are thus represented by the surface species in Tables 6.1 and 5.1. CO production was neglected because of the small amounts formed in all experiments involving $Pt/Ce_{0.73}Zr_{0.27}O_2$. The new parameters used for the simulation in Figure 6.1 are relative to the reactions in Table 6.1, and all the other parameters are kept as in Tables 4.2 and 5.3. Low-temperature activity is not accurately reproduced, and CO_2 formed below 600 °C is assumed to originate from oxygen previously adsorbed on soot.

6.2 Catalysed Soot Oxidation by NO

A TPO experiment of soot alone under NO (Chapter 4) showed that NO is reduced to form N_2, but no NO_2 is formed because of the absence of the oxidant O_2. When $Pt/Ce_{0.73}Zr_{0.27}O_2$ is added, and the experiment repeated in the same conditions (Figure 6.3), again no NO_2 or N_2O are produced, so that the only N-containing product can be assumed to be N_2 (Figure 6.4). However, as Figure 6.4 shows, the amount of N_2 (calculated from a nitrogen balance) formed is much greater in the presence of the catalyst. It can be presumed that both soot and catalyst contribute to the reduction of NO, since both Pt and CeO_2 are known to decompose NO [238, 219]. When adding oxygen to the reactive mix (Fig. 6.4 and 6.5), much less NO is consumed, NO_2 is formed and N_2 formation inhibited. A similar behaviour had been observed

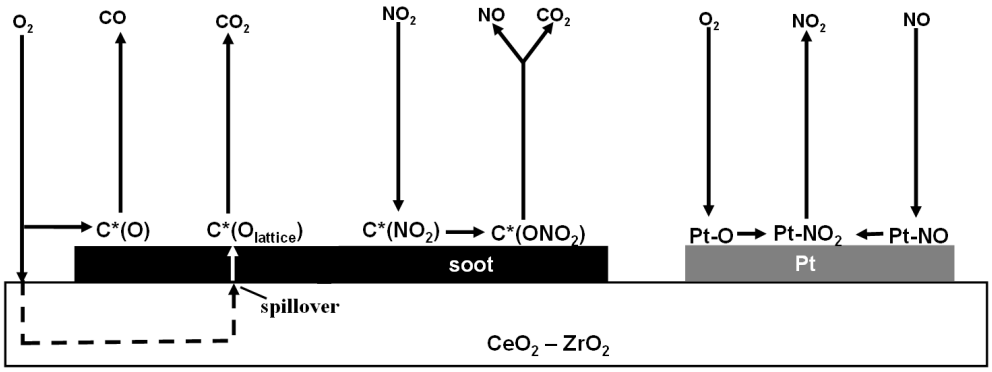

Figure 6.2: Schematic depiction of some of the more important reaction steps in the model.

in Chapter 4 for TPOs in absence of the catalyst. It must hence be assumed that on both the soot and the $Pt/Ce_{0.73}Zr_{0.27}O_2$ surface, oxygen is adsorbed preferentially, at least at the quantities used for these experiments [238]. Considering the significant O_2 concentration in diesel exhaust fumes, the conditions in a DPF are not conducive to the formation of N_2, except to a lesser degree at temperatures below 200 °C, where small amounts of N_2 are observed even in the presence of O_2 (see red line, in Figure 6.4). NO dissociation over soot (Fig. 4.8) and/or over $Pt/Ce_xZr_{1-x}O_2$ (Fig. 6.4) is thus inhibited by the presence of O_2 , in favour of NO_2 formation. NO reduction over platinum and ceria can be taken to have no bearing in such conditions and we do not plan to model the steps in this subsystem.

Figure 6.3b shows the effect of adding $Pt/Ce_{0.73}Zr_{0.27}O_2$ to soot-NO experiments on CO and CO_2 profiles. As all the experiments with soot and catalyst in this study do, it shows strong selectivity towards CO_2, with typically no more than 5 ppm of CO produced, as opposed to the 20 ppm produced with soot alone. Total CO_x emissions over time, calculated as CO + CO_2, hardly differ in the two cases. The only exception to this is the initial 40 ppm-peak of CO_2 at 100 °C observed in presence of the catalyst. Similar peaks of about 30-40 ppm are observed in $Pt/Ce_{0.73}Zr_{0.27}O_2$-soot-NO-O_2 and $Pt/Ce_{0.73}Zr_{0.27}O_2$-soot-O_2 experiments. Since this early peak is not

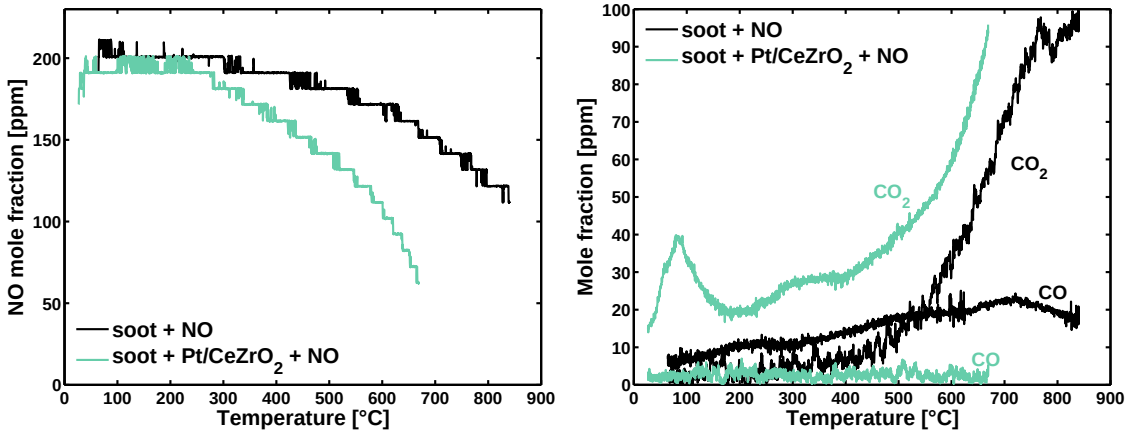

(a) NO consumption **(b)** CO_x production

Figure 6.3: Experimental mole fractions during soot oxidation with or without $Pt/Ce_{0.73}Zr_{0.27}O_2$ under 200 ppm NO.

observed in experiments on soot alone, it can be surmised that it is due to an early spillover of some previously adsorbed species (e.g. carbonates [236]) from the catalyst surface.

An oxygen balance for the soot-catalyst-NO experiment shows that there are an additional $3.55 \cdot 10^{-5}$ mol O in the products. As in the previously described TPO with 100% Ar, the extra oxygen atoms are presumed to originate from the soot surface and the catalyst. However, if the amount of oxygen pre-adsorbed on soot is again taken to be close to the $3.74 \cdot 10^{-5}$ mol calculated in the soot-NO experiment, very little of the extra oxygen in the reaction products comes from the catalyst. This is not necessarily surprising: the reaction of carbon with O originating from NO might well be more favourable than that of carbon with lattice or surface oxygen from $Pt/Ce_{0.73}Zr_{0.27}O_2$ and isotopic studies using ^{18}O and ^{16}O could clarify this point.

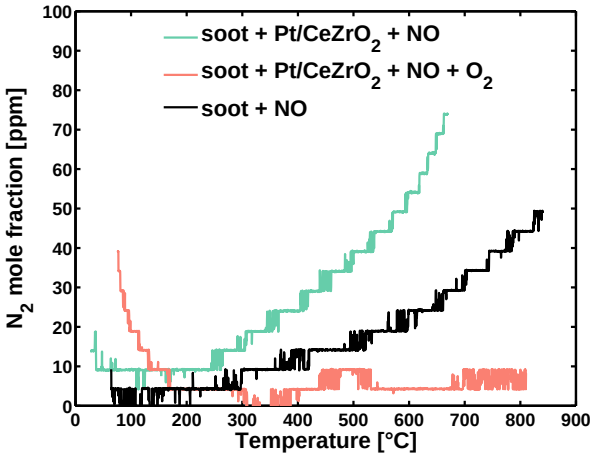

Figure 6.4: N_2 production from soot oxidation with or without $Pt/Ce_{0.73}Zr_{0.27}O_2$ and under different reactive atmospheres.

6.3 Catalysed Soot Oxidation by NO + O_2

In Figures 6.6a,b, CO and CO_2 mole fractions of a soot-catalyst TPO under NO and O_2 are compared with those obtained under different gas feeds or without catalyst. Only the oxygen-containing gas feeds are considered in this figure, as reaction with NO alone yields much smaller quantities of CO_x (Figures 4.8b and 6.3b). For easier comparison, the mole fractions shown here are normalised with respect to carbon mass obtained by integration of the CO and CO_2 profiles. As expected, the experiments show that addition of $Pt/Ce_{0.73}Zr_{0.27}O_2$ improves soot oxidation. However, the impact of the catalyst is more significant in presence of NO: Temperature at peak concentration is 515 °C as opposed to 580 °C under O_2 alone and 680 °C in absence of catalyst.

Considering that CO_x production in absence of $Pt/CeZrO_2$ is hardly affected by the addition of NO, it seems likely that the interaction of NO with the catalyst plays a role in the improved oxidation. It can be presumed that reaction with NO_2 (produced by NO oxidation on the catalyst) is partly responsible for improved soot consumption. This is supported by the fact that overall CO_x production under NO alone (i.e. no NO_2 is formed) is not increased by the catalyst.

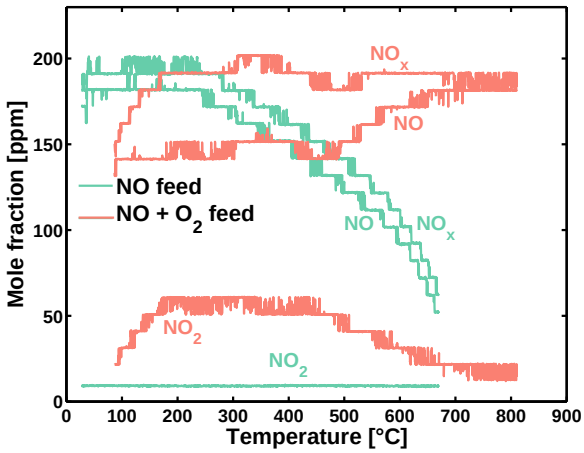

Figure 6.5: NO, NO_2 and NO_x mole fractions during soot oxidation in presence of $Pt/Ce_{0.73}Zr_{0.27}O_2$ and 200 ppm NO, with or without 10% O_2.

However, at the typical NO content of 200 ppm, the contribution of carbon atoms oxidised by NO_2 remains minor. If one calculates the amount of NO_2 originating from NO oxidation over the catalyst from the area under the grey curve in Figure 6.6c and the amount of NO_2 not reacting with soot from the area under the red curve, then their difference (the hatched area) represents NO_2 that did react with soot (neglecting NO_2 produced over soot itself, area under the violet curve, Fig. 6.6c). From integration of the measurements, this was found to be $7.34{\cdot}10^{-5}$ - $4.61{\cdot}10^{-5}$ = $2.72{\cdot}10^{-5}$ mol NO_2. The amount of O in this quantity of NO_2 is $5.46{\cdot}10^{-5}$ mol O, which is only 6% of the $8.64{\cdot}10^{-4}$ mol O found in the products CO_x (red curves, Figures 6.6a and b). Moreover, the addition of $Pt/CeZrO_2$ to soot-O_2 experiments leads to a shift toward lower temperatures by 110 °C, whereas the addition of NO to soot-$Pt/CeZrO_2$-O_2 experiments decreases it by only 45 °C. These considerations support the idea that oxygen spillover from catalyst to soot plays a more important role than NO_2 in enhancing soot oxidation in presence of $Pt/CeZrO_2$.

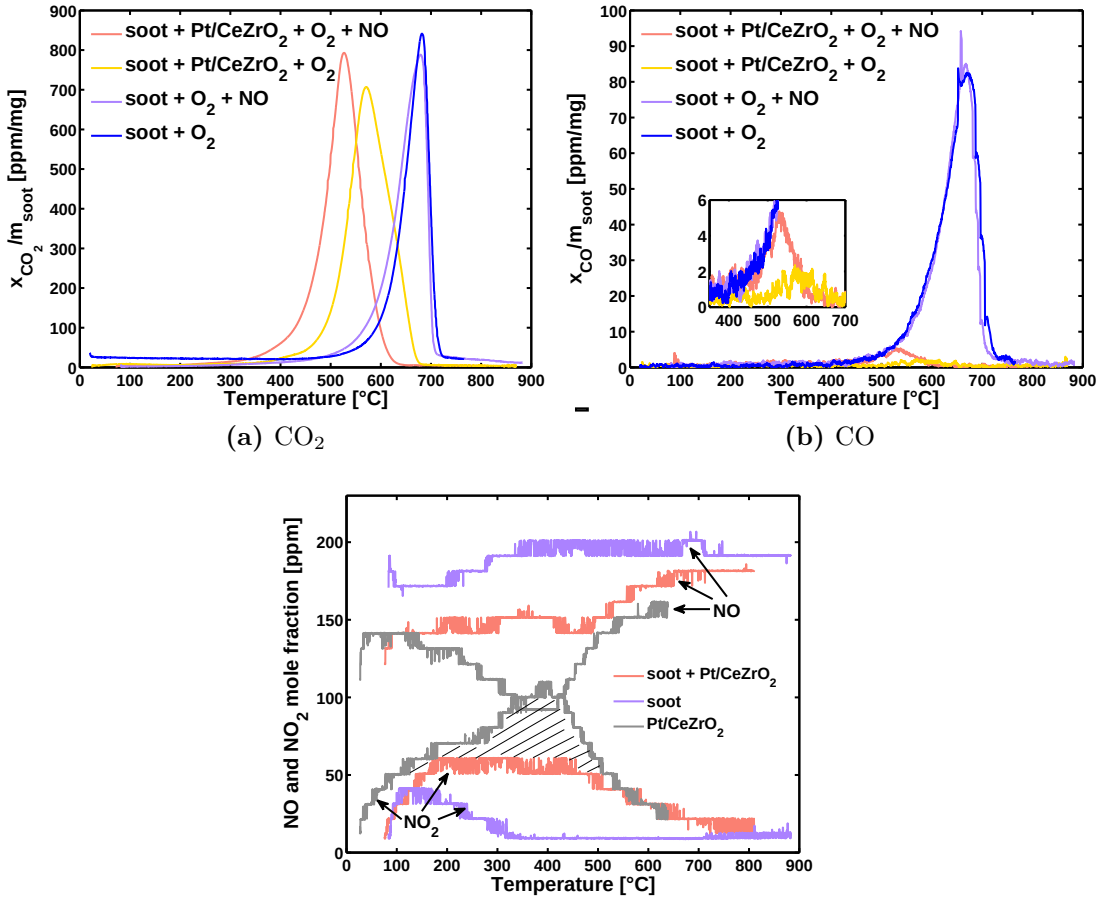

(a) CO_2 **(b)** CO

(c) NO and NO_2

Figure 6.6: Experimental mole fractions during soot oxidation with or without $Pt/Ce_{0.73}Zr_{0.27}O_2$ under 200 ppm NO + 10 % O_2.

Neglecting for the moment the low-temperature activity of the catalyst (see Chapter 5), the oxidation of CO over the catalyst and some other expected interactions, the experimental CO_2 profile for a catalyst/soot ratio of 5 (red line in Fig. 6.7) was used to estimate the parameters of R27 and R28 (Table 6.1). The values of A_{27} and E_{27} are 10^{17} $cm^2/mol/s$ and 85 kJ/mol, respectively, and A_{28} and E_{28} equal $4{\cdot}10^9$ $cm^3/mol/s$ and 102 kJ/mol.

Addition of $Pt/Ce_{0.73}Zr_{0.27}O_2$ to soot enhances the rate of oxidation. An example of the effect is shown in Fig. 6.7, as the experimental CO_2 peak shifts to temperatures

below 650 °C. The more catalyst is added, the more marked the effect becomes, and the TPO curves become taller and narrower. The simulation results in Figure 6.7 show that progressively lower pre-exponential factors for the oxidation step by lattice oxygen, A_{28}, allow for the reproduction of CO_2 formation with different catalyst/soot ratios. A fit of these values turns out to follow logarithmic behaviour with respect to the catalyst/soot ratio:

$$A_{28} = 1.264 \cdot 10^9 ln\left(\frac{c}{s}\right) + 1.975 \cdot 10^9 \quad [cm^3/mol/s] \tag{6.1}$$

For all $\frac{c}{s}$, spillover is favoured over the other possible path of oxygen onto the soot surface, direct adsorption.

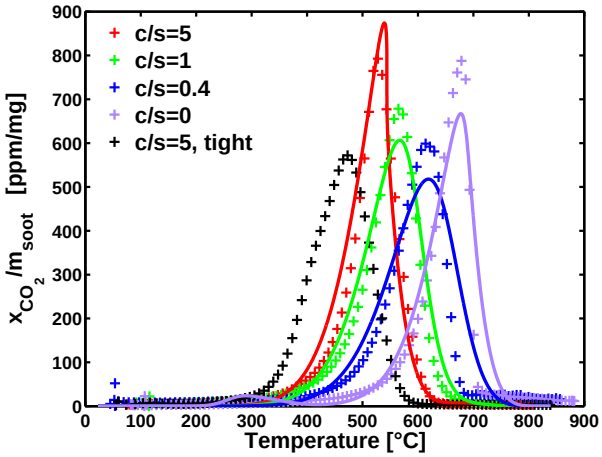

Figure 6.7: Experimental (symbols) and simulated (lines) CO_2 profiles for different catalyst/soot ratios, 200 ppm NO, 10 % O_2, 10 °C/min.

The value of A_{28} encloses the effects of the initial catalyst/soot ratio, of its variation during the course of the reaction and of the contact area between soot and catalyst on the oxidation rate of spilt-over lattice oxygen. It is also indirectly representative of the effect of the above mentioned factors on the spillover rate. While the CO_2 mole fractions corresponding to different values of are well reproduced for all the experiments using loose contact, this coarse representation is not sufficient to simulate reactivity of a tight contact mixture (Fig. 6.7, black symbols) as well. A number

of modelling alternatives can be suggested: the spillover could be considered as the rate determining step [234]; and A_{27} can be expressed as a function of $\frac{c}{s}$, in a manner similar to the modelling study of soot oxidation by CeO_2 by Bassou et al. [234], where however not only $\frac{c}{s}$ influences the rate, but also a number of other contact parameters. Furthermore, the evolution of contact area could be taken into account explicitly, as done for a global oxidation reaction of carbon black by CeO_2 in [76].

6.4 Conclusions

Kinetic parameters for a detailed mechanism of the $Pt/Ce_{0.73}Zr_{0.27}O_2$-catalysed soot oxidation by NO_x + O_2 were estimated using concentration profiles of the major product species. Soot oxidation in presence of catalyst occurs by oxygen spillover from the ceria support. This transfer is more efficient than direct oxygen adsorption on soot. Parameters of oxidation by spiltover lattice oxygen were found to display logarithmic behaviour with the catalyst soot/ratio. Work on a number of further reaction steps of this system is currently in progress.

Chapter 7

Conclusions and Outlook

This study is an attempt at understanding the kinetics of some of the heterogeneous catalytic and non-catalytic reactions relevant for diesel particle filters (DPFs) using the microkinetic/semi-detailed meanfield modelling approach. In particular, the approach is applied to soot oxidation catalysed by $Pt/Ce_{0.73}Zr_{0.27}O_2$, a catalyst formulation known to be particularly active. Microkinetic meanfield modelling allows for a description of the reaction kinetics in some detail, often via "lumped" intermediate species representative of a group of the physically observed species. However, it neglects the effects of surface heterogeneity of the reactive solid (soot or catalyst). A point that is applicable to all the reaction systems studied here, is that the measurement of surface species can mostly contribute only qualitative phenomenological information to meanfield modelling (nature and temperature of appearance of intermediate species), but no quantitative measurements of surface coverage. However quantitative gas species measurements are used for parameter estimation.

During the course of this study, the meanfield approach has been used to gain insight into the mechanism of soot oxidation by NO_x and NO_x+O_2. In the current literature, these systems had not yet been studied extensively from a meanfield perspective, unlike the C-O_2 reaction, which is modelled more frequently. This study has drawn on the many parameters proposed in the literature for the C-O_2 reaction as well as the mechanisms proposed on the basis of experimentally observed surface species. Many previously unavailable kinetic parameters were determined by comparison with gas phase product concentrations measured both in the literature and in experiments

performed in this study. The soot-NO mechanism suffers from lack of availability of surface species measurements and future work on this aspect would allow one to improve the mechanism's level of detail. However, the information on soot oxidation by O_2 or NO_2 is more relevant to DPFs and the literature much more abundant. Overall, the mechanistic parameters determined for the C-NO_x-O_2 reaction allow for the prediction of a number of temperature programmed fixed bed experiments.

Using the same approach, NO oxidation over ceria was modelled and kinetic parameters determined using several fixed bed experiments. The mechanism was proposed on the basis of the relatively abundant literature on observed surface species. While NO oxidation and other reaction over ceria are commonly studied experimentally, no meanfield models were available for comparison. Similar experiments from the literature were then modelled for ceria-zirconia catalysts with differing zirconium contents. For molar zirconium contents below 64%, the effect of increasing zirconium content can be modelled by smaller activation energies and pre-exponential factors in a microkinetic reduction step of ceria, without the need to introduce the Zr species in the mechanism.

Parameters of NO oxidation over Pt/Al_2O_3 were determined on the basis of a well-established mechanism from the literature. It was then shown that high temperature activity of a Pt/CeO_2 catalyst could in one case be successfully reproduced by coupling the two previously mentioned mechanisms. However, many experiments, including one performed in this study, lead to the conclusion that platinum and ceria when combined in a single formulation can exhibit significant synergetic effects, the composite formulation can be active at temperatures below 100 °C, where neither of the single components would be expected to be active. When such effects are present, the "piece-wise" approach to parameter estimation is insufficient, and future work would aim to describe the synergy explicitly, by formation of a more active surface species, for instance. The piece-wise method for parameter fitting has however been used successfully for fitting all the parameters in this study, since many of these cases present no specific synergy between the components being merged. The methodology consists in determining small subsets of parameters at a time by comparison with all the reaction products from relevant experiments, then fixing these

parameters and determining further parameters subsets with other experiments. For instance, parameters pertaining to the soot-NO reaction were determined by fitting to NO, N_2, CO and CO_2 measurements from a soot-NO experiment. An analogous method was used for soot-O_2, and a further subset of parameters was determined from soot-NO-O_2 experiments when merging the previously determined parameters.

In some of the soot-related systems, attempts were made to overcome the limitation of neglecting surface heterogeneity, typical of the meanfield approach. Since kinetic parameters in meanfield modelling represent average effects of the whole surface, different values of such parameters can represent different states of the surface. Where the oxidation of soot is concerned, one often distinguishes differently measured surface areas (ASA, TSA, RSA) as macroscopic averaged indicators of surface structure. In this study, it was shown that the oxidation of carbon materials with increasingly regular (surface) structure can be modelled employing linearly increasing activation energies for some of the CO_2-producing steps in a microkinetic mechanism, where it was assumed that molar carbon content was indicative of structural order. Unlike the use of surface areas, this approach allows one to model the disparate effects that differing degrees of structural order of the reactive surface can have on the different steps in a microkinetic mechanism. This use was illustrated by means of the C-NO reaction, where the NO adsorption step is modelled as not being affected by greater structural order, which the CO_2-producing step on the other hand is affected by.

The various subsets of steps were merged for a mechanism of soot oxidation catalysed by Pt/$Ce_{0.73}Zr_{0.27}O_2$ and two new steps introduced, including oxygen spillover from ceria to soot. Several steps of potential interest to this system (such as CO oxidation on Pt) have been neglected, but work on meanfield models of these steps is ongoing. However, the present mechanism is sufficient to reproduce the catalysed soot oxidation by a mixture of NO and O_2, and more or less efficient oxidation step parameters for spilt-over oxygen can account for the effect of different catalyst-soot ratios.

Conclusions et Perspectives

Ce travail porte sur la compréhension de la cinétique des réctions hétérogènes catalytiques et non catalytiques qui ont de l'intérêt pour les FaP. L'approche utilisée est basée sur l'approximation du champ moyen et des schémas réactionnels microcinétiques ou semi-détaillés. Cette approche est appliquée à l'oxydation des suies par $Pt/Ce_{0.73}Zr_{0.27}O_2$, qui est une formulation catalytique identifiée comme particulièrement active. L'approche de modélisation employée permet de décrire les étapes reactionnelles de manière plutôt détaillée par des étapes élémentaires ou "lumpées", ou éventuellement des espèces lumpées. Cependant, l'approche utilisée ne tient pas compte de l'hétérogénéitée des surfaces réactives (suie ou catalyseur). Les paramètres cinétiques des étapes reactionnelles sont estimés en ajustant les concentrations gazeuses calculées aux mesures expérimentales. Les mesures d'espèces surfaciques peuvent toutefois n'être utilisées que de façon qualitative. Elles permettent d'observer la formation des intermédiaires, mais pas la valeur des concentrations de surface.

Une approche de modélisation basée sur l'approximation du champ moyen a été utilisée pour étudier les mécanismes de l'oxydation des suies par des mélanges NO_x et NO_x+O_2, qui n'avaient pas fait l'objet d'une étude similaire auparavant. Les paramètres cinétiques correspondants ont été évalués. Ce faisant, nous avons exploité des nombreuses données bibliographiques, particulièrement celles portant sur l'oxydation de la suie par O_2. La modélisation du mécanisme d'oxydation par NO bénéficiera dorénavant de données expérimentales supplémentaires, puisque l'on retrouve très peu de mesures d'espèces de surface pour des expériences de ce type. Cependant, les réactions avec O_2 et NO_2 sont plus représentatives du fonctionnement d'un FaP, et les données bibliographiques plus nombreuses. Dans l'ensemble, le modèle permet de reproduire un nombre important de résultats expérimentaux obtenus en

température programmée.

La même approche a été appliquée à l'oxydation de NO sur cérine. Nous avons proposé le mécanisme reactionnel sur la base des nombreuses observations d'espèces de surface que l'on retrouve dans la bibliographie. Cependant, l'approche de modélisation basée sur l'approximation du champ moyen n'avait auparavant pas été appliquée à l'oxydation de NO sur cérine. De façon analogue, nous avons ensuite étudié la cinétique mise en jeu sur des cérine-zircones dans ces conditions opératives. Pour une teneur en zircone inférieure à 64%, l'effet de la teneur en zirconium dans la phase active peut être reproduit par des énergies d'activation et facteurs pré-exponentiels d'une des étapes considérées.

Concernant l'oxydation de NO sur Pt/Al_2O_3, nous avons exploité des études expérimentales bien renseignées. Dans un cas, il a été possible de coupler les schémas cinétiques déjà mentionnés pour reproduire l'activité du catalyseur composé Pt/CeO_2. Cependant nos tests catalytiques font apparaître une synergie importante entre le platine et la cérine-zircone. La réactivité à basse température obtenue dans cette expérience est plus élévée que pour les autres catalyseurs étudiés. Dans ce cas, la méthodologie de couplage des sous-ensembles d'étapes ne suffit pas pour modéliser les résultats obtenus pour le catalyseur composé de façon satisfaisante. De nombreux cas ne représentant pas de synergie particulière ont en revanche été reproduits avec succès par la technique d'ajustement. Cette méthodologie consiste en un ajustement progressif de sous-ensembles des paramètres cinétiques. Par exemple, les paramètres portant sur l'oxydation de suies par NO ont été évalués par ajustement des profils simulés avec des mesures de NO, N_2, CO et CO_2 provenant d'une expérience d'oxydation de suies par NO. La méthodologie suivie pour la modélisation des expériences réalisées sur le système suies-O_2 est identique et d'autres paramètres ont ensuite été déterminés à partir des expériences sur le système suies-NO-O_2, en couplant les étapes figées précedémment.

Dans certains cas, nous avons tenté de tenir compte de l'hétérogénéité de la surface réactive carbonée dans le modèle cinétique. Étant donné que les paramètres cinétiques dans notre modèle représentent des effets moyens, une valeur différente

de ces paramètres peut correspondre à un ensemble d'états différents pour la surface. Nous avons donc montré que l'oxydation de suies avec une structure graphitique plus ordonnée peut être reproduite par une énergie d'activation plus importante pour de l'étape de production de CO ou CO_2. En particulier, cette énérgie d'activation croît linéairement avec la teneur en carbone, cette teneur étant considérée comme un indicateur d'une structure plus ou moins ordonnée. Contrairement à une approche basée sur la valeur de la surface réactive (RSA), cette méthodologie nous permet de prendre en compte les effets complexes d'une structure plus ou moins hétérogène sur les différentes étapes réactionnelles. Pour illustrer cette procédure, nous avons appliqué cette démarche à la réaction entre la suie et NO. L'étape d'adsorption de NO est insensible à une structure plus ordonnée, l'étape de formation de CO_2 en revanche est bien affectée.

Les sous-ensembles d'étapes réactionnelles ont été couplés, et deux étapes supplémentaires ont finalement été introduites afin de reproduire l'oxydation des suies catalysée par $Pt/Ce_{0.73}Zr_{0.27}O_2$. Les étapes rajoutés décrivent le "spillover" d'oxygène de la cérine vers la suie. Tout en négligeant certaines étapes potentiellement intéressantes, nous avons montré que le schéma proposé suffit pour représenter nos expériences d'oxydation pour diverses valeurs du ratio catalyseur/suies.

Appendix A

Application: 3D Model of Soot Oxidation in a Fixed Bed

A.1 Scope and Outlook

DPFs typically function according to a wall flow arrangement (see Chapter 1), where soot particles are separated from the exhaust gas as it flows through a porous filtering medium. In order to model a full scale DPF then, a description of the gas flow through such a medium is needed, the pressure drop across a porous medium being of particular importance in such representations. Because of the complex flow in DPFs, 3D models are often appropriate for predicting and analysing phenomena such as hotspots and maldistribution. On the other hand, simpler (0D) descriptions can also be useful, such as the DPF component in the IFP Exhaust library of the LMS AmeSim Environment described in Appendix B.

In the interest of understanding some of the more complex phenomena that can be observed when coupling detailed chemistry and flow descriptions [239], engineers at IFP Energies nouvelles are developing a 3D CFD model of a DPF. So far, a model of flow in porous media has been coded. The proper functioning of this code with respect to heat transfer and pressure drop has been verified during the course of this study. Furthermore, some of the reaction kinetics developed during the thesis were implemented into this 3D model with a view to simulating some of the fixed

bed experiments described in Chapter 2. This procedure allowed for validation by comparison with the CSTR model described in Chapter 3, since no spatial dishomogeneities are expected in laboratory fixed bed reactors. Flow entering the fixed bed is thus at first taken to be homogenous, and at a later stage the impact of a flow pattern more representative of conditions in a DPF will be tested. This initial phase is seen as a test of the model representing the porous filtering medium, Figure A.1, where only the oxidation of a deposit of soot is simulated, but not the process of deposition of soot particles. The fixed bed of porous material (Figure A.1) therefore represents a bed of particles such as in a laboratory reactor, or a layer of soot in a DPF together with the filtering medium on which it is charged. The soot deposit is assumed to be homogeneous, but an investigation of the impact of an uneven distribution of soot particles is planned as one of the next steps. Once all of the mentioned aspects have been tested, the initial model is to be developed further so as to reproduce the functioning of an entire wallflow monolith.

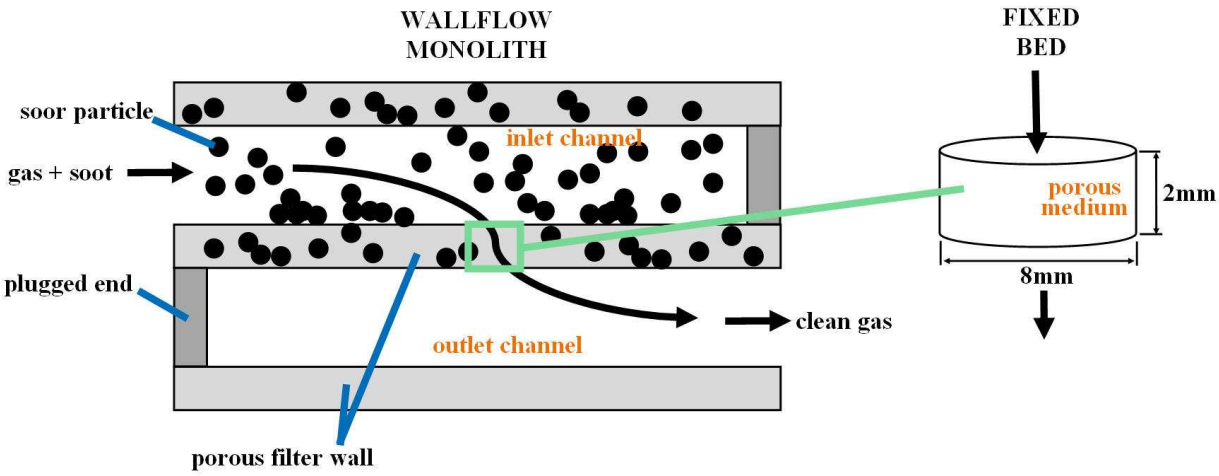

Figure A.1: Schematic depiction of a wallflow monolith and the porous subsystem currently being modelled at IFPEN.

A.2 The Model

A pseudo-continuum approach is used, which means that the flow is described via modified Navier-Stokes equations and the solid and gas phases are distinguished via the porosity, ε [240]. These pesudo-continuous equations of motion are established by coupling the empirical Carman-Kozeny pressure drop correlation with the Navier-Stokes equations. The model is written as the system of equations A.1-A.5 and the time derivatives are currently discretised in time according to the explicit, first-order Euler method and in space according to a finite volume method.

$$\partial_t(\varepsilon\rho_i) + \nabla\cdot(\varepsilon\rho_i\mathbf{u}) = \dot{\omega_i} \tag{A.1}$$

$$\partial_t(C_{s,k}) = \dot{\omega_k} \tag{A.2}$$

$$\nabla p = -\mathbf{S} \tag{A.3}$$

$$\partial_t(\varepsilon\rho e) + \nabla\cdot(\varepsilon\rho e\mathbf{u}) + p\nabla\cdot(\varepsilon\mathbf{u}) = \nabla\cdot(\lambda\nabla T) + \varepsilon_s\eta_s(T_s - T) \tag{A.4}$$

$$\partial_t(\varepsilon_s\rho_s e_s) = \nabla\cdot(\lambda_s\nabla T_s) + \varepsilon_s\eta_s(T - T_s) + \dot{\omega_E} \tag{A.5}$$

Equations A.1 and A.2 represent N_g mass conservation equations for the gas phase species i and N_s mass conservation equations for the surface species k, respectively. Total density in the gas phase is designated as ρ, whereas the fractional densities ρ_i of gas phase species i are defined by

$$\rho = \sum_{i=1}^{N_g} \rho_i \tag{A.6}$$

where $C_{s,k}$ is the concentration of surface species k in mol/m^2, $\mathbf{u}$ the gas velocity vector and $\dot{\omega_i}$ and $\dot{\omega_k}$ the source terms of gas species i and surface species k, respectively. Equation A.3 describes the conservation of momentum, where p is the gas pressure and the vector $\mathbf{S}$ is a source term which accounts for two different types of friction, as already seen in Chapter 3 where the Carman-Kozeny relation was applied macroscopically.

$$S(\varepsilon, \rho, \mathbf{u}) = D\left(\frac{1-\varepsilon}{\varepsilon}\right)^2 \mathbf{u} + F\left(\frac{1-\varepsilon}{\varepsilon}\right)\rho\|\mathbf{u}\|\mathbf{u} \tag{A.7}$$

The first term on the right hand side of Eq. A.7 contains the Darcy coefficient D and is linear in $\mathbf{u}$, whereas the second term contains the Forchheimer coefficient F and depends on the square of $\mathbf{u}$. Equations A.4 and A.5 are conservation equations of the gas phase and solid internal energies, e and e_s. All symbols with the subscript s indicate solid phase quantities, including the solid fraction, which is defined as the ones' complement of ε:

$$\varepsilon_s = 1 - \varepsilon \tag{A.8}$$

λ and λ_s indicate thermal conductivity of gas and solid phase, respectively, and T and T_s the respective temperatures. The terms $\varepsilon_s\eta_s(T_s - T)$ and $\varepsilon_s\eta_s(T - T_s)$ are representative of thermal exchange between solid and gas phase. The volumetric heat transfer coefficient η_s in $\mathrm{W/m^3/K}$ between the two phases is evaluated as [241]:

$$\eta_s = \frac{Nu\ \lambda_s}{d_p/6} \tag{A.9}$$

where Nu is the Nüsselt number as calculated from the Ranz correlation.

Mass and energy source terms are calculated as

$$\dot{\omega_i} = \sum_{j=1}^{N_g} \nu_{i,j} r_j S_a M_i \qquad [kg/s] \tag{A.10}$$

$$\dot{\omega_k} = \sum_{j=1}^{N_s} \nu_{i,j} r_j \qquad [mol/m^2/s] \tag{A.11}$$

$$\dot{\omega_E} = \sum_{j=1}^{n_{reac}} \left(\sum_{j=1}^{N_g} \nu_{i,j} e_i + \sum_{k=1}^{N_s} \nu_{k,j} e_k\right) r_j S_a \qquad [W/s] \tag{A.12}$$

where heat of reaction is considered to be liberated in the solid phase only, since

the reaction steps involve surface species. Some of the symbols appearing above are already defined in Chapter 3, including the reactive surface area, S_a. Note however that, in the CFD model Equations A.1-A.5 are solved in every mesh cell of the discretised domain. In each of these cells S_a is therefore a local surface area, which represents only a fraction of the reactive surface used in the 0D calculations in Chapter 3, and is calculated as a fraction of the total area proportional to the volume of mesh cell q: $S_{a,q} = S_{a,tot}\frac{v_q}{v_{tot}}$. The underlying assumption is that the reactive solid (soot, in the cases simulated in this chapter) is evenly distributed. The internal energy associated with gas i or surface species k is computed as

$$e_i = H_{f,i} + \int c_{p,i} dT_s - \frac{pM_i}{\zeta_i} \tag{A.13}$$

$$e_k = H_{f,k} + \int c_{p,k} dT_s \tag{A.14}$$

Here, the enthalpies of formation of the species, $H_{f,i}$ and $H_{f,k}$, and the coefficients needed to approximate the integral in Eq. A.13-A.14 are taken from the NIST database. Of the above quantities, those pertaining to all the soot-surface species are approximated by using the NIST values for graphite.

Appendix B

Using the IFP Exhaust Library for Kinetic Modelling in Fixed Beds

Figure B.1 shows a screenshot of the LMS AmeSim working window. A fixed bed reactor system is modelled by the ensemble of drag-and-drop components in Fig. B.1. The component denoted by FB represents the model of the actual layer of reactive solid (soot or catalyst) in the reactor. Other components allow for the injection of a reactive gas stream with a certain composition, flow rate and temperature, and the gas analyzer component allows one to visualise the gas composition downstream of the fixed bed. The flow source and gas analyzer components are provided in LMS AmeSim libraries, but the FB component, including flow through the porous particle bed and all the surface reactions, was formulated and coded during the course of this thesis.

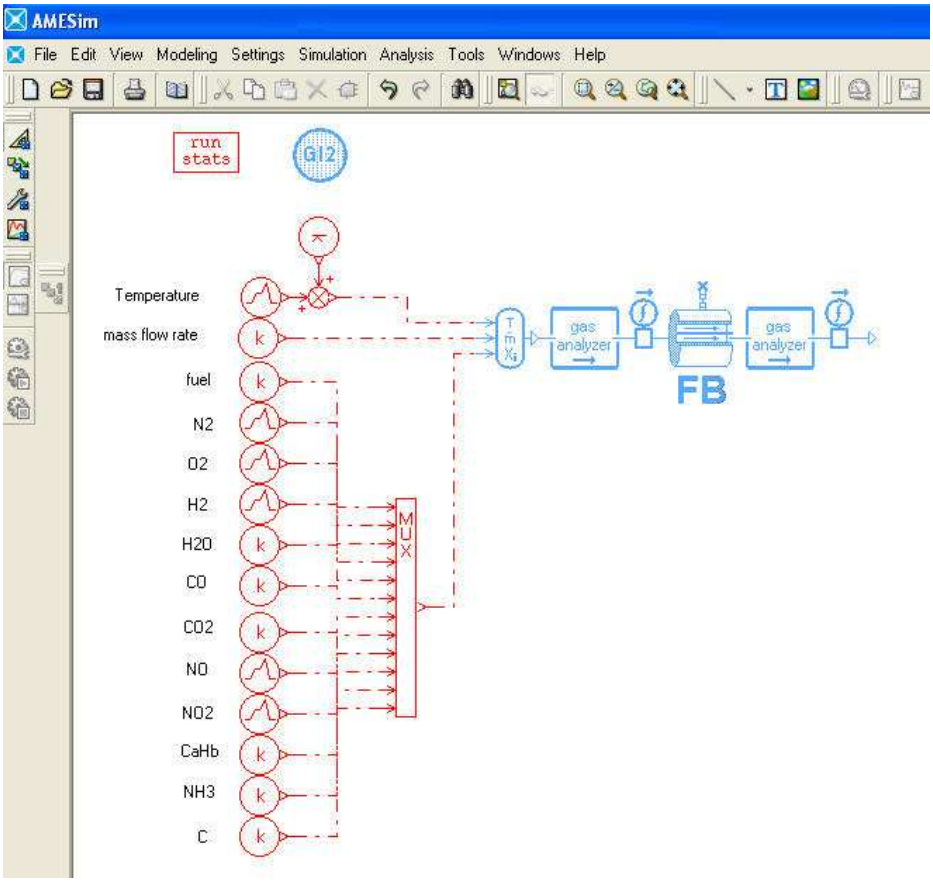

Figure B.1: Screenshot of the LMS AmeSim graphical user interface.

Appendix C

List of Publications

- [88] K. Leistner, A. Nicolle, D. Berthout and P. Da Costa, "Kinetic modelling of the oxidation of a wide range of carbon materials," *Combustion and Flame*, vol. 159, no. 1, pp. 64-76, 2012
- [235] K. Leistner, A. Nicolle and P. Da Costa, "Modelling the Kinetics of NO Oxidation and NO_x Storage over Platinum, Ceria and Ceria Zirconia," *Applied Catalysis B: Environmental*, vol. 111-112, pp. 415-423, 2012
- [90] K. Leistner, A. Nicolle and P. Da Costa, "Detailed Kinetic Analysis of Soot Oxidation by NO_2, NO, and NO + O_2," *The Journal of Physical Chemistry C*, in press, 10.1021/jp210312r
- K. Leistner, A. Nicolle and P. Da Costa, "Detailed Kinetic Analysis of Pt/CeZr-Catalysed Soot Oxidation,"in preparation

Bibliography

[1] B. A. van Setten, M. Makkee, and J. Moulijn, "Science and technology of catalytic diesel particulate filters," *Catalysis Reviews - Science and Technology*, vol. 43–44, pp. 489–564, 2001.

[2] O. Deutschmann and A. G. Konstandopoulos, *Catalytic Technology for Soot and Gaseous Pollution Control*. Wiley-VCH Verlag GmbH & Co. KGaA, 2010.

[3] "Air Quality Guidelines." `http://www.euro.who.int/Document/E90038.pdf`, 2005. World Health Organization.

[4] Z. Du, *Kinetic Modeling of Carbon Oxidation*. PhD thesis, Massachusetts Institute of Technology, 1990.

[5] A. J. McMichael, "The urban environment and health in a world of increasing globalization: issues for developing countries," *Bulletin of the World Health Organization*, vol. 78(9), pp. 1117–1126, 2008.

[6] Y. Hayashi, K. Doi, R. Suparat, and K. Sakurai, "Comparing the environment between cities in different stages of economic development and urbanisation," *Proceedings of 19th PTRC meeting (Civilising Transport)*, pp. 95–106, 1991.

[7] E. P. Agency, "Office of Air and Radiation." `http://www.epa.gov/`, 2009.

[8] M. E. Monge, B. D'Anna, L. Mazri, A. Giroir-Fendler, M. Ammann, D. Donaldson, and C. George, "Light changes the atmospheric reactivity of soot." Proceedings of the National Academy of Sciences, 2009. Special feature.

[9] O. Mathieu, *Etude cinétique de la formation des particules de suie dans les conditions de fonctionnement des moteurs automobile*. PhD thesis, Université d'Orléans, 2006.

[10] A. Makri and N. I. Stilianakis, "Vulnerability to air pollution health effects," *International Journal of Hygiene and Environmental Health*, vol. 211, pp. 326–336, 2008.

[11] E. Commission, "EU - Transport and Environment." `http://ec.europa.eu/environment/air/transport/road.htm`, 2008.

[12] N. Bafman, "Polluer nuit gravement à la santé," *Le Monde*, vol. 19 August, 2009.

[13] R. Chang and A. Violi, "Insights into the Effect of Combustion-Generated Carbon Nano-Particles on Biological Membranes: A Computer Simulation Study," *Journal of Physical Chemistry B*, vol. 110, pp. 5073–5083, 2006.

[14] N. Farah, "Soot: A global warming emission." Presentation at Task Force on Hemispheric Transport of Air Pollution (TF HTAP) Meeting, 2009.

[15] M. Z. Jacobson, "Control of fossil-fuel particulate black carbon and organic matter, possibly the most effective method of slowing global warming," *Journal of Geophysical Research*, vol. 107, pp. 16–1–16–22, 2002.

[16] D. Shindell and G. Faluvegi, "Climate response to regional radiative forcing during the twentieth century," *Nature Geoscience*, vol. 2, pp. 294–300, 2009.

[17] F. Monforti, R. Bellasio, R. Bianconi, G. Clai, and G. Zanini, "An evaluation of particle deposition fluxes to cultural heritage sites in Florence, Italy," *Science of the Total Environment*, vol. 334–335, pp. 61–72, 2004.

[18] R. van Grieken, K. Gysels, P. Hoornaert, P. Joos, I. Szaloki, and A. Worobiec, "Characterisation of individual aerosol particles for atmospheric and cultural heritage studies," *Water, Air and Soil Pollution*, vol. 123, pp. 215–228, 2000.

[19] E. Inc., "DieselNet Technology Guide - Diesel Particulate Filters." `www.DieselNet.com`, 2001.

[20] F. Piscaglia, C. Rutland, and D. Foster, "Development of a CFD Model to Study the Hydrodynamic Characteristics and the Soot Deposition Mechanism on the Porous Wall of a Diesel Particulate Filter," *SAE*, vol. 2005-01-0963.

[21] M. Issa, *Etude théorique et expérimentale de l'oxydation catalytique du noir de carbone: Influence du contact entre solides.* PhD thesis, Université de Haute Alsace, 2008.

[22] C. N. Millet, P. Menegazzi, B. Martin, and H. Colas, "Modélisation de la régénération du filtre à particules Diesel : effet de l'additif," *Oil & Gas Science and Technology - Rev. IFP*, vol. 58, no. 1, pp. 151–162, 2003.

[23] T. Deuschle, *Untersuchung von Beladungs-, Regenerations- und Ascheeinlagerungsprozessen in Dieselruß-Partikelfiltern von Kraftfahrzeugen.* PhD thesis, Universität Stuttgart, 2008.

[24] D. Fino and V. Specchia, "Open issues in oxidative catalysis for diesel particulate abatement," *Powder Technology*, vol. 180, pp. 64–73, 2008.

[25] O. Senneca, P. Salatino, and D. Menghini, "The influence of thermal annealing on oxygen uptake and combustion rates of a bituminious coal char," *Proceedings of the Combustion Institute*, vol. 31, pp. 1889–1895, 2007.

[26] P. B. Weisz and R. Goodwin, "Combustion of Carbonaceous Deposits within Porous Catalyst Particles I. Diffusion-Controlled Kinetics," *Journal of Catalysis*, vol. 2, pp. 397–404, 1963.

[27] H. Chelliah, A. Makino, I. Kato, N. Araki, and C. Law, "Modeling of Graphite Oxidation in a Stagnation-Point Flow Field Using Detailed Homogeneous and Semiglobal Heterogeneous Mechanisms with Comparisons to Experiments," *Combustion and Flame*, vol. 104, pp. 469–480, 1996.

[28] C. Depcik and D. Assanis, "One-demensional automative catalyst modeling," *Progress in Energy and Combustion Science*, vol. 31, pp. 308–369, 2005.

[29] "Eberspächer and Fluent Developing CFD Technology to Design Automotive Diesel Filters," 2006. Fluent Inc.

[30] B. Stanmore, V. Tschamber, and J.-F. Brilhac, "Oxidation of carbon by NO_x, with particular reference to NO_2 and N_2O," *Fuel*, vol. 87, pp. 131–146, 2008.

[31] G. Miessen, F. Behrendt, O. Deutschmann, and J. Warnatz, "Numerical studies of the heterogeneous combustion of char using detailed chemistry," *Chemosphere*, vol. 42, pp. 609–613, 2001.

[32] G. Miessen, *Simulation der Koksverbrennung unter Verwendung detaillierter Reaktionsmechanismen*. PhD thesis, Ruprecht-Karls-Universität Heidelberg, 2000.

[33] F. Jacquot, V. Logie, J. F. Brilhac, and P. Gilot, "Kinetics of the oxidation of carbon black by NO_2: Influence of the presence of water and oxygen," *Carbon*, vol. 40, no. 3, pp. 335 – 343, 2002.

[34] I. Smith and D. Harris, *Fundamental Issues in Control of Carbon Gasification Reactivity*, pp. 49–77. Kluwer Academic Publishers, 1991.

[35] J. P. Neeft, X. Nijhuis, E. Smakman, M. Makkee, and J. A. Moulijn, "Kinetics of the oxidation of diesel soot," *Fuel*, vol. 76, no. 12, pp. 1129–1136, 1997.

[36] A. Yezerets, N. W. Currier, H. A. Eadler, A. Suresh, P. F. Madden, and M. A. Branigin, "Investigation of the oxidation behavior of diesel particulate matter," *Catalysis Today*, vol. 88, no. 1-2, pp. 17 – 25, 2003.

[37] P. Darcy, *Modélisation du fonctionnement d'un filtre à particules catalysé*. PhD thesis, Université Pierre et Marie Curie (Paris VI), 2005.

[38] R. H. Hurt and J. M. Calo, "Semi-Global Intrinsic Kinetics for Char Combustion Modeling," *Combustion and Flame*, vol. 125, pp. 1138–1149, 2001.

[39] B. Stanmore, J.-F. Brilhac, and P. Gilot, "The oxidation of soot: a review of experiments, mechanisms and models," *Carbon*, vol. 39, pp. 2247–2268, 2001.

[40] R. Backreedy, J. M. Jones, M. Pourkashanian, and A. Williams, "A study of the reaction of oxygen with graphite: Model chemistry," *Faraday Discussions*, vol. 119, pp. 385–394, 2001.

[41] Z. Du, A. F. Sarofim, and J. P. Longwell, "Activation Energy Distribution in Temperature-Programmed Desorption: Modeling and Application to the Soot-Oxygen System," *Energy & Fuels*, vol. 4, pp. 214–221, 1990.

[42] P. Campbell and R. Mitchell, "The impact of the distributions of surface oxides and their migration on characterization of the heterogeneous carbon-oxygen reaction," *Combustion and Flame*, vol. 154, pp. 47–66, 2008.

[43] L. Retailleau, R. Vonarb, V. Perrichon, E. Jean, and D. Bianchi, "Catalytic oxidation of a diesel soot formed in the presence of a cerium additive. i. characterization of the cerium fraction using magnetic susceptibility and temperature-programmed desorption," *Energy & Fuels*, vol. 18, no. 3, pp. 872–882, 2004.

[44] J. Arthur, "Reactions between carbon and oxygen," *Transactions of the Faraday Society*, vol. 7, pp. 164–178, 1950.

[45] L. R. Radovic, "Active Sites in Graphene and the Mechanism of CO_2 Formation in Carbon Oxidation," *Journal of the American Chemical Society*, vol. 131, no. 47, pp. 17166–17175, 2009.

[46] A. Montoya, F. Mondragón, and T. N. Truong, "Formation of CO precursors during char gasification with O_2, CO_2 and H_2O," *Fuel Processing Technology*, vol. 77–78, pp. 125–130, 2002.

[47] A. Sadezky, H. Muckenhuber, H. Grothe, R. Niessner, and U. Poschl, "Raman microspectroscopy of soot and related carbonaceous materials: Spectral analysis and structural information," *Carbon*, vol. 43, no. 8, pp. 1731 – 1742, 2005.

[48] C. A. Amann and D. C. Siegla, "Diesel Particulates - What They Are and Why," *Aerosol Science and Technology*, vol. 1: 1, pp. 73–101, 1981.

[49] M. Alfè, B. Apicella, R. Barbella, J.-N. Rouzaud, A. Tregrossi, and A. Ciajolo, "Structure-property relationship in nanostructures of young and mature soot in premixed flames," *Proceedings of the Combustion Institute*, vol. 32, pp. 697–704, 2009.

[50] E. Fitzer, K.-H. Kochling, H. Boehm, and H. Marsh, "Recommended terminology for the description of carbon as a solid," *Pure and Applied Chemistry*, vol. 3, pp. 473–506, 1995.

[51] N. M. Laurendeau, "Heterogeneous kinetics of coal char gasification and combustion," *Progress in Energy and Combustion Science*, vol. 4, pp. 221–270, 1978.

[52] J. M. Jones and D. H. Jones, "Modelling the competition between annealing and oxidation in the carbon-oxygen reaction," *Letters to the Editor / Carbon*, vol. 45, pp. 668–689, 2007.

[53] O. Aubry, *Etude des précurseurs gazeux de couches minces en carbone déposées á partir de phases gazeuses activées thermiquement et par plasma*. PhD thesis, Université d'Orléans, 2002.

[54] W. F. Wells and L. D. Smoot, "Relation between reactivity and structure for coals and chars," *Fuel*, vol. 70, pp. 454–458, 1991.

[55] S. Niksa, G.-S. Liu, and R. H. Hurt, "Coal conversion submodels for design applications at elevated pressures. Part I. Devolatilization and char oxidation," *Progress in Energy and Combustion Science*, vol. 29, pp. 425–477, 2003.

[56] G.-S. Liu and S. Niksa, "Coal conversion submodels for design applications at elevated pressures. Part II. Char gasification," *Progress in Energy and Combustion Science*, vol. 30, pp. 679–717, 2004.

[57] R. L. Vander Wal and A. J. Tomasek, "Soot oxidation: dependence upon initial nanostructure," *Combustion and Flame*, vol. 134, pp. 1–9, 2003.

[58] M. Ruiz, R. Guzmán de Villoria, A. Millera, M. Alzueta, and R. Bilbao, "Influence of the temperature on the properties of the soot formed from C_2H_2 pyrolysis," *Chemical Engineering Journal*, vol. 127, pp. 1–9, 2007.

[59] T. Ishiguro, N. Suzuki, Y. Fujitani, and H. Morimoto, "Microstructural Changes of Diesel Soot During Oxidation," *Combustion and Flame*, vol. 85, pp. 1–6, 1991.

[60] M. Knauer, M. E. Schuster, D. Su, R. Schlogl, R. Niessner, and N. P. Ivleva, "Soot Structure and Reactivity Analysis by Raman Microspectroscopy,

Temperature-Programmed Oxidation and High-Resolution Transmission Electron Microscopy," *The Journal of Physical Chemistry*, vol. 113, pp. 13871–13880, 2009.

[61] H. Jung, D. B. Kittleson, and M. R. Zachariah, "The Influence of Engine Lubricating Oil on Diesel Nanoparticle Emissions and Kinetics of Oxidation," *SAE*, vol. 2003-01-3179.

[62] R. J. Berger, F. Kapteijn, J. A. Moulijn, G. B. Marin, J. De Wilde, M. Olea, D. Chen, A. Holmen, L. Lietti, E. Tronconi, and Y. Schuurman, "Dynamic methods for catalytic kinetics," *Applied Catalysis A: General*, vol. 342, pp. 3–28, 2008.

[63] R. J. Berger, E. H. Stitt, G. B. Marin, F. Kapteijn, and J. A. Moulijn, "Chemical reaction kinetics in practice," *CatTech*, vol. 5, pp. 30–60, 2001.

[64] D. Schweich, *Génie de la réaction chimique*. Lavoisier Tec & Doc, 2001.

[65] S. Bhatia and D. Perlmutter, "A Random Pore Model for Fluid-Solid Reactions: I. Isothermal, Kinetic Control," *AIChE Journal*, vol. 26, No. 3, pp. 379–386, 1980.

[66] S. Bhatia and D. Perlmutter, "A Random Pore Model for Fluid-Solid Reactions: II. Diffusion and Transport Effects," *AIChE Journal*, vol. 27, No. 2, pp. 247–254, 1981.

[67] E. M. Suuberg and I. Aarna, "Kinetics of tire derived fuel (TDF) char oxidation and accompanying changes in surface area," *Fuel*, vol. 88, pp. 179–186, 2009.

[68] J. Lahaye, J. Dentzer, P. Soulard, and P. Ehrburger, "Fundamental Issues in Control of Carbon Gasification Reactivity," pp. 143–162, Kluwer Academic Publishers, 1991.

[69] L. Radovic, A. Lizzio, and H. Jiang in *Fundamental Issues in Control of Carbon Gasification Reactivity* (J. Lahaye and P. Ehrburger, eds.), pp. 235–255, Kluwer Academic Publishers, 1991.

[70] B. McEnaney, "Fundamental Issues in Control of Carbon Gasification Reactivity," pp. 175–203, Kluwer Academic Publishers, 1991.

[71] A. Trovarelli, ed., *Catalysis by Ceria and Related Materials*. Imperial College Press, 2002.

[72] C. Mims, "Fundamental Issues in Control of Carbon Gasification Reactivity," pp. 383–407, Kluwer Academic Publishers, 1991.

[73] M. S. Gross, M. A. Ulla, and C. A. Querini, "catalytic oxidation of diesel soot: New characterization and kinetic evidence related to the reaction mechanism on K/CeO_2 catalyst," *Applied Catalysis A: General*, vol. 360, pp. 81–88, 2009.

[74] R. Backreedy, J. M. Jones, M. Pourkashanian, and A. Williams, "Modeling the reaction of oxygen with coal and biomass chars," *Proceedings of the Combustion Institute*, vol. 29, pp. 415–422, 2002.

[75] A. Bueno-Lopéz, K. Krishna, B. van der Linden, G. Mul, J. Moulijn, and M. Makkee, "On the mechanism of model diesel soot-O_2 reaction catalysed by Pt-containing La^{3+}-doped CeO_2. A TAP study with isotopic O_2," *Catalysis Today*, vol. 121, pp. 237–245, 2007.

[76] M. Issa, H. Mahzoul, A. Brillard, J.-F. Brilhac, and C. Petit, "Effect of the contact between carbon black and catalyst particles on carbon oxidation rate: Experiments and modelling," in - *8th ICE Naples*, SAE International, 2007.

[77] M. Issa, A. Brillard, J.-F. Brilhac, and C. Petit, "Oxidation of carbon by CeO_2: Effect of the contact between carbon black and catalyst particles," *Fuel*, vol. 87, pp. 740–750, 2008.

[78] A. Bueno-Lopéz, K. Krishna, B. van der Linden, G. Mul, J. Moulijn, and M. Makkee, "On the mechanism of model diesel soot-O_2 reaction catalysed by Pt-containing La^{3+}-doped CeO_2. A TAP study with isotopic O_2," *Catalysis Today*, vol. 121, pp. 237–245, 2007.

[79] W. C. Conner and J. L. Falconer, "Spillover in heterogeneous catalysis," *Chemical Reviews*, vol. 95, no. 3, pp. 759–788, 1995.

[80] M. Jeguirim, V. Tschamber, and P. Ehrburger, "Catalytic effect of platinum on the kinetics of carbon oxidation by NO_2 and O_2," *Aplied Catalysis B: Environmental*, vol. 76, pp. 235–240, 2007.

[81] E. Aneggi, C. de Leitenburg, G. Dolcetti, and A. Trovarelli, "Diesel soot combustion activity of ceria promoted with alkali metals," *Catalysis Today*, vol. 136, pp. 3–10, 2008.

[82] I. Atribak, B. Azambre, A. Bueno-López, and A. García-García, "Effect of NO_x adsdorption/desorption over ceria-zirconia catalysts on the catalytic combustion of model soot," *Applied Catalysis B: Environmental*, vol. 92, pp. 126–137, 2009.

[83] J. E. House, *Principles of Chemical Kinetics*. Academic Press, 2007.

[84] N. Lamharess, C.-N. Millet, L. Starck, E. Jeudy, J. Lavy, and P. D. Costa, "Catalysed diesel particulate filter: Study of the reactivity of soot arising from biodiesel combustion," *Catalysis Today*, vol. In Press, Corrected Proof, pp. –, 2011.

[85] C. Tighe, M. Twigg, A. Hayhurst, and J. Dennis, "The kinetics of oxidation of Diesel soots by NO_2," *Combustion and Flame*, vol. In Press, Corrected Proof, 2011.

[86] L. Olsson, H. Persson, E. Fridell, M. Skoglundh, and B. Andersson, "A Kinetic Study of NO Oxidation and NO_x Storage on Pt/Al_2O_3 and $Pt/BaO/Al_2O_3$," *The Journal of Physical Chemistry B*, vol. 105, no. 29, pp. 6895–6906, 2001.

[87] N. Rankovic, A. Nicolle, and P. Da Costa, "Detailed Kinetic Modeling Study of NO_x Oxidation and Storage and Their Interactions over $Pt/Ba/Al_2O_3$ Monolith Catalysts," *Journal of Physical Chemistry C*, vol. 114, no. 15, pp. 7102–7111, 2010.

[88] K. Leistner, A. Nicolle, D. Berthout, and P. D. Costa, "Kinetic modelling of the oxidation of a wide range of carbon materials," *Combustion and Flame*, vol. 159, no. 1, pp. 64–76, 2012.

[89] M. Jeguirim, V. Tschamber, J. Brilhac, and P. Ehrburger, "Interaction mechanism of NO_2 with carbon black: effect of surface oxygen complexes," *Journal of Analytical and Applied Pyrolysis*, vol. 72, pp. 171–181, 2004.

[90] K. Leistner, A. Nicolle, and P. Da Costa, "Detailed Kinetic Analysis of Soot Oxidation by NO_2, NO, and NO + O_2," *The Journal of Physical Chemistry C*, vol. 116, no. 7, pp. 4642–4654, 2012.

[91] J. Villermaux, *Génie de la réaction chimique. Conception et fonctionnement des réacteurs.* Lavoisier Tec & Doc, 1993.

[92] P. Wellstead, *Introduction to Physical System Modelling.* Academic Press Ltd, 1979.

[93] B. Bouteiller, *Etude théorique et expérimentale des filtres à particules à substrat céramique pour moteur Diesel. Application à une nouvelle géométrie de cellules.* PhD thesis, Université d'Orléans, 2006.

[94] K. Yamamoto, N. Takada, and M. Misawa, "Combustion simulation with Lattice-Boltzmann method in a three-dimensional porous structure," *Proceedings of the Combustion Institute*, vol. 30, pp. 1509–1515, 2005.

[95] L. Oxarango, *Transferts de Chaleur et de Masse dans des structures poreuses multi-échelles*. PhD thesis, Institut de Mécanique des Fluides de Toulouse, 2004.

[96] M. Matyka, A. Khalili, and Z. Koza, "Tortuosity-porosity relation in the porous media flow," *Physical Review E*, vol. 78, no. 2, p. 026306, 2008.

[97] J. Kanervo, A. Krause, J. Aittamaa, P. Hagelberg, K. Lipiainen, I. Eilos, J. Hiltunen, and V. Niemi, "Kinetics of the regeneration of a cracking catalyst derived from TPO measurements," *Chemical Engineering Science*, vol. 56, pp. 1221–1227, 2001.

[98] R. E. Mitchell, "An intrinsic kinetics-based, particle-population balance model for char oxidation during pulverized coal combustion," *Proceedings of the Combustion Institute*, vol. 28, no. 2, pp. 2261 – 2270, 2000.

[99] L. Chan, A. Sarofim, and J. Beér, "Kinetics of the NO-carbon reaction at fluidized bed combustor conditions," *Combustion and Flame*, vol. 52, no. 0, pp. 37–45, 1983.

[100] H. Teng and E. M. Suuberg, "Chemisorption of nitric oxide on char. 1. reversible nitric oxide sorption," *The Journal of Physical Chemistry*, vol. 97, no. 2, pp. 478–483, 1993.

[101] H. Muckenhuber and H. Grothe, "The heterogeneous reaction between soot and NO_2 at elevated temperature," *Carbon*, vol. 44, no. 3, pp. 546 – 559, 2006.

[102] T. Okuhara and K.-i. Tanaka, "Adsorption and reduction of nitrogen monoxide by potassium-doped carbon," *Journal of the Chemical Society, Faraday Transactions 1*, vol. 82, pp. 3657–3666, 1986.

[103] P. Chambrion, T. Suzuki, Z.-G. Zhang, T. Kyotani, and A. Tomita, "Xps of nitrogen-containing functional groups formed during the c-no reaction," *Energy & Fuels*, vol. 11, no. 3, pp. 681–685, 1997.

[104] P. Chambrion, H. Orikasa, T. Suzuki, T. Kyotani, and A. Tomita, "A study of the C-NO reaction by using isotopically labelled C and NO," *Fuel*, vol. 76, no. 6, pp. 493–498, 1997.

[105] H. Teng, E. M. Suuberg, and J. M. Calo, "Studies on the reduction of nitric oxide by carbon: the nitric oxide-carbon gasification reaction," *Energy & Fuels*, vol. 6, no. 4, pp. 398–406, 1992.

[106] M. S. Akhter, A. R. Chughtai, and D. M. Smith, "Reaction of hexane soot with nitrogen dioxide/nitrogen oxide (n_2o_4)," *The Journal of Physical Chemistry*, vol. 88, no. 22, pp. 5334–5342, 1984.

[107] Kalberer, M. and Tabor, K. and Ammann, M. and Parrat, Y. and Weingartner, E. and Piguet, D. and Rössler, E. and Jost, D. T. and Türler, A. and Gäggeler, H. W. and Baltensperger, U., "Heterogeneous chemical processing of 13no$_2$ by monodisperse carbon aerosols at very low concentrations," *The Journal of Physical Chemistry*, vol. 100, no. 38, pp. 15487–15493, 1996.

[108] M. J. Illán-Gómez, A. Linares-Solano, L. Radovic, and C. Salinas-Martínez de Lecea, "NO Reduction by Activated Carbons. 7. Some Mechanistic Aspects of Uncatalyzed and Catalyzed Reaction," *Energy & Fuels*, vol. 10, no. 1, pp. 158–168, 1996.

[109] B. Azambre, S. Collura, J. Trichard, and J. Weber, "Nature and thermal stability of adsorbed intermediates formed during the reaction of diesel soot with nitrogen dioxide," *Applied Surface Science*, vol. 253, no. 4, pp. 2296 – 2303, 2006.

[110] O. Deutschmann, "Interactions between transport and chemistry in catalytic reactors," 2001. Habilitation thesis.

[111] M. Coltrin, R. Kee, and F. Rupley, "Surface Chemkin (Version 4.0): A Fortran Package for Analyzing Heterogeneous Chemical Kinetics at a Solid-Surface - Gas-Phase Interface," Report SAND90-8003B, Sandia National Laboratories, 1990.

[112] T. Alvarez, A. B. Fuertes, J. J. Pis, and P. Ehrburger, "Influence of coal oxidation upon char gasification reactivity," *Fuel*, vol. 74, no. 5, pp. 729 – 735, 1995.

[113] C. Schonenbeck, R. Gadiou, and D. Schwartz, "A kinetic study of the high temperature NO-char reaction," *Fuel*, vol. 83, no. 4-5, pp. 443 – 450, 2004.

[114] Y. H. Li, L. R. Radovic, G. Q. Lu, and V. Rudolph, "A new kinetic model for the NO-carbon reaction," *Chemical Engineering Science*, vol. 54, no. 19, pp. 4125 – 4136, 1999.

[115] H. Wang, B. Dlugogorski, and E. M. Kennedy, "Coal oxidation at low temperatures: oxygen consumption, oxidation products, reaction mechanism and kinetic modelling," *Progress in Energy and Combustion Science*, vol. 29, pp. 487–513, 2003.

[116] R. Dittmeyer and G. Emig, *Simultaneous Heat and Mass Transfer and Chemical Reaction. Handbook of Heterogeneous Catalysis*, pp. 1727–1784. Wiley-VCH Verlag GmbH & Co. KGaA, 2008.

[117] R. C. Reid, J. M. Prausnitz, and T. K. Sherwood, *The Properties of Gases and Liquids*. McGraw-Hill Book Company, 1958.

[118] E. Mason and A. Malinauskas, *Gas transport in porous media: The dusty-gas model*. Elsevier, 1983.

[119] K. B. Bischoff, "Effectiveness factors for general reaction rate forms," *AIChE Journal*, vol. 11, no. 2, pp. 351–355, 1965.

[120] J. Hong, *Modelling char oxidation as a funtion of pressure using an intrinsic Langmuir rate equation*. PhD thesis, Brigham Young University, 2000.

[121] I. P. Kandylas, O. A. Haralampous, and G. C. Koltsakis, "Diesel soot oxidation with no_2: Engine experiments and simulations," *Industrial & Engineering Chemistry Research*, vol. 41, no. 22, pp. 5372–5384, 2002.

[122] I. P. Kandylas and G. C. Koltsakis, "No_2-assisted regeneration of diesel particulate filters: A modeling study," *Industrial & Engineering Chemistry Research*, vol. 41, no. 9, pp. 2115–2123, 2002.

[123] T. Mendiara, M. Alzueta, A. Millera, and R. Bilbao, "Acetylene soot reaction with NO in the presence of CO," *Journal of Hazardous Materials*, vol. 166, no. 2-3, pp. 1389–1394, 2009.

[124] I. Aarna and E. M. Suuberg, "The role of carbon monoxide in the no-carbon reaction," *Energy & Fuels*, vol. 13, no. 6, pp. 1145–1153, 1999.

[125] P. García, F. Coloma, C. S. M. de Lecea, and F. Mondragón, "Nitrogen complexes formation during NO-C reaction at low temperature in presence of O_2 and H_2O," *Fuel Processing Technology*, vol. 77-78, no. 0, pp. 255–259, 2002.

[126] C. Arnal, M. U. Alzueta, A. Millera, and R. Bilbao, "Experimental and kinetic study of the interaction of a comemrcial soot toward NO at high temperature," *Proceedings of the Seventh Mediterranean Combustion Symposium (MCS-7)*, 2011.

[127] K. Noda, P. Chambrion, T. Kyotani, and A. Tomita, "A study of the n_2 formation mechanism in carbon-n_2o reaction by using isotope gases," *Energy & Fuels*, vol. 13, no. 4, pp. 941–946, 1999.

[128] C. J. Tighe, J. S. Dennis, A. N. Hayhurst, and M. V. Twigg, "The reactions of NO with diesel soot, fullerene, carbon nanotubes and activated carbons doped with transition metals," *Proceedings of the Combustion Institute*, vol. 32, pp. 1989–1996, 2009.

[129] C. J. Tighe, M. V. Twigg, A. N. Hayhurst, and J. S. Dennis, "Adsorption and Reaction of NO_2 on Carbon Black and Diesel Soot at Near-Ambient Temperatures," *Industrial & Engineering Chemistry Research*, 2011.

[130] C. Pevida, A. Arenillas, F. Rubiera, and J. Pis, "Synthetic coal chars for the elucidation of NO heterogeneous reduction mechanisms," *Fuel*, vol. 86, no. 1-2, pp. 41–49, 2007.

[131] K.-Y. Choi, N. W. Cant, and D. L. Trimm, "Gasification of carbonaceous particulates," *Journal of Chemical Technology & Biotechnology*, vol. 71, no. 1, pp. 57–60, 1998.

[132] C. Esarte, A. Callejas, A. Millera, R. Bilbao, and M. U. Alzueta, "Characterization and reactivity with NO/O_2 of the soot formed in the pyrolysis of acetylene-ethanol mixtures," *Journal of Analytical and Applied Pyrolysis*, no. 0, pp. –, 2011. in press, 10.1016/j.jaap.2011.11.004.

[133] T. Mendiara, M. U. Alzueta, A. Millera, and R. Bilbao, "A Comparison of Acetylene Soot and Two Different Carbon Blacks: Reactivity to Oxygen and NO," *International Journal of Chemical Reactor Engineering*, vol. 5, pp. 1–15, 2007.

[134] A. Setiabudi, M. Makkee, and J. A. Moulijn, "The role of NO_2 and O_2 in the accelerated combustion of soot in diesel exhaust gases," *Applied Catalysis B: Environmental*, vol. 50, no. 3, pp. 185 – 194, 2004.

[135] P. Chambrion, T. Kyotani, and A. Tomita, "Role of N-Containing Surface Species on NO Reduction by Carbon," *Energy & Fuels*, vol. 12, no. 2, pp. 416–421, 1998.

[136] H. Teng and E. M. Suuberg, "Chemisorption of nitric oxide on char. 2. irreversible carbon oxide formation," *Industrial & Engineering Chemistry Research*, vol. 32, no. 3, pp. 416–423, 1993.

[137] M. J. llán Gómez, A. Linares-Solano, C. Salinas-Martínez de Lecea, and J. M. Calo, "Nitrogen oxide (NO) reduction by activated carbons. 1. The role of carbon porosity and surface area," *Energy & Fuels*, vol. 7, no. 1, pp. 146–154, 1993.

[138] I. Aarna and E. M. Suuberg, "A review of the kinetics of the nitric oxide-carbon reaction," *Fuel*, vol. 76, no. 6, pp. 475 – 491, 1997.

[139] J. Yang, G. Mestl, d. Herein, R. Schlogl, and J. Find, "Reaction of NO with carbonaceous materials: 1. Reaction and adsorption of NO on ashless carbon black," *Carbon*, vol. 38, no. 5, pp. 715–727, 2000.

[140] J. Yang, G. Mestl, d. Herein, R. Schlogl, and J. Find, "Reaction of NO with carbonaceous materials: 2. Effect of oxygen on the reaction of NO with ashless carbon black," *Carbon*, vol. 38, no. 5, pp. 729–740, 2000.

[141] T. Mendiara, M. U. Alzueta, A. Millera, and R. Bilbao, "Influence of the no concentration and the presence of oxygen in the acetylene soot reaction with no," *Energy & Fuels*, vol. 22, no. 1, pp. 284–290, 2008.

[142] T. Suzuki, T. Kyotani, and A. Tomita, "Study on the Carbon-Nitric Oxide Reaction in the Presence of Oxygen," *Industrial & Engineering Chemistry Research*, vol. 33, no. 11, pp. 2840–2845, 1994.

[143] S. Kureti, W. Weisweiler, and K. Hizbullah, "Simultaneous conversion of nitrogen oxides and soot into nitrogen and carbon dioxide over iron containing oxide catalysts in diesel exhaust gas," *Applied Catalysis B: Environmental*, vol. 43, no. 3, pp. 281 – 291, 2003.

[144] J. Zawadzki, M. Wisniewski, and K. Skowronska, "Heterogeneous reactions of NO_2 and NO-O_2 on the surface of carbons," *Carbon*, vol. 41, no. 2, pp. 235 – 246, 2003.

[145] H. Muckenhuber and H. Grothe, "A DRIFTS study of the heterogeneous reaction of NO_2 with carbonaceous materials at elevated temperature," *Carbon*, vol. 45, no. 2, pp. 321–329, 2007.

[146] U. Kirchner, V. Scheer, and R. Vogt, "Ftir spectroscopic investigation of the mechanism and kinetics of the heterogeneous reactions of no_2 and hno_3 with soot," *The Journal of Physical Chemistry A*, vol. 104, no. 39, pp. 8908–8915, 2000.

[147] I. W. Smith, "The intrinsic reactivity of carbons to oxygen," *Fuel*, vol. 57, pp. 409 – 414, 978.

[148] Z. H. Zhu, J. Finnerty, G. Q. Lu, and R. T. Yang, "Opposite Roles of O_2 in NO and N_2O-Carbon Reactions: An Ab Initio Study," *The Journal of Physical Chemistry B*, vol. 105, no. 4, pp. 821–830, 2001.

[149] T. Kyotani and A. Tomita, "Analysis of the reaction of carbon with no/n_2o using ab initio molecular orbital theory," *The Journal of Physical Chemistry B*, vol. 103, no. 17, pp. 3434–3441, 1999.

[150] Y. Kong and C. Y. Cha, "NO_x adsorption on char in presence of oxygen and moisture," *Carbon*, vol. 34, no. 8, pp. 1027 – 1033, 1996.

[151] A. Tomita, "Suppression of nitrogen oxides emission by carbonaceous reductants," *Fuel Processing Technology*, vol. 71, no. 1-3, pp. 53–70, 2001.

[152] M. Guerrero, A. Millera, M. U. Alzueta, and R. Bilbao, "Experimental and kinetic study at high temperatures of the no reduction over eucalyptus char produced at different heating rates," *Energy & Fuels*, vol. 25, no. 3, pp. 1024–1033, 2011.

[153] J. Kanervo, T. Keskitalo, R. Slioor, and A. Krause, "Temperature-programmed desorption as a tool to extract quantitative kinetic or energetic information for porous catalysts," *Journal of Catalysis*, vol. 238, no. 2, pp. 382–393, 2006.

[154] J. A. Dumesic, D. F. Rudd, L. M. Aparicio, J. E. Rekoske, and A. Trevino, *The Microkinetics of Heterogeneous Catalysis*. American Chemical Society, 1993.

[155] C. Querini, "Coke Characterization," in *Catalysis* (J. J. Spivey and G. Roberts, eds.), vol. 17, ch. 4, pp. 166–176, The Royal Society of Chemistry, 2004.

[156] R. H. Hurt, "Structure, properties, and reactivity of solid fuels," *Symposium (International) on Combustion*, vol. 27, no. 2, pp. 2887–2904, 1998.

[157] A. Williams, M. Pourkashanian, and J. M. Jones, "Combustion of pulverised coal and biomass," *Progress in Energy and Combustion Science*, vol. 27, no. 6, pp. 587 – 610, 2001.

[158] A. Messerer, R. Niessner, and U. Poschl, "Comprehensive kinetic characterization of the oxidation and gasification of model and real diesel soot by nitrogen oxides and oxygen under engine exhaust conditions: Measurement, Langmuir-Hinshelwood, and Arrhenius parameters," *Carbon*, vol. 44, no. 2, pp. 307 – 324, 2006.

[159] A. D. H. Clague, J. B. Donnet, T. K. Wang, and J. C. M. Peng, "A comparison of diesel engine soot with carbon black," *Carbon*, vol. 37, no. 10, pp. 1553 – 1565, 1999.

[160] L. R. Radovic, P. L. Walker, and R. G. Jenkins, "Importance of carbon active sites in the gasification of coal chars," *Fuel*, vol. 62, no. 7, pp. 849 – 856, 1983.

[161] R. L. Vander Wal, V. M. Vryg, and M. D. Hays, "Fingerprinting soot (towards source identification): Physical structure and chemical composition," *Journal of Aerosol Science*, vol. 41, no. 1, pp. 108 – 117, 2010. Special Issue for the 9th International Conference on Carbonaceous Particles in the Atmosphere.

[162] A. Molina, E. Eddings, D. Pershing, and A. Sarofim, "Char nitrogen conversion: implications to emissions from coal-fired utility boilers," *Progress in Energy and Combustion Science*, vol. 26, no. 4-6, pp. 507–531, 2000.

[163] K. J. Lee, "Modeling of Oygen Chemisorption in Microporous Carbons," *Journal of Industrial and Engineering Chemistry*, vol. 2, pp. 33–39, 1996.

[164] P. Burg and D. Cagniant, "Characterization of Carbon Surface Chemistry," in *Chemistry and Physics of Carbon* (L. R. Radovic, ed.), vol. 30, ch. 3, pp. 129–176, CRC Press, Taylor & Francis Group, 2008.

[165] J. Ranish and P. Walker, "High pressure studies of the carbon-oxygen reaction," *Carbon*, vol. 31, no. 1, pp. 135 – 141, 1993.

[166] B. S. Haynes and T. G. Newbury, "Oxyreactivity of carbon surface oxides," *Proceedings of the Combustion Institute*, vol. 28, no. 2, pp. 2197 – 2203, 2000.

[167] A. M. Nienow and J. T. Roberts, "Heterogeneous chemistry of carbon aerosols," *Annual Review of Physical Chemistry*, vol. 57, no. 1, pp. 105–128, 2006.

[168] I. P. Kandylas and A. M. Stamatelos, "Modeling Catalytic Regeneration of Diesel Particulate Filters, Taking into Account Adsorbed Hydrocarbon Oxidation," *Industrial & Engineering Chemistry Research*, vol. 38, no. 5, pp. 1866–1876, 1999.

[169] G. C. Koltsakis and A. M. Stamatelos, "Catalytic automotive exhaust aftertreatment," *Progress in Energy and Combustion Science*, vol. 23, no. 1, pp. 1 – 39, 1997.

[170] N. Laine, F. Vastola, and P. Walker, "The importance of active surface area in the carbon-oxygen reaction," *Journal of Physical Chemistry*, vol. 67, pp. 2030 – 2034, 1963.

[171] J. Lahaye and P. Ehrburger, "Surface chemistry of carbon: an atomistic approach," *Pure and Applied Chemistry*, vol. 61, pp. 1853 – 1858, 1989.

[172] E. M. Suuberg, H. Teng, and J. M. Calo, "Studies on the kinetics and mechanism of the reaction of NO with carbon," *Symposium (International) on Combustion*, vol. 23, no. 1, pp. 1199 – 1205, 1991. Twenty-Third Symposium (International) on Combustion.

[173] Z. Du, A. F. Sarofim, J. P. Longwell, and C. A. Mims, "Kinetic Measurement and Modeling of Carbon Oxidation," *Energy & Fuels*, vol. 5, pp. 296–302, 1991.

[174] C. Li and T. C. Brown, "Carbon oxidation kinetics from evolved carbon oxide analysis during temperature-programmed oxidation," *Carbon*, vol. 39, pp. 725–732, 2001.

[175] J.-M. Commandré, *Formation des oxydes d'azote lors de la combustion de cokes de pétrole dans des conditions de précalcinateur de cimenterie*. PhD thesis, L'Institut National Polytechnique de Toulouse, 2002.

[176] J.-M. Commandré and S. Salvador, "Lack of correlation between the properties of a petroleum coke and its behaviour during combustion," *Fuel Processing Technology*, vol. 86, pp. 795–808, 2005.

[177] C. L. Senior and R. C. Flagan, "Synthetic chars for the study of ash vaporization," *Symposium (International) on Combustion*, pp. 921–929, 1984.

[178] A. Hayhurst and M. Parmar, "Does solid carbon burn in oxygen to give the gaseous intermediate CO or produce CO_2 directly? Some experiments in a hot bed of sand fluidized by air," *Chemical Engineering Science*, pp. 427–438, 1997.

[179] K. A. Skokova, *Selectivity in the carbon-oxygen reaction.* PhD thesis, Pennsylvania State University, 1997.

[180] R. H. Hurt and R. E. Mitchell, "Unified High-temperature Char Combustion Kinetics for a Suite of Coals of Various Rank," *Symposium (International) on Combustion*, vol. 24, pp. 1243–1250, 1992.

[181] M.-L. Chan, J. M. Jones, M. Pourkashanian, and A. Williams, "The oxidative reactivity of coal chars in relation to their structure," *Fuel*, vol. 78, pp. 1539–1552, 1999.

[182] A. Strzelec, T. Toops, C. Daw, D. Foster, and C. Rutland, "ULSD and Biodiesel Particulate Oxidation Model: Combined Effects of Volatiles and Fixed Carbon Combustion," in *SAE Powertrains, Fuels and Lubricants Meeting*, 2010.

[183] E. Hippo and P. L. Walker, "Reactivity of heat-treated coals in carbon dioxide at 900 °c," *Fuel*, vol. 54, no. 4, pp. 245 – 248, 1975.

[184] O. Senneca and P. Salatino, "Overlapping of heterogeneous and purely thermally activated solid-state processes in the combustion of a bituminous coal," *Combustion and Flame*, vol. 144, no. 3, pp. 578 – 591, 2006.

[185] O. Senneca and P. Salatino, "A semi-detailed kinetic model of char combustion with consideration of thermal annealing," *Proceedings of the Combustion Institute*, vol. 33, no. 2, pp. 1763 – 1770, 2011.

[186] O. Senneca and P. Salatino, "Loss of gasification reactivity toward O_2 and CO_2 upon heat treatment of carbons," *Proceedings of the Combustion Institute*, vol. 29, pp. 485–493, 2002.

[187] T. Lang and R. H. Hurt, "Char combustion reactivities for a suite of diverse solid fuels and char-forming organic model compounds," *Proceedings of the Combustion Institute*, vol. 29, no. 1, pp. 423 – 431, 2002.

[188] S. H. Ng, D. P. Fung, and S. D. Kim, "Study of the pore structure and reactivity of Canadian coal-derived chars," *Fuel*, vol. 67, pp. 700–706, 1988.

[189] T.-W. Kwon, S. D. Kim, and D. P. Fung, "Reaction kinetics of char-CO_2 gasification," *Fuel*, vol. 67, pp. 530–535, 1988.

[190] D. P. Fung and S. D. Kim, "Chemical reactivity of Canadian coal-derived chars," *Fuel*, vol. 63, pp. 1197–1201, 1984.

[191] S. H. Ng, D. P. Fung, and S. D. Kim, "Some physical properties of Canadian coals and their effects on coal reactivity," *Fuel*, vol. 63, pp. 1564–1568, 1984.

[192] A. A. Lizzio, H. Jiang, and L. R. Radovic, "On the kinetics of carbon (Char) gasification: Reconciling models with experiments," *Carbon*, vol. 28, no. 1, pp. 7 – 19, 1990.

[193] S. Roy and A. Baiker, "No$_x$ storage-reduction catalysis: From mechanism and materials properties to storage-reduction performance," *Chemical Reviews*, vol. 109, no. 9, pp. 4054–4091, 2009.

[194] A. Trovarelli, C. de Leitenburg, M. Boaro, and G. Dolcetti, "The utilization of ceria in industrial catalysis," *Catalysis Today*, vol. 50, no. 2, pp. 353 – 367, 1999.

[195] S. Miyoshi, H. Yamada, H. Iwakuni, K. Harada, K. Minoschima, and A. Takami, *Exhaust Gas Purification Catalyst and Method of Fabricating the Same*. No. US Patent No. 2007/0117715 A1, May 2007.

[196] G. Blanchard, E. Rohart, Y. Lendresse, F. Tronel, X. Courtois, D. Duprez, S. Elbouazzaoui, and P. Marecot, *Zirconium/Praseodymium Oxide NO_x Traps and Purification of Gases Containing Nitrogen Oxides (NO_x) Therewith*. No. US Patent No. 2009/0191108 A1, Jul 2009.

[197] L. J. Gill, P. G. Blakeman, M. V. Twigg, and A. P. Walker, "The use of no$_x$ adsorber catalysts on diesel engines," *Topics in Catalysis*, vol. 28, pp. 157–164, 2004.

[198] N. Rankovic, A. Nicolle, D. Berthout, and P. Da Costa, "Extension of a kinetic model for NO oxidation and NO_x storage to fixed-bed $Pt/Ba/Al_2O_3$ catalysts," *Catalysis Communications*, vol. 12, no. 1, pp. 54 – 57, 2010.

[199] Y. Ji, T. Toops, U. Graham, G. Jacobs, and M. Crocker, "A kinetic and drifts study of supported pt catalysts for no oxidation," *Catalysis Letters*, vol. 110, pp. 29–37, 2006.

[200] E. Rohart, V. Bellière-Baca, K. Yokota, V. Harlé, and C. Pitois, "Rare earths based oxides as alternative materials to ba in no_x-trap catalysts," *Topics in Catalysis*, vol. 42-43, pp. 71–75, 2007.

[201] R. Marques, P. Darcy, P. Da Costa, H. Mellottée, J.-M. Trichard, and G. Djéga-Mariadassou, "Kinetics and mechanism of steady-state catalytic NO + O_2 reactions on Pt/SiO_2 and $Pt/CeZrO_2$," *Journal of Molecular Catalysis A: Chemical*, vol. 221, no. 1-2, pp. 127 – 136, 2004.

[202] M. Nolan, S. C. Parker, and G. W. Watson, "CeO_2 catalysed conversion of CO, NO_2 and NO from first principles energetics," *Physical Chemistry Chemical Physics*, vol. 8, pp. 216–218, 2006.

[203] M. Nolan, S. C. Parker, and G. W. Watson, "Reduction of no_2 on ceria surfaces," *The Journal of Physical Chemistry B*, vol. 110, no. 5, pp. 2256–2262, 2006.

[204] Z. Yang, T. K. Woo, and K. Hermansson, "Adsorption of NO on unreduced and reduced CeO_2 surfaces: A plane-wave DFT study," *Surface Science*, vol. 600, no. 22, pp. 4953 – 4960, 2006.

[205] V. Schmeißer, J. de Riva Pérez, U. Tuttlies, and G. Eigenberger, "Experimental results concerning the role of pt, rh, ba, ce and al_2o_3; on no_x-storage catalyst behaviour," *Topics in Catalysis*, vol. 42-43, pp. 15–19, 2007.

[206] Y. Ji, J.-S. Choi, T. Toops, M. Crocker, and M. Naseri, "Influence of ceria on the NO_x storage/reduction behavior of lean NO_x trap catalysts," *Catalysis Today*, vol. 136, no. 1-2, pp. 146 – 155, 2008.

[207] S. Benard, L. Retailleau, F. Gaillard, P. Vernoux, and A. Giroir-Fendler, "Supported platinum catalysts for nitrogen oxide sensors," *Applied Catalysis B: Environmental*, vol. 55, no. 1, pp. 11 – 21, 2005.

[208] R. J. Gorte, "Design parameters for temperature programmed desorption from porous catalysts," *Journal of Catalysis*, vol. 75, no. 1, pp. 164 – 174, 1982.

[209] A. Trovarelli, "Catalytic Properties of Ceria and CeO_2-Containing Materials," *Catalysis Reviews - Science and Technology*, vol. 38, no. 4, pp. 439–520, 1996.

[210] M. Daturi, E. Finocchio, C. Binet, J.-C. Lavalley, F. Fally, V. Perrichon, H. Vidal, N. Hickey, and J. Kašpar, "Reduction of high surface area ceo_2-zro_2 mixed oxides," *Journal of Physical Chemistry B*, vol. 104, no. 39, pp. 9186–9194, 2000.

[211] L. Olsson and B. Andersson, "Kinetic modelling in automotive catalysis," *Topics in Catalysis*, vol. 28, pp. 89–98, 2004.

[212] M. Zinkevich, D. Djurovic, and F. Aldinger, "Thermodynamic modelling of the cerium-oxygen system," *Solid State Ionics*, vol. 177, no. 11-12, pp. 989 – 1001, 2006.

[213] I. Atribak, B. Azambre, A. Bueno-López, A. García-García, L. Zenbury, and P. Burg, "Effect of ceria-zirconia composition on NO_x adsorption/desorption processes: How does it rely to soot combustion?," in *Catalysis for Environment - International Group for Research (GDRI) Meeting*, 2008.

[214] M. Hartmann, "Untersuchung der Ceroxid-Speicherkomponente von NO_x-Speicherkatalysatoren," Master's thesis, Universität Karlsruhe, 2006.

[215] G. Zhou, P. R. Shah, T. Kim, P. Fornasiero, and R. J. Gorte, "Oxidation entropies and enthalpies of ceria-zirconia solid solutions," *Catalysis Today*, vol. 123, no. 1-4, pp. 86 – 93, 2007. M. Albert Vannice Festschrift.

[216] G. Zhou, P. R. Shah, T. Montini, P. Fornasiero, and R. J. Gorte, "Oxidation enthalpies for reduction of ceria surfaces," *Surf. Sci.*, vol. 601, no. 12, pp. 2512 – 2519, 2007.

[217] B. Azambre, L. Zenboury, A. Koch, and J. Weber, "Adsorption and Desorption of NO_x on Commercial Ceria-Zirconia ($Ce_xZr_{1-x}O_2$) Mixed Oxides: A Combined TGA, TPD-MS, and DRIFTS study," *The Journal of Physical Chemistry C*, vol. 113, no. 30, pp. 13287–13299, 2009.

[218] B. Azambre, L. Zenboury, F. Delacroix, and J. Weber, "Adsorption of NO and NO_2 on ceria-zirconia of composition $Ce_{0.69}Zr_{0.31}O_2$: A DRIFTS study," *Catalysis Today*, vol. 137, no. 2-4, pp. 278 – 282, 2008.

[219] M. Adamowska, A. Krzton, M. Najbar, P. D. Costa, and G. Djéga-Mariadassou, "DRIFT study of the interaction of NO and O_2 with the surface of $Ce_{0.62}Zr_{0.38}O_2$ as deNO_x catalyst," *Catalysis Today*, vol. 137, no. 2-4, pp. 288 – 291, 2008. AWPA Symposium 2007.

[220] D. Bhatia, R. W. McCabe, M. P. Harold, and V. Balakotaiah, "Experimental and kinetic study of NO oxidation on model Pt catalysts," *Journal of Catalysis*, vol. 266, no. 1, pp. 106 – 119, 2009.

[221] V. Perrichon, L. Retailleau, P. Bazin, M. Daturi, and J. C. Lavalley, "Metal dispersion of CeO_2-ZrO_2 supported platinum catalysts measured by H_2 or CO chemisorption," *Applied Catalysis A: General*, vol. 260, no. 1, pp. 1 – 8, 2004.

[222] G. Zafiris and R. Gorte, "A study of CO, NO, and H_2 adsorption on model Pt/CeO_2 catalysts," *Surface Science*, vol. 276, no. 1-3, pp. 86 – 94, 1992.

[223] G. C. Bond, "Metal-support and Metal-additive Effects in Catalysis," *Platinum Metals Review*, vol. 27, pp. 16–18, 1983.

[224] W. Lin, A. A. Herzing, C. J. Kiely, and I. E. Wachs, "Probing metal-support interactions under oxidizing and reducing conditions: In situ raman and infrared spectroscopic and scanning transmission electron microscopic-x-ray energy-dispersive spectroscopic investigation of supported platinum catalysts," *The Journal of Physical Chemistry C*, vol. 112, no. 15, pp. 5942–5951, 2008.

[225] S. J. Tauster, "Strong metal-support interactions," *Accounts of Chemical Research*, vol. 20, no. 11, pp. 389–394, 1987.

[226] P. Bera, K. Patil, V. Jayaram, G. Subbanna, and M. Hegde, "Ionic Dispersion of Pt and Pd on CeO_2 by Combustion Method: Effect of Metal-Ceria Interaction on Catalytic Activities for NO Reduction and CO and Hydrocarbon Oxidation," *Journal of Catalysis*, vol. 196, no. 2, pp. 293–301, 2000.

[227] A. Scotti, I. Nova, E. Tronconi, L. Castoldi, L. Lietti, and P. Forzatti, "Kinetic study of lean no_x storage over the $pt/ba/al_2o_3$ system," *Industrial & Engineering Chemistry Research*, vol. 43, no. 16, pp. 4522–4534, 2004.

[228] E. Corbos, S. Elbouazzaoui, X. Courtois, N. Bion, P. Marecot, and D. Duprez, "No_x storage capacity, so_2 resistance and regeneration of pt/(ba)/cezr model catalysts for no_x -trap system," *Topics in Catalysis*, vol. 42-43, pp. 9–13, 2007.

[229] Y. Ji, T. Toops, and M. Crocker, "Effect of ceria on the storage and regeneration behavior of a model lean no_x trap catalyst," *Catalysis Letters*, vol. 119, pp. 257–264, 2007.

[230] P. Svedberg, E. Jobson, S. Erkfeldt, B. Andersson, M. Larsson, and M. Skoglundh, "Influence of the storage material on the storage of no_x at low temperatures," *Topics in Catalysis*, vol. 30-31, pp. 199–206, 2004.

[231] D. Martin and D. Duprez, "Evaluation of the acid-base surface properties of several oxides and supported metal catalysts by means of model reactions," *Journal of Molecular Catalysis A: Chemical*, vol. 118, no. 1, pp. 113 – 128, 1997.

[232] M. Piacentini, M. Maciejewski, and A. Baiker, "Role and distribution of different ba-containing phases in supported pt-ba nsr catalysts," *Topics in Catalysis*, vol. 42-43, pp. 55–59, 2007.

[233] B. Azambre, S. Collura, P. Darcy, J. Trichard, P. D. Costa, A. García-García, and A. Bueno-López, "Effects of a $Pt/Ce_{0.68}Zr_{0.32}O_2$ catalyst and NO_2 on the kinetics of diesel soot oxidation from thermogravimetric analyses," *Fuel Processing Technology*, vol. 92, no. 3, pp. 363 – 371, 2011.

[234] B. Bassou, N. Guilhaume, K. Lombaert, C. Mirodatos, and D. Bianchi, "Experimental Microkinetic Approach of the Catalytic Oxidation of Diesel Soot by Ceria Using Temperature-Programmed Experiments. Part 2: Kinetic Modeling of the Impact of the Ceria/Soot Contacts on the Rate of Oxidation," *Energy & Fuels*, vol. 24, no. 9, pp. 4781–4792, 2010.

[235] K. Leistner, A. Nicolle, and P. D. Costa, "Modelling the Kinetics of NO Oxidation and NO_x Storage Over Platinum, Ceria and Ceria Zirconia," *Applied Catalysis B: Environmental*, vol. 111-112, pp. 415–423, 2012.

[236] B. Bassou, N. Guilhaume, K. Lombaert, C. Mirodatos, and D. Bianchi, "Experimental Microkinetic Approach of the Catalytic Oxidation of Diesel Soot by Ceria Using Temperature-Programmed Experiments. Part 1: Impact and Evolution of the Ceria/Soot Contacts during Soot Oxidation," *Energy & Fuels*, vol. 24, no. 9, pp. 4766–4780, 2010.

[237] R. Vonarb, A. Hachimi, E. Jean, and D. Bianchi, "Catalytic Oxidation of a Diesel Soot Formed in the Presence of a Cerium Additive. II. Temperature-Programmed Experiments on the Surface-Oxygenated Complexes and Kinetic Modeling," *Energy & Fuels*, vol. 19, no. 1, pp. 35–48, 2005.

[238] A. Amirnazmi, J. Benson, and M. Boudart, "Oxygen inhibition in the decomposition of no on metal oxides and platinum," *Journal of Catalysis*, vol. 30, no. 1, pp. 55 – 65, 1973.

[239] L. Kunz, L. Maier, S. Tischer, and O. Deutschmann, *Modeling the Rate of Heterogeneous Reactions*, pp. 113–148. Wiley-VCH Verlag GmbH & Co. KGaA, 2011.

[240] B. Eisfeld and K. Schnitzlein, "A new pseudo-continuous model for the fluid flow in packed beds," *Chemical Engineering Science*, vol. 60, no. 15, pp. 4105 – 4117, 2005.

[241] N. Wakao and S. Kaguei, *Heat and Mass Transfer in Packed Beds*. Gordon and Breach Science Publishers, 1982.